FINAL REPORT

Deep Water Munitions Detection System

ESTCP Project MM-0739

MARCH 2010

Robert DiMarco
Dean Keiswetter
Thomas Bell
SAIC

Approved for public release; distribution unlimited.

Environmental Security Technology Certification Program

TABLE OF CONTENTS

List of Figures ……..… iii

List of Tables ……...…. v

1.0 Introduction …….. 6

2.0 The Survey Sites …….…. 8

3.0 Noise Levels …….……11

4.0 Sensor Motion ……..……13

5.0 Target Parameter Estimation …….……..19

6.0 Target Distributions in Burial Depth and Size ……..……. .21

7.0 Target Areal Densities ……..…… 31

8.0 Conclusions ……...……. 33

9.0 References …….…. 35

Appendices

Appendix A: Analysis report Sea Bright, NJ ……...…… 36

Appendix B: Analysis report MFS Hawaii survey …….……. 48

Appendix C: Analysis report MTA data sets …….…….. 66

FIGURES

4.1 MTA sensor height data. From Appendix C. ……..……. 13

4.2 TG sensor position data from the Oahu site. Top plot shows sensor and bottom location relative to surface for a single tow leg. Bottom plot shows water depth and sensor height data averaged over each leg. From appendix B. …….……. 14

4.3 MTA sensor tracks superimposed over dipole model for target number 369 from Duck site. ……...……....16

4.4 MTA data points plotted as measured field value versus the offset distance required to reconcile the measured field with the dipole model. …….……....17

5.1 Normalized histogram of the SNR distribution of targets: for all MTA data, and for the Oahu and Sea Bright TG data. …….…....20

6.1 Data from all sites plotted as depth of target center versus effective size. Dashed line at 0 is the interface between the bottom and the water. Targets with positive depths are above the bottom and those with negative depths are buried below the bottom. Targets within the red box are displayed in Figure 6.2. ……...……....21

6.2 Data from all sites plotted as depth of target center versus effective size, with size and depth histograms. Dashed line is at bottom, positive depths are above bottom (red) and negative depths are below bottom. Targets within the red box are displayed in Figure 6.3. …….……....22

6.3 Data from all sites plotted as depth of target center versus effective size, with size and depth histograms. Dashed line is at bottom, positive depths are above bottom (red) and negative depths are below bottom. ……..……....23

6.4 Histogram of effective size for all underwater sites (blue) and for typical land sites (red). ……...…….....24

6.5a Data from MTA site Blossom Point plotted as depth of target center versus effective size, with size and depth histograms. Target points are color coded by SNR. Red line is estimate of detection cutoff due to system sensitivity (see text). …….....25

6.5b Data from MTA site Duck plotted as depth of target center versus effective size, with size and depth histograms. Target points are color coded by SNR. Red line is estimate of detection cutoff due to system sensitivity (see text). …….....25

6.5c Data from MTA site Lake Erie plotted as depth of target center versus effective size, with size and depth histograms. Target points are color coded by SNR. Red line is estimate of detection cutoff due to system sensitivity (see text). ……....26

6.5d Data from MTA site Ostrich Bay plotted as depth of target center versus effective size, with size and depth histograms. Target points are color coded by SNR. Red line is estimate of detection cutoff due to system sensitivity (see text). ……..…....26

6.5e Data from MTA site Vieques plotted as depth of target center versus effective size, with size and depth histograms. Target points are color coded by SNR. Red line is estimate of detection cutoff due to system sensitivity (see text). ……...…...27

6.5f Data from TG site Oahu plotted as depth of target center versus effective size, with size and depth histograms. Target points are color coded by SNR. Solid red line is estimate of detection cutoff due to system sensitivity, with dashed lines at different SNR (see text). ……..……..27

6.5g Data from TG site Sea Bright plotted as depth of target center versus effective size, with size and depth histograms. Target points are color coded by SNR. Red line is estimate of detection cutoff due to system sensitivity, with dashed lines at different SNR (see text). ……....28

6.6 Example of sensitivity analysis (see text for explanation). …….....29

TABLES

2.1 Survey sited used in this study ……. 10

3.1 Site noise level estimates …….… 12

4.1 Sensor height statistics ……..... 15

7.1 Raw target densities …….……..... 32

ACRONYMS

UXO	unexploded ordnance
GPS	global positioning system
MTA	marine towed array
TG	towed gradiometer
Mag	magnetic
nT	nanotesla
rms	root mean square
SNR	signal to noise ratio
dB	decibel
nT/m	nanotesla per meter

1.0 Introduction

Underwater UXO sites are of increasing interest to the Department of Defense cleanup community. This interest has led to the development of specialized systems for digitally mapping magnetic or electromagnetic anomalies in shallow water. These systems are essentially extensions of successful land-based technologies to the underwater environment. Yet the cost of underwater surveying is significantly greater than similar land-based activities, and extrapolation of the current generation of shallow water systems to deeper water depths would result in even greater costs. While some of the cost escalation may be unavoidable, it is desirable to consider alternate technologies and approaches. One factor limiting the ability of the research community to do this is the lack of information about "typical" underwater sites that could be used to benchmark alternatives. This report synthesizes data and analyses from a number of underwater UXO sites that were surveyed with existing systems. The objective is to describe what we have learned to date about the underwater UXO problem; and to delineate the performance required to meet underwater UXO survey objectives.

In all seven underwater magnetometer survey sites were chosen for inclusion in this study. The sites cover a wide variety of environments in fresh and salt water, and include expected UXO areas and non-UXO areas (see Section 2). Despite the diversity, all of the sites showed some similar characteristics. While there was a wide range of target densities between the sites, and in different areas within certain sites, there were significant numbers of ferrous targets detected everywhere. As is seen at land sites that have had human use or habitation, you always find something. The large majority of targets at each site were completely buried. Thus, survey systems that cannot detect buried targets will miss a significant fraction of the total. However, at each site there were also some targets (29 % averaged over all sites) that were proud on the bottom, or only partially buried.

Internal evidence at every site indicates that the detection performance was limited by the capability of the system employed; a more sensitive system would have detected more targets. This is clear from the distribution in size and depth for targets detected in each survey (see Section 6). These distributions are consistent with being cut off at the expected (model-based) sensitivity of the survey, suggesting that part of the actual distribution was not seen. The consistency of the observed data with the model allows the development of an estimate of the detection performance for new magnetic systems, based on known system parameters. This methodology could be used to compare the expected performance of different systems, or different survey strategies, to the detection requirements of a given project.

The report is organized as follows. In Section 2 the relevant characteristics of the seven survey sites are summarized (more detailed site descriptions are given in the appendices, and in full reports cited in the references). Section 3 looks at the sensor noise levels achieved by the surveys. One important difference between land and underwater surveys is that the position of the underwater sensors must be estimated indirectly, since they cannot directly access GPS data. Section 4 reviews the depth-keeping performance of the surveys, and estimates the absolute positioning accuracy for one survey. The

various methods used in the analyses to declare target detections and to estimate target parameters are described in Section 5. The observed distributions of targets in size-depth space and in area across the sites are detailed in Section 6 and Section 7 respectively. Conclusions are summarized in Section 8.

2.0 The Survey Sites

Seven shallow water survey sites were chosen for this study based on the ready availability of sufficient magnetometer data to support the planned analyses. The sites include a range of different environments including freshwater, inshore brackish to salt water, and off-shore areas. Most of the surveys used were performed with the Marine Towed Array (MTA) system, although two other sites were used which had been surveyed with Geometrics Towed Gradiometer (TG) systems. In both of the gradiometer based surveys the data from the individual magnetometers that made up the gradiometer were available. Magnetic anomalies from each site were reanalyzed to produce uniform target lists with location, size, SNR and fit coherence. This report will look at collective characteristics of the whole data set, and contrast differences across the sites. More detailed data for individual sites can be found in reports prepared for this analysis (Appendices A and B, for the two TG sites, and Appendix C, for the MTA sites), as well as in the original site reports listed in the references.

Table 2.1 lists some characteristics of the seven sites. Included in the table are the site name (as they will be referred to in this report), the date when the survey was conducted, the range of water depths in the survey area, the system used, the type of coverage, and the number of targets included in the later analyses. The survey coverage column uses the term “lines” for surveys where the spacing between tow lines was significantly greater than the sensor coverage; in these cases the survey attempted to sample a large area to determine the distribution of targets, and delineate areas with and without potential UXO. For surveys labeled “blanket” the tow lines were close enough to provide continuous sensor coverage in the cross-track direction, allowing detection of all targets in an area of interest. For the Blossom Point both techniques were used; a large area was surveyed with widely spread lines, and then a smaller area within was surveyed completely.

The Sea Bright survey took place several miles off the coast of New Jersey in an area that was used as a source of sand in beach replenishment projects. The original impetus for the survey was the discovery of several UXO objects on the replenished beach. The source location had been used in times past as a firing range for Fort Hancock, and the area sees significant commercial and recreational traffic. The survey was meant to ascertain the extent of potential UXO in the area. Several widely spaced long tow lines were surveyed with two cesium vapor magnetometers separated by 2 meters (cross-track). The tows were along the shore direction in an area of relatively uniform depth and the sensors were maintained at approximately 2 meters off the bottom. Specific targets found in the survey were not recovered, although divers did find UXO objects in the same vicinity following the survey (refs. 1, 2).

The Duck survey in Currituck Sound inshore from a barrier island in North Carolina was the first field demonstration of the MTA system. The site is adjacent to the land-based former Navy Target Facility at Duck, and was expected to contain UXO items that had fallen short of the target area. The area sees significant commercial and recreational traffic. The MTA has eight magnetometers, spaced 61 cm apart, on a towed sensor platform. The sensor platform has active control elements that allow its depth to be changed during the tow in response to changing water depth and obstructions on the

bottom. In this case the sensors were towed about 1 meter from the bottom. The survey provided blanket coverage of an area of roughly 60 hectares from the shore to about 4 meters depth. One hundred of the targets detected during the survey were selected for recovery after the analysis; numerous munitions items were recovered, as well as non-munitions items such as commercial crab traps (ref. 3).

The Ostrich Bay survey also used the MTA system. This site is part of the Puget Sound and is adjacent to the former Naval Ammunition Depot in Bremerton, Washington. The bay had not been used as a range, but had been a working port facility where ordnance items were loaded and unloaded. It is mostly used for recreation at this time. The water depth ranged from 1 to 12 meters and the sensors were generally towed at 1.3 meters from the bottom. However, underwater obstructions in parts of the site led to large variations in the tow height. The survey provided blanket coverage of about 75 hectares. As at Duck some targets (120) were chosen from the detection list for recovery by divers. In this case few munitions related items were recovered (ref. 4).

The Lake Erie site is in freshwater adjacent to the former Erie Army Depot. The off-shore area was the impact zone for artillery proof testing that was performed at the depot over many years. The area has mostly recreational traffic at this time. Large numbers of munitions related targets were expected (and found). The survey was designed to find the areas of potential UXO concentration within the large site (10000 hectare) and to determine if range related items were migrating out of the known impact areas. The survey consisted of widely spaced MTA tow lines that cut across the impact fan roughly parallel to the shore. The initial survey lines began as close to the shore line as the system could operate and then moved to progressively deeper water (depths ranged from 1 to 10 meters). The system was generally towed a little higher, 1.5 meters from the bottom, then in previous MTA surveys. The resulting loss of sensitivity was acceptable since the main targets of interest were larger munitions items. A subset of 186 targets was selected for intrusive investigations, and 141 objects were recovered including 130 munitions, or munitions related, items (ref. 5).

The next MTA survey was in open ocean water at the Bahia Salinas del Sur, part of the Vieques Naval Training Range on the south side of Vieques Island in Puerto Rico. The area is currently off-limits to all unauthorized activity. Due to ubiquitous coral and marine grasses the MTA could only be used in areas deeper than about 2 meters, and the average tow depth was two meters off the bottom. This blanket survey covered 79 hectares. In order to access the areas shallower than 2 meters, a separate measurement system was used with to magnetometers mounted in a fiberglass skiff. In this system the sensors were fixed to the skiff and so the sensor height from the bottom depended on the water depth. The skiff system was used to survey an additional 32 hectares. Overall 603 targets were fit from the data; however there was no follow-up to determine ground truth for these objects (ref. 6).

In 2007 an underwater towed gradiometer survey was conducted by Geometrics on the Navy Degaussing Range which is part of the Pearl Harbor region of Honolulu on the island of Oahu in Hawaii. The objective was to locate magnetic debris in the survey area

that could interfere with ship degaussing operations. The area is a working part of this busy harbor complex and was expected to have large numbers of ferrous objects. Since the concern was mainly with larger objects the sensor was towed at an average height above the bottom of 4 meters, a greater height than for any of the other survey sites. The survey provided blanket coverage of about 25 hectares, and the analysis recorded 253 targets (see appendix B).

The final MTA site was at on the Potomac River, adjacent to the Blossom Point Research Facility in Maryland. As for the Lake Erie site the main emphasis was to determine the extent of potential UXO objects on this large (3500 hectare) site. Initially, widely spaced transects covering the whole area were surveyed. After initial analysis a smaller 30 hectare area was selected for blanket coverage. The data analyzed here includes both of these data sets (ref. 7).

NAME	**DATE**	**DEPTH**	**TYPE**	**COVERAGE**	**TARGETS**
Sea Bright, NJ	9/95	12-15 m	TG	LINES	303
Duck, NC	5/05	1-3 m	MTA	BLANKET	432
Ostrich Bay, WA	6/06	1-12 m	MTA	BLANKET	648
Lake Erie, OH	8/06	1-10 m	MTA	LINES	779
Vieques, PR	6/07	1-10 m	MTA	BLANKET	603
Oahu, HI	9/07	11-13 m	TG	BLANKET	253
Blossom Pt., MD	10/07	1-10 m	MTA	MIXED	619
				Total:	3637

Table 2.1. Survey sites used in this study.

3.0 Noise Levels

Sensor noise levels were estimated as a first step in determining detection performance for the seven surveys. For the two TG sites a single noise level was estimated from the data and applied to the all targets from that site. For the MTA sites the target analysis software automatically estimated a noise level for each target based on surrounding data. The average of these individual estimates was then computed, along with an overall site noise estimate as explained below.

In the TG data sets the noise estimate was made after targets had been detected. At the Sea Bight site the operator chose locations along the tow lines that were more than 15 meters from any target. Data segments along the line within 15 meters of the chosen locations were then used to estimate the noise. Note that although the data were processed as a horizontal gradiometer the raw data from each magnetometer were recorded and these total field data from both sensors were used to estimate the noise level. In all 44 locations were used for the noise analysis, with the average noise level estimated at 0.12 nT. A similar methodology was used for the Oahu TG site. In this case thirteen locations for the noise analyses were chosen away from detected targets on the 2-dimensional data map. All points within a 15 meter box were used in the calculation; again total field data from both magnetometers were used. The average noise level for the site was estimated to be 0.22 nT. Tables that list the noise statistics for each of the noise locations for these two sites are contained in the site reports (Appendices A and B). The overall noise level for the site was used when calculating the SNR for individual targets.

Two methods were used to estimate the noise level for the MTA sites. First there is an estimate that is created along with each target parameter fit. When the operator selects data for a target, a region larger than the anomalous data is chosen. As described in Appendix C, the software then automatically classifies data in the scene to be either signal or background. The background data is used to estimate a noise level associated with that target. The median of these noise levels over all the targets is used as an estimate of the site noise level (the median is used because the automated method will overestimate the noise for a few targets if insufficient surrounding data are selected). A second method was used to estimate the noise level over the entire site. Data were separated out for each tow line; all of the data was used with no attempt to remove targets at this point. The data were sorted by sensor amplitude and a method (described in Appendix C) was used to estimate a cutoff between the Gaussian distributed bulk of the data, and the non-Gaussian tails (presumably from targets). The resulting noise level estimates from each line were averaged to produce a site estimate. The results for all seven of the sites are summarized in Table 3.1. The trends over the five MTA sites are the same for both noise estimation methods used, although the second method results in consistently lower values.

As noted in the Appendix C, and in the MTA site reports, it appears that the observed noise levels for that system are driven by magnetic noise from moving components of the sensor platform, rather than from environmental sources. In particular the actuators that move the control surfaces appear to be the source of the observed noise. This is clear when looking at how the noise varies across the sensor platform. The sensors closer to the

outside (and so closer to the actuators) experience higher noise levels than those towards the center (see Table 2 in Appendix C). The significantly lower noise level seen in the MTA data from the Duck site resulted from the use of actuators with lower magnetic signatures at that time. After that survey the actuators needed to be replaced and, unfortunately, the replacements had greater intrinsic magnetic noise.

In summary the noise levels observed for the MTA system are of order ten times greater than those observed in the TG data. The MTA noise level appears to be driven by system noise, rather than by environmental sources. These higher noise levels are the result having active depth control on the sensor platform that allows the MTA to maintain closer contact to the bottom. The result of this strategy on detection sensitivity will be examined in Section 6.

NAME	**TYPE**	**HEIGHT FROM BOTTOM (m)**	**NOISE LEVEL (nT)**	
Sea Bright	TG	2.0	0.12	
Oahu	TG	4.0	0.22	
			Method 1	**Method 2**
Duck	MTA	1.0	0.56	0.43
Ostrich Bay	MTA	1.3	3.8	2.9
Lake Erie	MTA	1.5	2.9	1.2
Vieques	MTA	2.0	3.1	2.0
Blossom Pt – lines	MTA	1.3	1.5	1.2
blanket area				2.3

Table 3.1. Site noise level estimates.

4.0 Sensor Motion

This section discusses two topics related to sensor platform motion: the depth keeping performance in the seven surveys, and an estimate of the accuracy of the position data from the MTA system. Depth keeping is an important aspect for underwater detection systems since every incremental increase in sensor height from the bottom results in an equal decrease in the depth to which a given sized object can be detected. It will be seen in Section 6 that the large majority of objects at each site were buried, and that the sensor height above the bottom is the main determinant of detection performance.

4.1 Depth Keeping

All of the surveys considered in this report had a method to monitor water depth and the position of the sensor in the water column as it was towed through the water. In the TG surveys the sensor was towed at sufficient height above the bottom that it was not in danger of hitting submerged obstacles and a steady height was maintained. The MTA system has a forward-looking sonar to spot obstructions in front of the sensor platform and the ability to adjust its depth to "fly" over such obstacles. This allows it to keep closer to the bottom on average, but results in large changes in the height of the data where there are significant bottom obstructions.

MTA position data from two different sites are shown in Figure 4.1. The vertical axis is the height above the bottom of the sensor platform; the horizontal axis is the leg

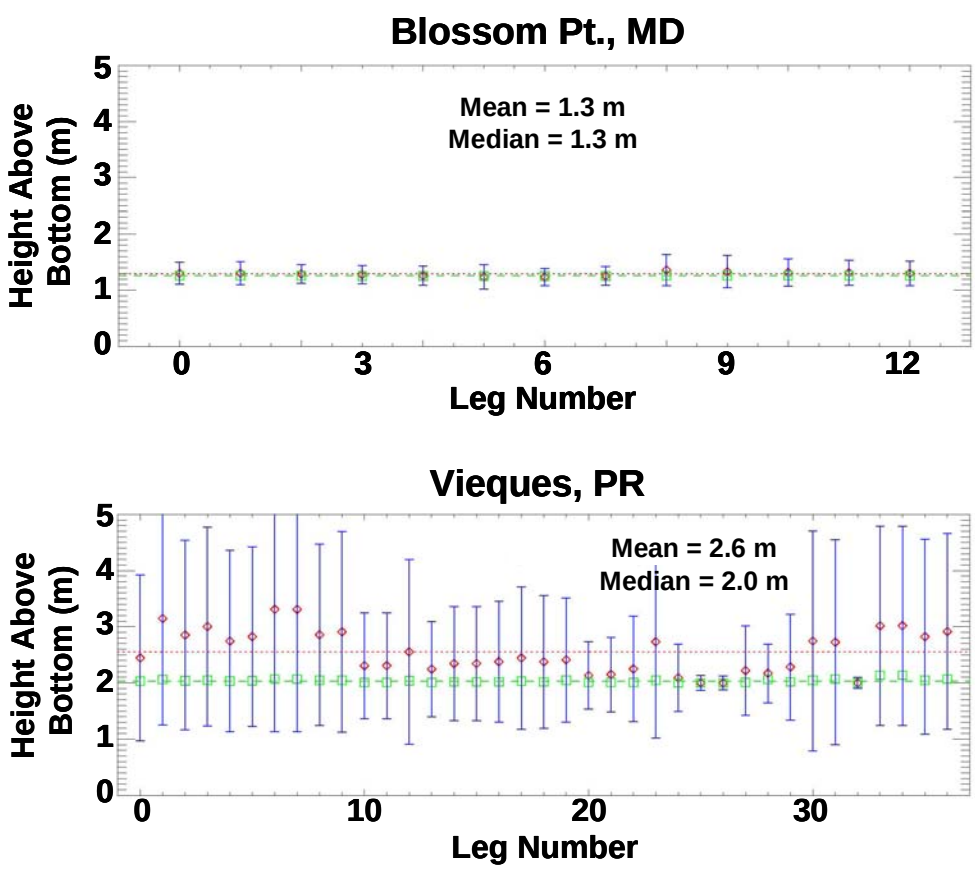

Figure 4.1. MTA sensor height data. From Appendix C.

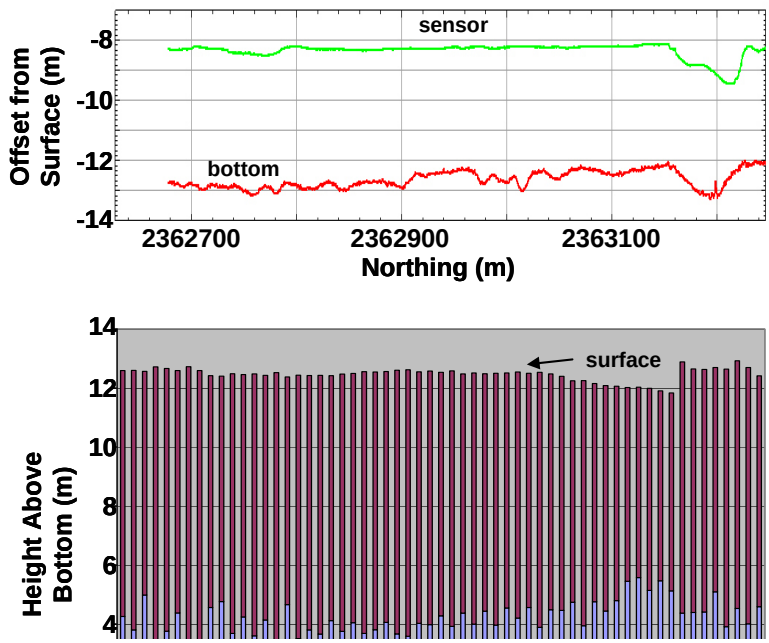

Figure 4.2. TG sensor position data from the Oahu site. Top plot shows sensor and bottom location relative to surface for a single tow leg. Bottom plot shows water depth and sensor height data averaged over each leg. From appendix B.

number. For each leg the median depth is plotted in green, the mean depth is shown in red and the bars around the mean show plus and minus one standard deviation of the depth data for that leg. The data from Duck are typical of sites with little or no underwater obstruction. The system was able to maintain its target depth of 1 meter over most of the site with minor deviations. The data from Vieques is very different. In this case almost every leg had significant obstruction (mostly due to coral reefs and other bottom structures). While the median height was close to the planned height of 2 meters, there were significant depth excursions to avoid the obstructions which significantly raised the mean and standard deviation.

Depth keeping data from the TG sensor at Oahu is shown in Figure 4.2. The first plot shows an example of the altitude profile for a single tow line. The depth of the sea floor, determined by sonar on the tow vessel, is shown in red (with the water surface as the origin of the vertical axis). The depth of the sensor, determined by a pressure sensor on the tow body, is shown in green. The difference between the two is the sensor height from the bottom, nominally targeted at 4 meters. Sensor height is varied by adjusting the tow speed with a fixed cable length. This method leads to excursions at the end of tow lines as the effective speed through the water changed during turns. Although the sensor platform cannot be controlled actively like the MTA the height from the bottom is well maintained, since at this height there are no obstructions that need to be avoided, and the sea-floor relief in this area was relatively flat. The second plot shows data from the whole site with the average water depth for each leg as a purple bar, and the average tow height shown in blue. The standard deviation of sensor height above the bottom was typically of order 0.3 m excluding the turns which occurred outside the mapped area.

Table 4.1 shows the average sensor height for the seven survey sites. For the MTA sites the standard deviation of the mean can be used to determine which sites had more uniform tows, like Duck, and which had significant obstructions to be avoided, like Vieques.

NAME	**TYPE**	**Sensor Height From Bottom (m)**		
		Mean		**Std. Dev.**
Sea Bright	TG	2.0		0.5
Oahu	TG	4.0		0.3
		Median	**Mean**	**Std. Dev.**
Duck	MTA	1.0	1.2	0.4
Ostrich Bay	MTA	1.3	1.8	1.4
Lake Erie	MTA	1.5	1.5	0.2
Vieques	MTA	2.0	2.6	1.4
Blossom Pt. – lines	MTA	1.2	1.4	1.1
blanket area	MTA	1.3	1.3	0.2

Table 4.1. Sensor height statistics.

4.2 Estimation of Position Error

One of the key differences between land and underwater surveys is that GPS receivers cannot directly track the location of underwater sensors, since the antenna cannot receive underwater. For all of the surveys used in this study there was a GPS receiver attached to the tow vessel which provided an absolute position reference. The relative offset from the GPS receiver to the sensors was then estimated using auxiliary measurements and models of the sensor platform motion. The absolute positions of the collected data were then inferred from the time dependent GPS position and the estimated offsets. Some notion of the accuracy of the absolute position may be gleaned by looking at target reacquisition results. However, the reacquisition relies on the same kind of indirect positioning as the original measurement. Protocols for reacquiring underwater targets with UXO trained divers suggest that an accuracy of only a few meters in the stated position is expected.

An analysis of data from one site was performed to get a better estimate on the absolute position accuracy achieved in these surveys. The analysis concentrated on a particular class of targets seen at the Duck site. These targets were fairly large with effective radii in the 0.6 to 0.7 meter range (they were assumed by the survey team to be 11.75 inch Tiny Tim rockets, which were known to have been used at the site). They were also deep, being buried 3 to 5 meters below the bottom. These depths, combined with the 1-meter average height of the sensor, meant that the offset from the sensors to the center of the targets was 4 to 6 meters. This large offset was important for the analysis since at this range it is expected that higher order magnetic moments of the target will be small compared to the dipole component and so the data will be consistent with a dipole model.

An example of the data from one such object is shown in Figure 4.3. The color image shows the model for the best fit dipole parameters centered at the origin and evaluated at the average vertical offset for the data. The dark lines crossing the image are made from dots at the locations where MTA data were recorded (the data are also taken at different heights which dimension is not shown in the figure). Across each tow leg there are eight sensor measurements which move in parallel as the tow body wiggles through the scene. The density of measurements along the tow direction is so high that the lines appear continuous at this resolution. Several overlapping legs cross the region in the y-direction. Also, two additional diagonal passes through the area are visible. Along a given leg the relative positions of the data points for the eight sensors are constrained by the inter-sensor spacing, and the known tow speed. However, between tow legs the relative error in the 3-dimensional position may be much larger.

To estimate the position error all of the data points are compared to the best fit 3-dimensional dipole model. First, the dipole model of the target is created using all of the data points to fit the target size, inclination, declination and absolute location in three dimensions. The model may then be inverted to estimate the measured magnetic field at any location relative to the target. It is assumed in the analysis that the magnetic field

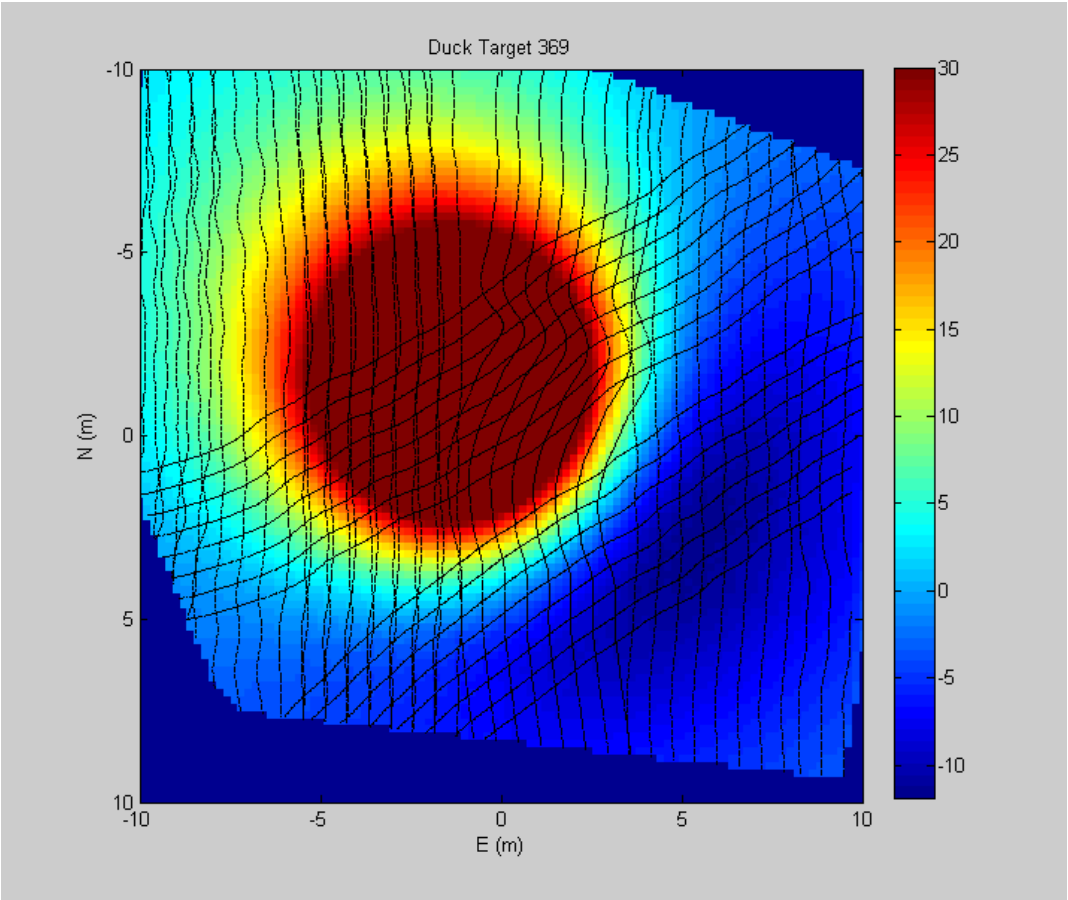

Figure 4.3. MTA sensor tracks superimposed over dipole model for target number 369 from Duck site.

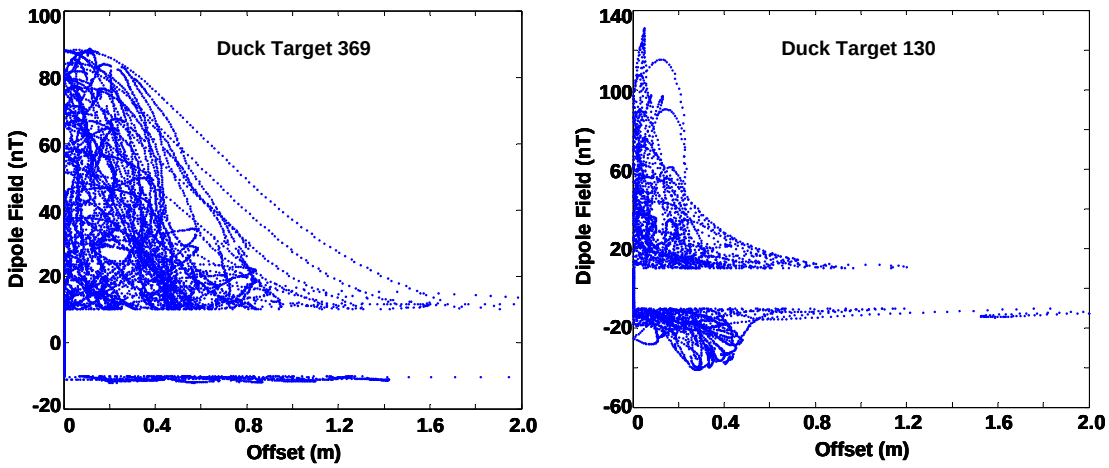

Figure 4.4. MTA data points plotted as measured field value versus the offset distance required to reconcile the measured field with the dipole model.

measurement at each data point is correct, but that the position may be in error. The offset from the recorded position of the point to the closest point in the 3-dimensional dipole model that matches the measured field value is then calculated. These offsets represent the estimate of the position error. The assumption that measured field is correct is necessary for the analysis, but is of course incorrect; the field measurement is effected by the sensor noise. This assumption then restricts the usefulness of the resulting offset estimate to parts of the model where the offset due to the magnetic field measurement error is small compared to the actual position offset; that is to places where the spatial gradient of the model is large compared to the field measurement error. To account for this effect the analysis was restricted to data points with a measured field anomaly of greater than 10 nT (recall from Section 3 that the magnetic field noise for this site averaged less than 1 nT).

Results for two targets, which are typical of all the targets studied, are shown in Figure 4.4. In these plots the vertical axis is the measured magnetic field anomaly (note the area from -10 to 10 nT is empty), and the horizontal axis is the calculated offset. Data are plotted as separate points. The majority of the data points lie below offsets of about 0.4 meters. Note that the offsets increase significantly as the magnitude of the measured field decreases to near 10 nT, in fact including points with lower measured field values results in very large offset estimates. This suggests that the increase in offset at low field values is an artifact of the assumption that the magnetic field measurement is correct, rather than a true measure of position errors.

In considering the utility of these results it is important to note that the method used did not directly measure the position error; in some ways it underestimates and in other ways overestimates the true error. For instance the offset calculated for a given point was the minimum distance needed to reconcile the measured data and the model, the true offset may have been larger if it was in a different direction. On the other hand, as noted above, any error in the magnetic field measurement will tend to increase the calculated offset. Also, systematic errors in position are not captured. Despite these caveats the

consistency of the results across several different targets, each consisting of several separate legs, suggests that 0.4 meters rms is a good estimate of the position error achieved with the MTA system.

5.0 Target Parameter Estimation

For all of the surveys considered here target parameters were estimated in an automated fashion from target data were selected by an operator. The operator display consists of a 2-dimensional image of mapped amplitudes for blanket data, or time series of amplitudes for line data. The operator looks for anomalies that match the criteria for the survey, and then uses interactive tools to define the data to be used in fitting the anomaly. The selected data, consisting of a 3-dimensional absolute location, and measured amplitude are then fed to an inversion routine that fits a dipole model to the data. The model has 6 unknowns: the 3-dimensional position of the dipole, the dipole inclination and declination angles, and the dipole strength. The fitting routine also calculates the coherence of the resulting fit and the SNR for the target.

Although the same general procedure was used, the two different operators that reanalyzed the TG and MTA data used somewhat different detailed methodology and so care must be exercised in comparing the data directly. An example of this has been mentioned in Section 3, where different methods were used to estimate the magnetic noise for TG and MTA sites. Another example is the method of calculating the SNR reported for targets. For the TG sites the SNR for each target was calculated using the signal levels for that target and the site averaged noise. However, for the MTA sites the calculation was performed using a local estimate of the noise which varied for each target. In addition, the signal used in the MTA data is modulated by the estimated noise and so the quoted SNR more closely resembles a “signal excess” over threshold (see Appendix C). The effects of these differences are difficult to sort out in detail; however, it is clear that the reported MTA SNRs are significantly smaller than those reported for the TG system. The details of the two different methods used are described in the appendices. Histograms of SNR for the reported targets from the MTA data and from the two TG sites are shown in Figure 5.1.

Another difference among the surveys was that different criteria were used to select targets. As noted in the reports for the TG analyses, the operator was guided in selecting targets by automatic target selection, based on thresholding of peaks in the analytic signal channel. The operator mostly resolved duplicate entries of the same target from the automated selection, and also added targets at the edge of the field that the automated procedures could not discern. The threshold was set consistent with the original intent of the surveys which was to detect larger objects; and as a result the SNRs for all of the selected targets are large (the resulting target distributions have more then 95% of targets with SNR greater than 20 dB). Also, the threshold for the two TG surveys was different; 3 nT/m was used for the Oahu survey, while 5 nT/m was used for the Sea Bright survey even though the estimated noise level at Sea Bright was lower. Thus, the SNR distribution of the Sea Bright targets is skewed towards larger values than that for Oahu (see Figure 5.1). The differences between the SNR distributions for the TG sites and for the MTA sites, apparent in Figure 5.1, are larger than would be expected from the differences in the calculations referred to in the last paragraph. It appears that the automated targets selection used in the TG analyses resulted in an effectively higher detection threshold. This will also be evident in the distributions of target parameters described in the next section.

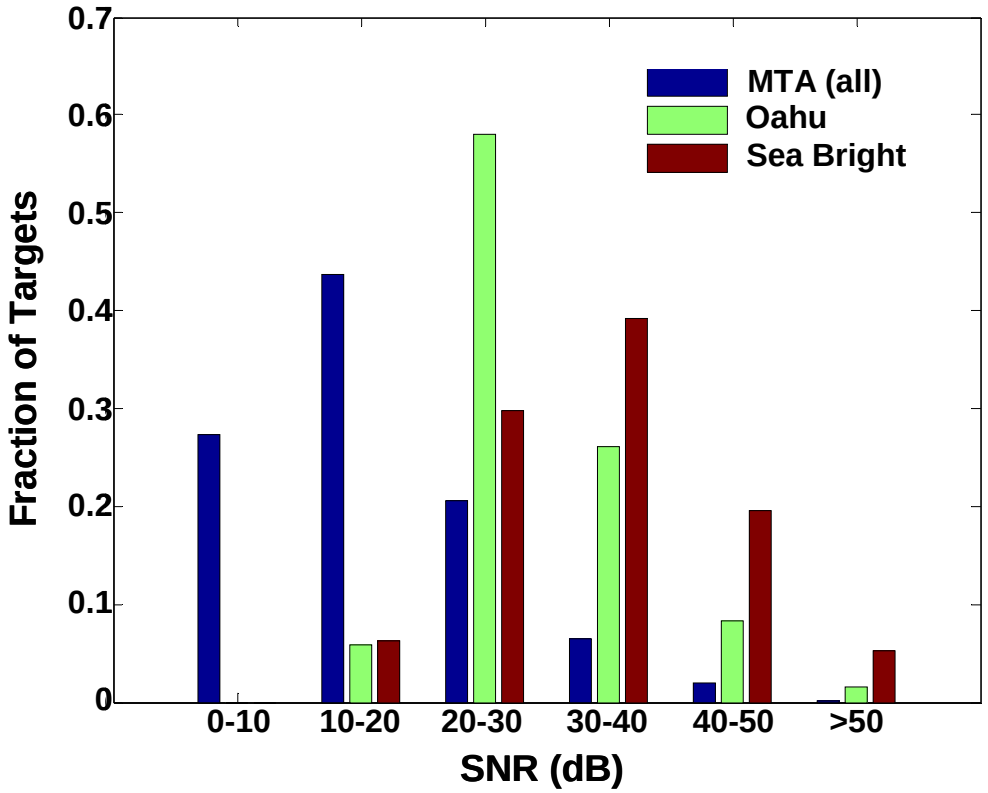

Figure 5.1. Normalized histogram of the SNR distribution of targets: for all MTA data, and for the Oahu and Sea Bright TG data.

6.0 Target Distributions in Burial Depth and Size

In this section we review the distribution of targets in size and depth in order to describe what is "typical" for targets at underwater sites, and to show how the detection sensitivity of a given survey will affect what part of that typical distribution can be detected. Looking at all of the sites together, and then examining each in turn, will allow construction of a semi-empirical model for how the detection sensitivity depends on the achieved noise level, the sensor height from the bottom, and the Earth's total field at the survey site. This model, using the parameters calculated earlier in this report, appears to explain much of the observed variation in detection between the survey sites. This is especially true for the MTA data which were all collected and processed similarly.

The aggregate underwater data set consists of 3637 fit targets. The distribution of those targets in size and depth is shown in Figure 6.1. The depth axis is plotted with zero being the calculated water-bottom interface at the target location. Negative values indicate the calculated depth of the center of the target is below the bottom, while positive values of depth imply that the center of the target is above the bottom (the target is presumably resting on the bottom, or semi-buried). The horizontal axis plots the target size as the effective radius (the radius of a spherical target that would produce the same dipole parameters as observed, if it was centered at the fit location).This plot shows all of

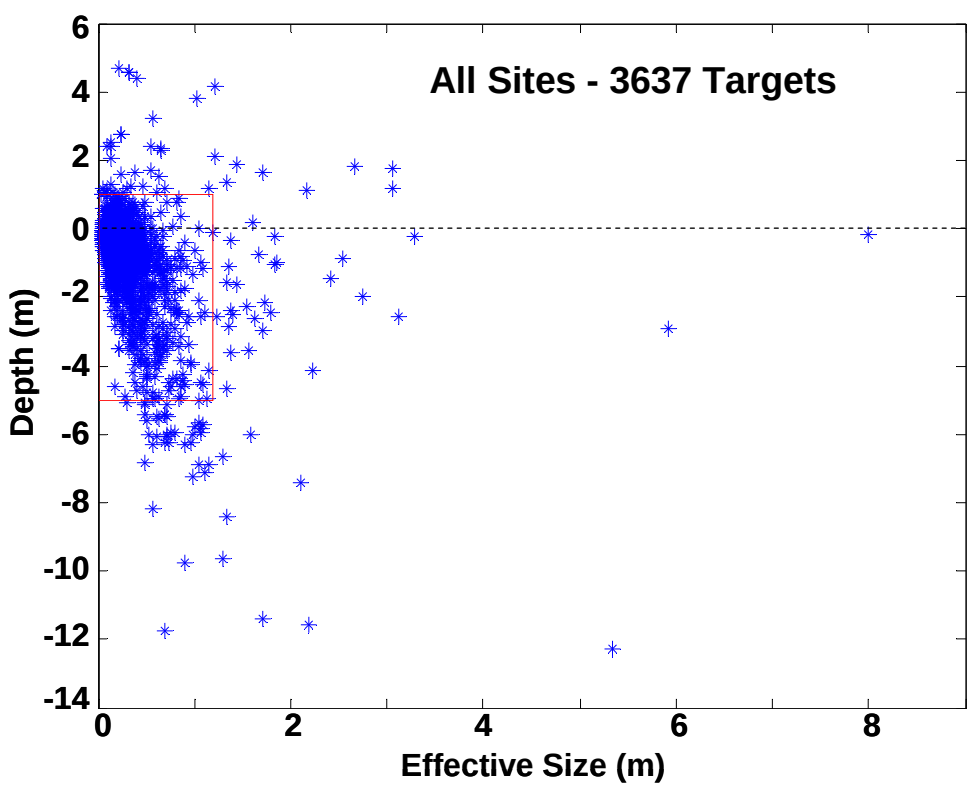

Figure 6.1. Data from all sites plotted as depth of target center versus effective size. Dashed line at 0 is the interface between the bottom and the water. Targets with positive depths are above the bottom and those with negative depths are buried below the bottom. Targets within the red box are displayed in Figure 6.2.

the target fits and includes a handful of outliers with parameters that are probably not correct. These outliers may be due to poorly reconstructed data, or to the use of a single dipole model to fit objects that are actually extended in space or that consist of closely spaced multiple objects.

The large majority of the targets fall within the red box shown in Figure 6.1. These are replotted with expanded axes in Figure 6.2 (similarly, the boxed region on Figure 6.2 is expanded in Figure 6.3). This figure also contains normalized histograms of the target size and depth distributions. The change in color on the histogram of burial depths occurs at the bottom; 15 % of the targets are fit to a depth at or above the bottom. Since this is the depth of the target center, some targets with small negative depths may be partially unburied. If we include targets that are fit to depths less than one radius, then 29 % of targets are proud, or only partially buried. This still leaves greater than 70 % of the targets that are completely buried. These features are consistent across all seven of the test sites; the large majority of detected targets are fully buried under the bottom; however, all of the sites also exhibit a significant fraction of targets that appear from the fits to be proud on the bottom.

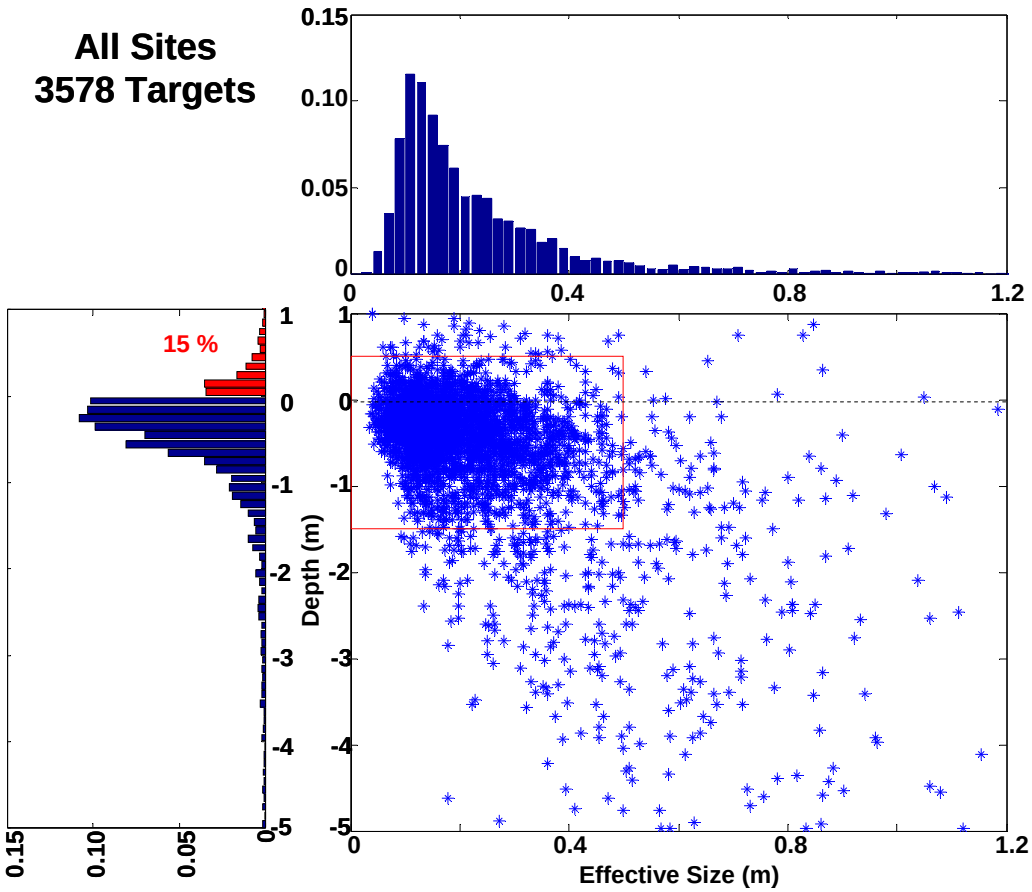

Figure 6.2. Data from all sites plotted as depth of target center versus effective size, with size and depth histograms. Dashed line is at bottom, positive depths are above bottom (red) and negative depths are below bottom. Targets within the red box are displayed in Figure 6.3.

The size histogram shows that most of the targets are relatively small, the distribution peaks just above 0.1 m effective radius. The distribution is cut off on the low side by the inherent inability of the systems employed to detect smaller objects at longer ranges. However, because of the different sensor heights and noise levels of the different surveys, the cutoff varies site to site as will be shown below. Comparison with target size distributions from typical land sites, as is done in Figure 6.4, suggests that the smaller objects may be present underwater as well; they just cannot be detected with the systems used. The ground systems are not any more sensitive, but they can be maintained closer to the ground surface and so can detect smaller objects if they are present. Another feature seen on the comparison in Figure 6.4 is that the underwater distribution is wider, that is it has relatively greater numbers of larger objects than the land distribution. The reason for this is not immediately clear although several explanations present themselves. Naval munitions tends to be larger than those typically used in surface warfare; so those sites that contain naval UXO may be expected to have larger sized targets. Large metal objects are harder to recover underwater and in many settings will remain in place once they are introduced. For instance lost anchors, or even outboard motors, are not likely to be recovered once lost in a few meters of water, while similarly sized objects that fall off

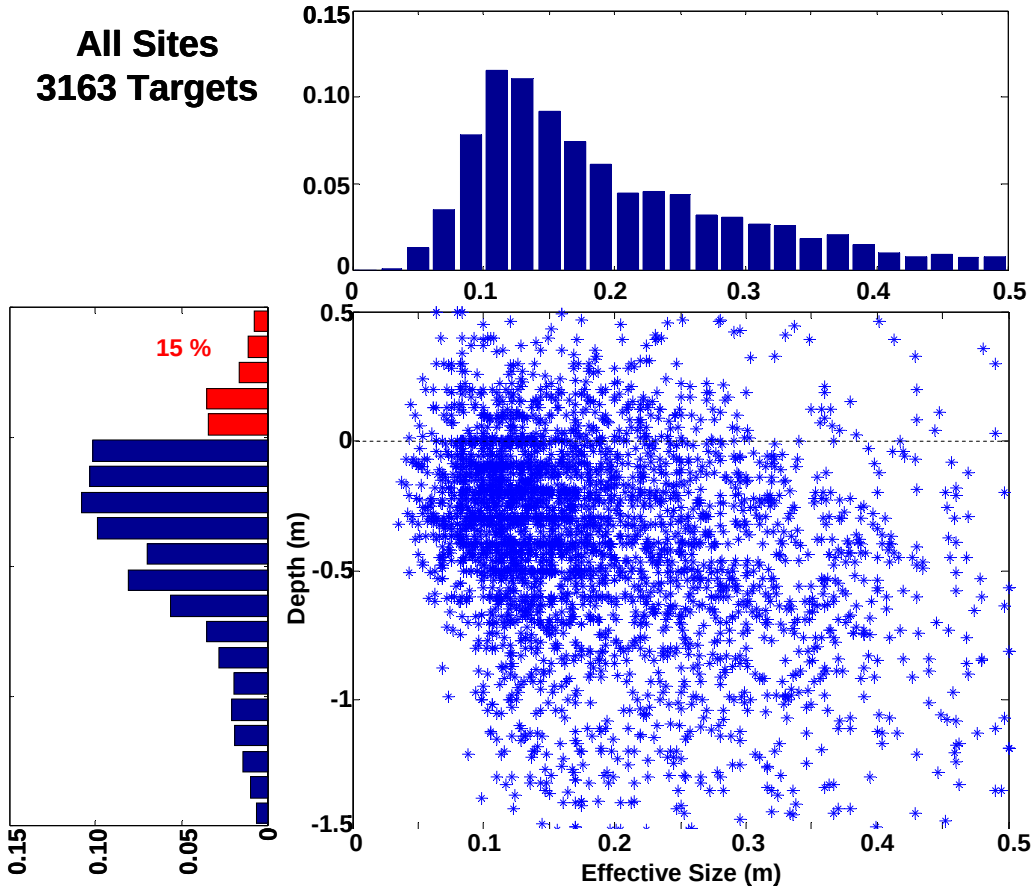

Figure 6.3. Data from all sites plotted as depth of target center versus effective size, with size and depth histograms. Dashed line is at bottom, positive depths are above bottom (red) and negative depths are below bottom.

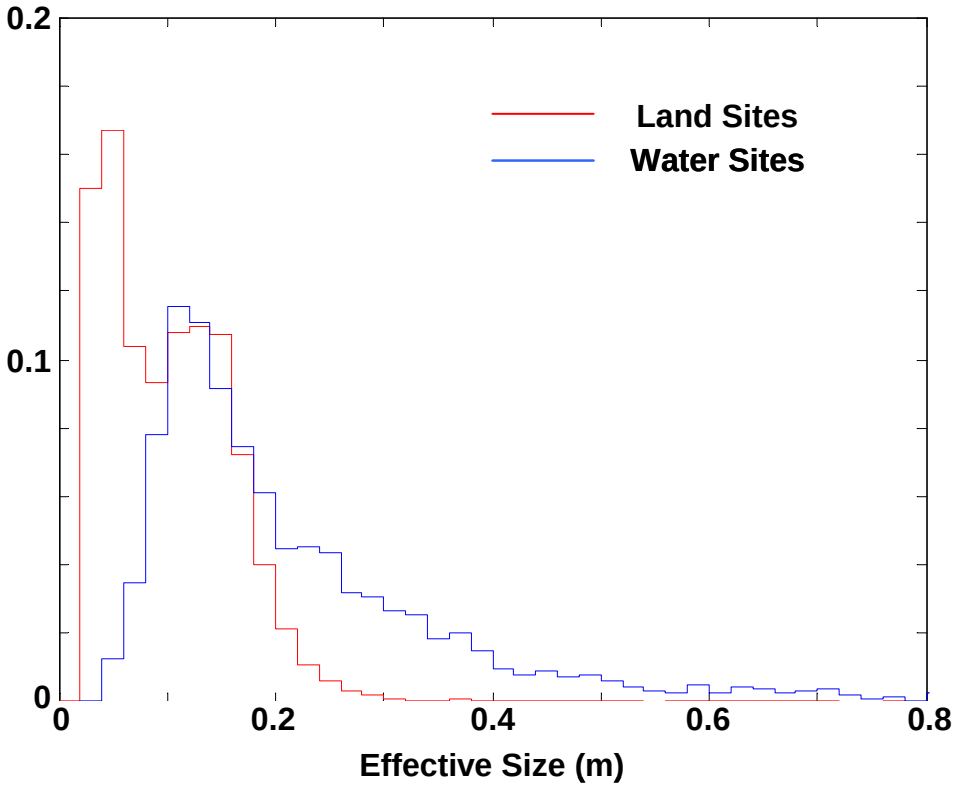

Figure 6.4. Histogram of effective size for all underwater sites (blue) and for typical land sites (red).

a truck on land will be picked up. Also, large objects on the surface are likely to be moved, or ignored, in a land survey; while similar objects are counted underwater.

The target distributions for each site are different than the aggregate; the differences are driven by characteristics of the sites themselves, and by the sensitivity of the surveys performed. Figures 6.5a-g show the size depth distributions from the seven survey sites. In these plots the each target point is colored according to its calculated SNR. For any given site the same expected features are seen; larger shallower targets have generally higher SNR than smaller or deeper ones. Beyond the lowest SNR targets detected there is an apparently linear cutoff in size-depth space below which no targets are seen. For example Figure 6.5a shows the distribution for the MTA survey at Duck. A red line is drawn at the approximate location of the size-depth cutoff. A linear cutoff is expected since the quantity being measured, the magnetic field, is proportional to the cube of the effective radius, *a*, over the cube of the range to the target, *z*, (or burial depth plus tow height):

$$B \propto \frac{a^3}{z^3} \quad . \qquad (1)$$

The slope of the cutoff line depends on the SNR. Factors that change the SNR at different sites such as the noise level and total Earth field are expected to change the slope. Given a reference line with slope η_0, corresponding to a survey with sensor noise N_0, and Earth

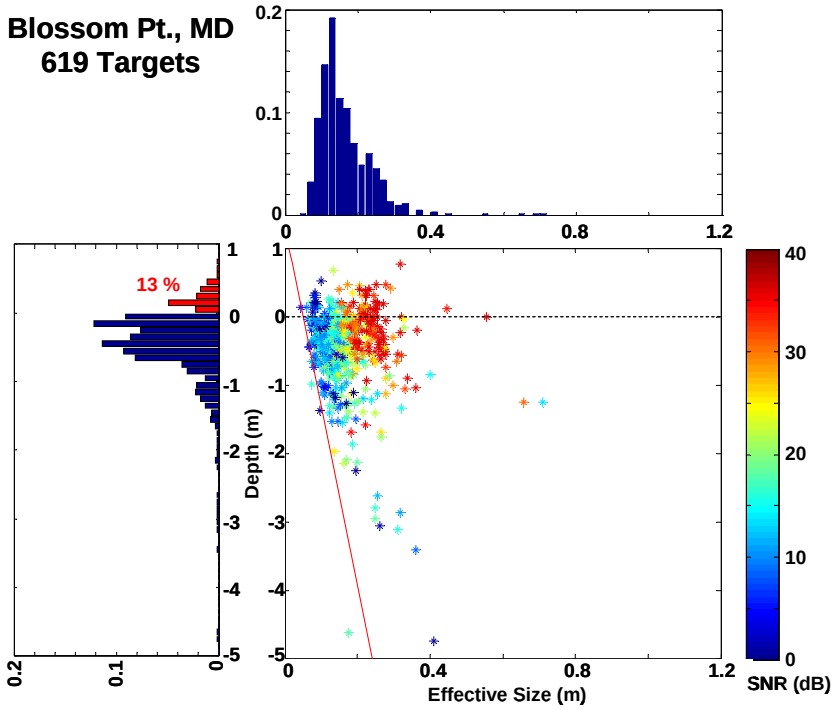

Figure 6.5a. Data from MTA site Blossom Point plotted as depth of target center versus effective size, with size and depth histograms. Target points are color coded by SNR. Red line is estimate of detection cutoff due to system sensitivity (see text).

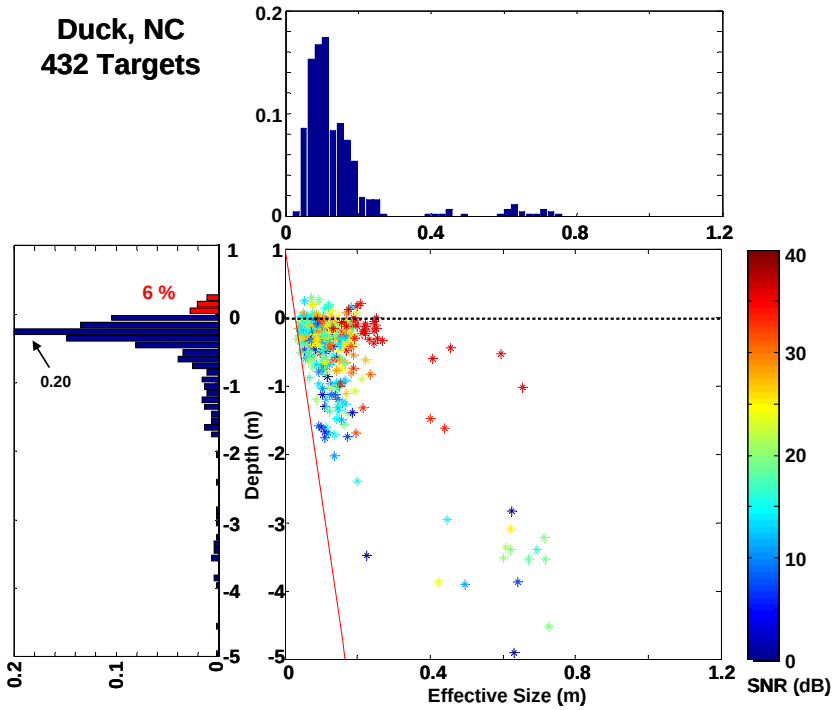

Figure 6.5b. Data from MTA site Duck plotted as depth of target center versus effective size, with size and depth histograms. Target points are color coded by SNR. Red line is estimate of detection cutoff due to system sensitivity (see text).

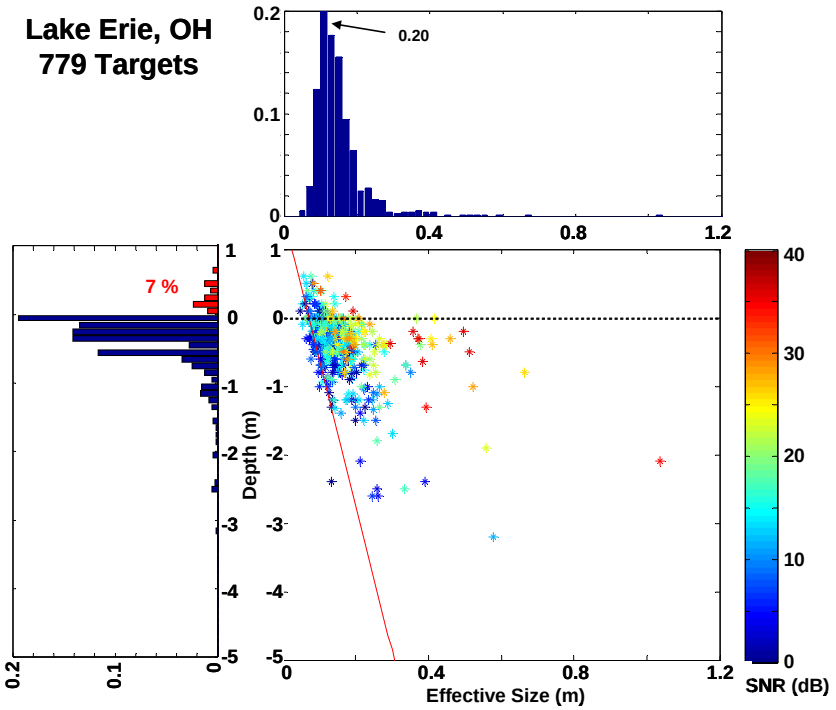

Figure 6.5c. Data from MTA site Lake Erie plotted as depth of target center versus effective size, with size and depth histograms. Target points are color coded by SNR. Red line is estimate of detection cutoff due to system sensitivity (see text).

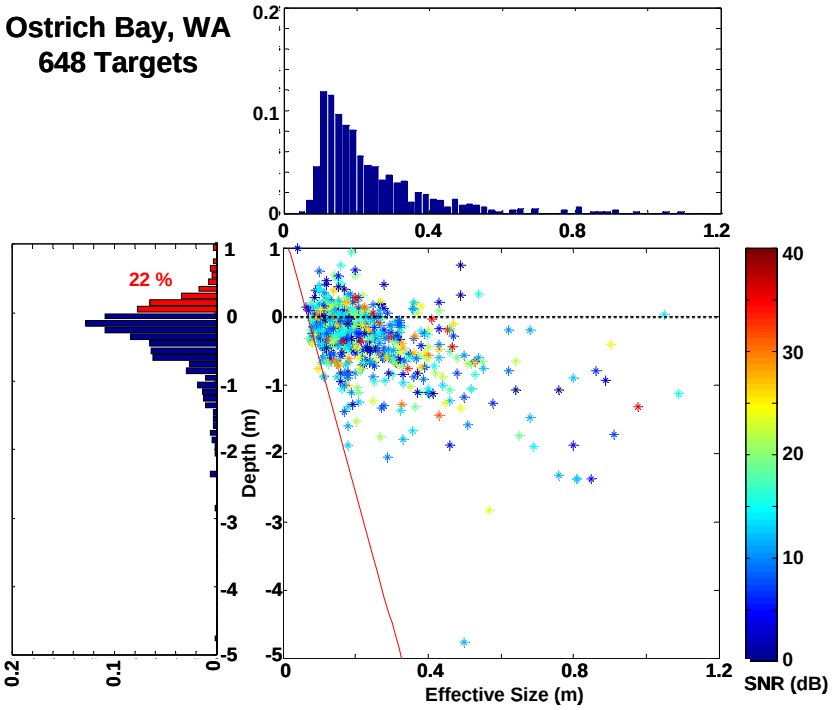

Figure 6.5d. Data from MTA site Ostrich Bay plotted as depth of target center versus effective size, with size and depth histograms. Target points are color coded by SNR. Red line is estimate of detection cutoff due to system sensitivity (see text).

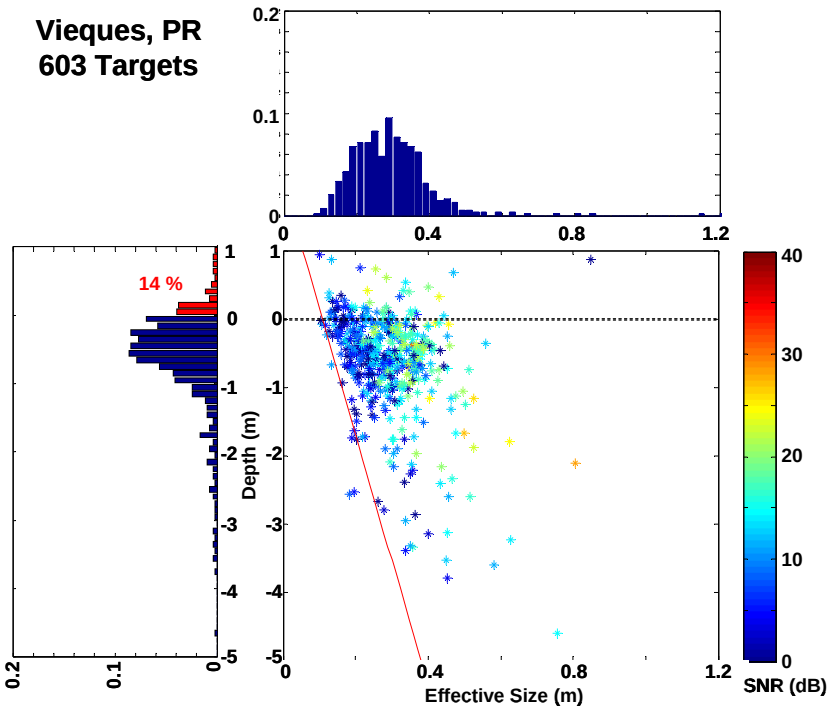

Figure 6.5e. Data from MTA site Vieques plotted as depth of target center versus effective size, with size and depth histograms. Target points are color coded by SNR. Red line is estimate of detection cutoff due to system sensitivity (see text).

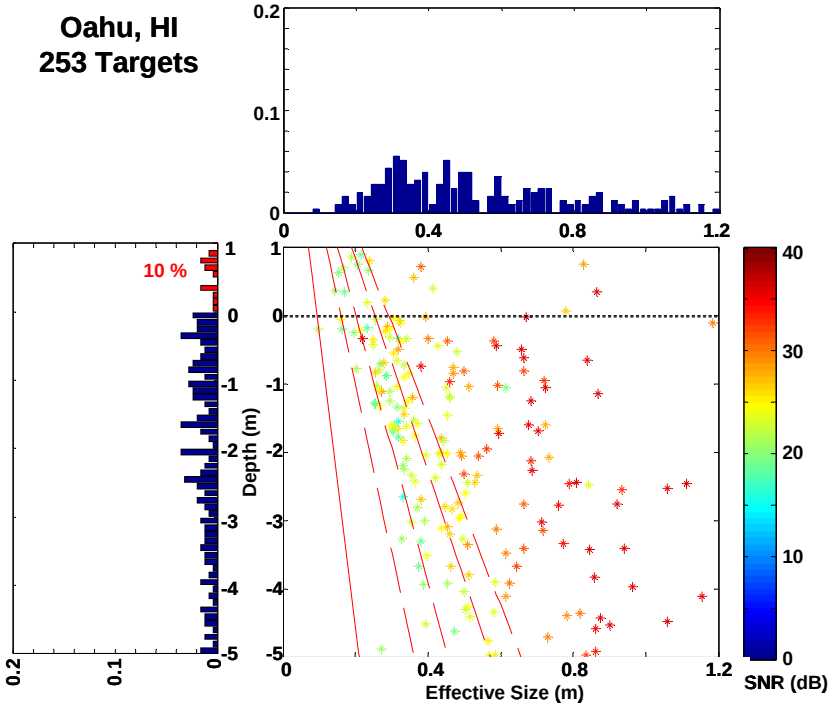

Figure 6.5f. Data from TG site Oahu plotted as depth of target center versus effective size, with size and depth histograms. Target points are color coded by SNR. Solid red line is estimate of detection cutoff due to system sensitivity, with dashed lines at different SNR (see text).

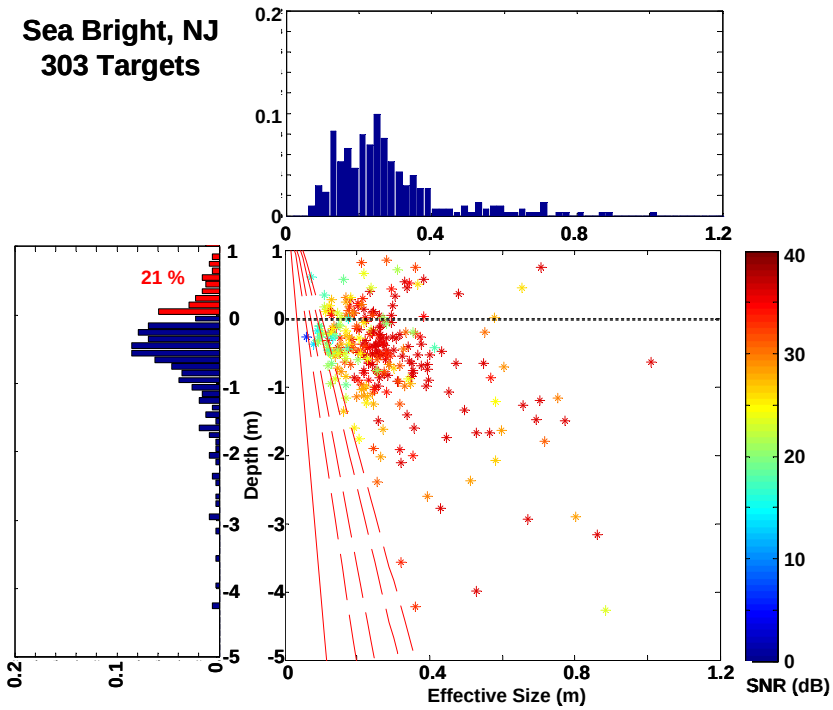

Figure 6.5g. Data from TG site Sea Bright plotted as depth of target center versus effective size, with size and depth histograms. Target points are color coded by SNR. Red line is estimate of detection cutoff due to system sensitivity, with dashed lines at different SNR (see text).

field B_0; a survey that achieves a noise level of N_S, with an Earth field B_S, will have a cutoff slope of:

$$\eta_S = \eta_0 \left(\frac{N_0 B_S}{N_S B_0} \right)^{1/3}, \qquad (2)$$

assuming that the same detection threshold was used as in the reference. The point where the cutoff line intersects the depth axis will be the sensor height above the bottom for the survey. So moving the sensor one meter higher from the bottom will shift the cutoff line up one meter, but not change the slope (at least not directly, the slope will be changed if the noise is reduced by increasing the offset from the bottom through equation 2.) The solid red lines on all of the plots in Figure 6.5 were calculated this way using the noise levels (Table 4.1), Earth field, and tow depths (Table 3.1) from each site. The reference values used were: 1 nT for N_0, 55500 nT for B_0, and -30 nT/m for η_0. The target data from all of the MTA sites are consistent with the calculated cutoff, even though there is significant variation in the parameters site to site. For the TG data sites, Figure 6.5 f and g, the calculated cutoff is still shown as a red solid line but dashed lines are added with SNR 5, 10, 20, and 30 dB worse than calculated from the observed noise level. These curved can be calculated by increasing the noise term in equation 2, but it is more likely that what actually changed in the survey is that a higher detection threshold was used. For these two surveys the actual cutoff appears to be 5 to 10 dB worse than the calculated cutoff line, suggesting the threshold was similarly higher than that used in the MTA

surveys. As noted above the TG analysis was performed by a different operator than the MTA analysis; also the objective in the TG surveys was to look for larger items, which would justify the higher threshold. This is also suggested by the SNR numbers for the targets which have a minimum at about 20 dB in the TG data. The spread of target data in SNR is consistent with the SNR cutoff lines, for instance the last dashed line at 30 dB is consistent with the cutoff for high SNR (red) targets.

The forgoing discussion suggests a relatively simple method to determine the system requirements for a given survey, based on the need to detect objects of a certain size and expected maximum burial depth. For a given site the Earth's field will be fixed and the slope of the detection cutoff line as a function of noise level can be calculated using equation 2 and the reference parameters given in the previous paragraph. The intercept with the burial depth axis should be the expected sensor height from the bottom. Sensor height and noise level can be traded off to some extent to achieve the required detection performance. Conversely, after a survey is performed, equation 2 can be used with the actual noise level and sensor height, to determine the range of objects that should have been detected, and those that are likely to be missed.

An example of using the above equations for sensitivity analysis, based on the data shown in Figure 6.6, will be used to illustrate several key features of underwater magnetometer surveys. In the figure, the expected performance of three different survey systems is shown. The blue line is the expected performance based on the noise level (1.2 nT) and average tow height (1.5 m) achieved in the MTA survey at Ostrich Bay. The slope of the line is determined from equation 2 to be -28 (using 55500 nT for B_S), and it intercepts the vertical axis at the tow height, 1.5 m. A survey system that achieves this performance should detect objects above and to the right of the blue line. The green line is the expected performance based on parameters from the TG survey at Oahu (noise level, 0.2 nT, and average height from the bottom of 4 m). For comparison purposes the same B_S is used for all three lines. The slope of the green line from equation 2 is -51, which is steeper than the blue line, and it intercepts the vertical axis at 4 m. The region shaded light blue represents the region of this space where the blue system can detect targets that would not be seen by the green system. Similarly, the light green shading represents the region where the green system has better performance. Effective size for several common munitions items are marked on the figure. The blue system can detect 60 mm munitions lying on the bottom, or partially buried, as may occur in areas with hard rock or sand bottoms. The green system will be not be able to detect targets of this size. If the targets are larger, say 155 mm, then the green system will have better performance. It can detect these items at significantly greater burial depths, which may occur in areas with soft mud bottoms. For targets of roughly 110 mm size, the performance of the two systems is equal.

The above example of a performance trade between two types of underwater magnetometer systems represents a general trend. Towed systems that attempt to remain close to the bottom (like the MTA system) will generally have higher noise than those that are designed to fly higher off the bottom (like the TG system). The MTA will do a better job detecting small targets; where the proximity matters most. Systems with lower

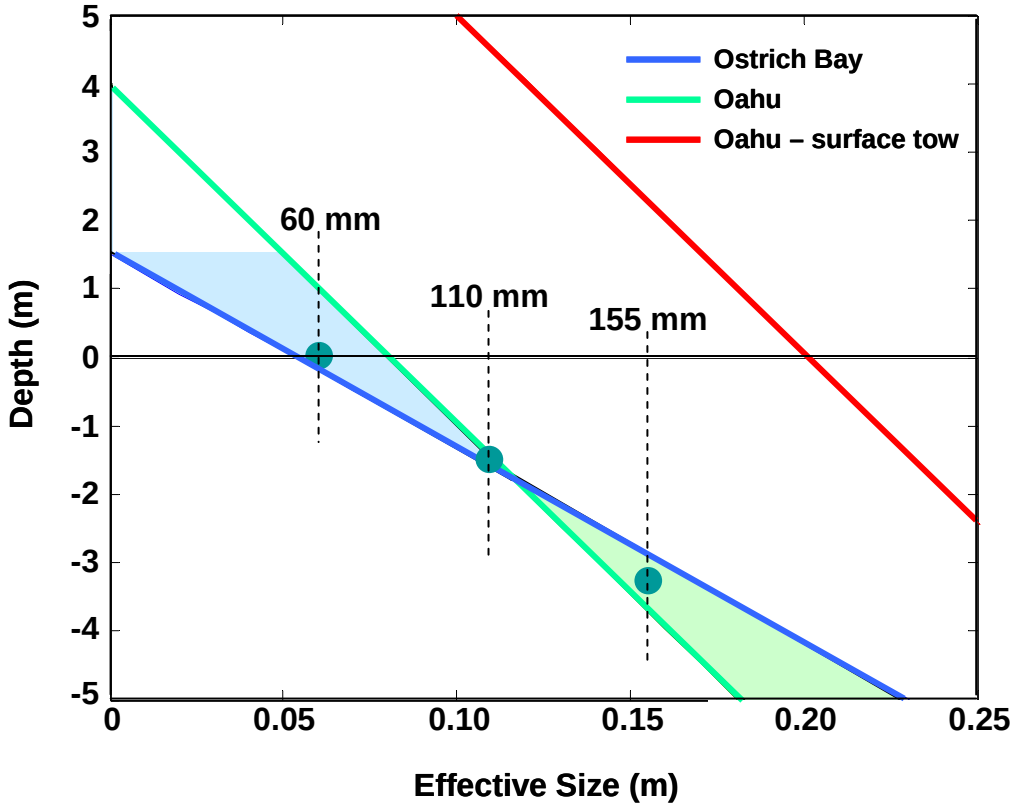

Figure 6.6. Example of sensitivity analysis (see text for explanation).

noise will be better at detecting larger munitions items when they are deeply buried. Going too far from the bottom however, will not work well. The red line in Figure 6.6 is the expected performance for a TG system that is towed at 10 m from the bottom. Such a system can only detect very large targets. In water this deep, or deeper, it is important that some effort be made to decrease the range from the sensor to the bottom. Of course the optimal system would have its sensors close to the bottom, and have low noise. Unfortunately, this is not typically possible since the closer the sensor gets to the bottom, the more the small fluctuations due to inhomogeneities in the material making up the bottom effect the sensor. Unless the bottom is atypically quiet magnetically a tradeoff as illustrated in Figure 6.6 is always needed.

7.0 Target Areal Densities

The seven survey sites all contained significant numbers of ferrous targets, but the areal density of the targets varied greatly, both in different parts of the same site, and between sites. The raw averages of the areal density for each site are shown in Table 7.1. In sites with blanket coverage surveys the area is the estimated area covered by the 2-dimensional mapped data that were used for target detection. In cases where line surveys were performed the coverage width of a typical line was estimated based on the instrumented width of the sensor platform (for MTA data), or on the tow height from the bottom and the expected detection range (for TG data). The coverage width was then multiplied by the total length of the tow lines used in the analysis to estimate the area covered. The total number of targets was then divided by the coverage area to produce the areal density (number of targets per hectare) listed in the table. Calculated this way the average densities are fairly uniform over the sites (except for Lake Erie, of which more below). Also note that not all sites are included. Protocols used for analysis at some of the sites resulted in uneven coverage of targets over the survey area. This was especially true in areas where there were large numbers of targets; these areas tended to be sampled statistically rather than exhaustively.

The average site density as calculated above hides considerable variation within some of the sites; the Lake Erie site is a case in point. The area surveyed included the impact area for an artillery test range, the periphery of the impact area, and areas far outside the expected impact zone. Individual transect lines often cut through all three of these areas. Automated target picking software was run with a fixed threshold and produced 5344 “possible targets” over 238 hectares of surveyed area (the numbers listed in Table 7.1). The number of automatically selected targets is much larger then the 779 listed in Table 2.1 and used throughout the rest of this report (the smaller number came from an operator assisted analysis of a subsection of the total survey area). Within the impact area the target density is on average about 85 targets per hectare, with some transects containing more than 250 targets per hectare in the impact zone (similar high target densities were also seen in the area surrounding an old working pier at the Ostrich Bay site). In regions well away from the impact area, the target density drops to approximately 2.4 per hectare. Further offshore, in a region that is popular with recreational fishermen, and which may also contain range related targets that are migrating to deeper water, the density is a little higher at 4.5 targets per hectare. Thus, within this one site there are distinct areas where the density of ferrous targets varies by two orders of magnitude.

All of the underwater areas surveyed were selected because they were expected to contain significant numbers of possible UXO targets. So perhaps it is not surprising that many targets were found. It is worth noting however, that targets were found everywhere surveying was done, even away from expected areas of target concentration, albeit at reduced density. As is seen in land surveys in areas that have had long human habitation, there is an irreducible background of cultural objects even in seemingly remote underwater areas. Thus, discrimination of typical underwater clutter (abandoned anchors, crab pots, pieces of pipe and wire, etc.) from potential UXO is critical for improving the cost efficiency of underwater cleanup activities, no less than on land.

NAME	AREA (hectare)	TARGETS	HEIGHT FROM BOTTOM (m)	DENSITY (#/ha)
Sea Bright, NJ	29	303	2.0	10.4
Duck, NC	62	432	1.0	7.0
Lake Erie, OH	238	5344**	1.5	22.5
Vieques, PR	79	532	2.0	6.7
Oahu, HI	25	253	4.0	10.1

** - automated target calls

Table 7.1. Raw target densities.

8.0 Conclusions

This report collects and reexamines data from a number of underwater magnetometer surveys in order to assess what has been learned about the underwater UXO problem. In general there are no features of the underwater UXO problem that are simplifications compared land surveys. All of the same problems must be addressed, with the added difficulties of marine logistics and only indirect access to the Earth's (underwater) surface.

Ferrous object that were large enough to be detected were found in all of the surveyed areas of all of the sites included in this study. The density of targets ranged from a low of several per hectare, to a high of over 250 per hectare; typical densities were around 10 per hectare. At every site two thirds to three quarters of the targets were completely buried in the bottom (according to their parameter fits), with the remaining objects lying on the bottom or partially buried. This result suggests that survey methods that are not sensitive to buried objects will be unable to detect the majority of potential UXO, even though they will detect significant numbers of objects.

Compared to typical ground UXO surveys, the distribution of estimated size for underwater surveys showed a higher percentage of large objects. It is not clear if this difference is due to the typically larger caliber of marine munitions, or to other causes. There is also a dearth of the smallest sized objects in the underwater surveys; this is likely because the reduced sensitivity of the surveys did not allow detection of small objects (mostly due to greater stand-off range, see below).

A typical problem with underwater surveys with towed instruments is the need to keep a large enough stand-off from the bottom to avoid snagging the sensors. The MTA system used active depth control to allow average stand-offs as small as 1 meter, at the expense of increased magnetic noise due to the servos that move the control surfaces. The alternate approach of the TG systems was to control the sensor depth via the tow speed; this allowed a significant reduction in magnetic noise, at the cost standoff ranges of several meters. Which of these strategies is most effective depends on the requirements of the survey. The MTA approach (higher noise and less stand-off) is more effective at detecting smaller objects at greater depth, while the alternate approach allows detection of larger objects at greater depth. A semi-empirical expression (equation 2) was developed to estimate the region of size-depth space that can be accessed based on the expected magnetic noise level, the sensor standoff from the bottom, and the local Earth's field. This simple expression appears to explain much of the observed variation in detection between the survey sites. Using this equation the performance effects of system design tradeoffs, such as the noise-height trade described above, can be determined.

Another issue that needs to be addressed in underwater surveys is estimation of the geographic position of the sensors. Direct GPS positioning is generally not possible, since the GPS antenna cannot operate underwater. Both of the systems described here used GPS antennas mounted on the tow vessel, and auxiliary measurements and motion models to estimate the offset from the GPS antenna to the underwater sensors. In this report data from the MTA survey at Duck, NC, was used to estimate the accuracy of

these sensor position estimates. The results indicated an rms accuracy of about 0.4 m for repeated tows over a set of large deep targets. This accuracy is sufficient to support reacquisition of individual objects. Maintaining this level of accuracy in the sensor position will become more difficult for systems operating in deeper water with larger offsets from the well determined GPS position.

Performing underwater UXO surveys with the type of systems described in this report is considerably more expensive than doing similar surveys on land. The survey costs will increase steeply for systems that can operate in deeper water. The two primary reasons for the higher costs are that boats are more expensive to buy, crew, and maintain than similarly capable ground vehicles, and that boats are slower than ground vehicles so the surveys take longer. It is difficult to imagine a technology shift that would make it substantially cheaper to do underwater magnetic surveying, unless fully autonomous surveying becomes possible (eliminating the cost of the surface vessel, crew and survey team). Other UXO detection technologies (sonar for example) may change to cost paradigm; but the forgoing analysis indicates that at a minimum any successful underwater UXO technology must be able to detect fully buried objects.

This report has concentrated on underwater surveys, but of course the other parts of the UXO remediation problem remain. Reacquisition of objects detected in underwater surveys is generally performed by UXO trained divers with special equipment. Much technology development could be applied here to improve reacquisition methodologies and documentation, and to reduce cost. Regardless of how objects are detected or reacquired, most ferrous underwater objects are not potentially dangerous UXO, but are scrap metal. Removing these objects while treating them as UXO will represent the most significant cost item in underwater remediation (as it does on land). Therefore the key development emphasis should remain on technologies that can discriminate potentially hazardous targets from scrap.

9.0 References

1. Pope, Joan, et al., “Pilot Study to Characterize Ordnance Contamination within the Sea Bright, New Jersey, Sand Borrow Site,” CERC-96-8, December, 1996

2. DeProspo, Douglas, et al., “Localization and Characterization of Underwater UXO,” in Conference Proceedings of the UXO Forum 1997, Nashville, Tennessee, May 1997

3. “Marine Towed Array Technology Demonstration at the Former Naval Duck Target Facility,” ESTCP Project MM2003-24, Final Report, November 21, 2005

4. “The MTA UXO Survey and Target Recovery on Lake Erie at the Former Erie Army Depot,” ESTCP Project MM2003-24, Final Report, January 25, 2007

5. “Demonstration of the Marine Towed Array on Ostrich Bay at the Former Naval Ammunition Depot – Puget Sound, June 12-30, 2006,” ESTCP Project MM2003-24, Final Report, September 20, 2008

6. “Demonstration of the Marine Towed Array on Bahia Salinas del Sur Vieques, Puerto Rico, June 1-30, 2007,” ESTCP Project: MM2003-24, Final Report, February, 16, 2009

7. “Marine Towed Array Demonstration Blossom Point Research Facility, October 2007”, ESTCP Project MM-0328.

APPENDIX A: Analysis report Sea Bright, NJ

Introduction

This is a brief writeup that summarizes the analysis of an underwater magnetic investigation that was conducted by the U.S. Army Corps of Engineers, Waterways Experiment Station in support of the Sea Bright beach nourishment project for the U.S. Army Engineer District, New York. The objective of the analysis is to characterize the data set to determine noise levels, survey statistics and quality of the dipole fits.

Equipment:

The data were collected along 6 three mile long north-south tracks (parallel to the shoreline) which were spaced 200 feet apart. The water depth in the collection area is 40-50 feet. The data were gathered at 10 Hz using two Geometrics Model G-880 Cesium vapor magnetometers separated by a distance of 2 meters and mounted on a submersible platform. The sensor array was flown at a nominal altitude of 1 to 2 meters above the sea floor and monitored to within 1 centimeter. A fiberglass hulled, aluminum decked and housed research vessel was used to tow the sensor platform at a forward speed of 3 to 4 knots with a 54 meter setback distance.

Data

Figure 1 shows the locations of the magnetic survey lines. Alternate lines are plotted in black and red to facilitate tracking individual lines to their respective line number. Figure 2 shows an example of the magnetic and height above sea floor data for a portion of line 95258462. The final diurnal corrected magnetic data received for the two sensors are shown in the top two panels as red traces. As evident in the figure, geology significantly affects the magnetic data for this profile and similar geologic activity is seen in the other transect lines. The low frequency geologic signature was removed using a combination of splines and filters to create the final leveled magnetic data plotted as blue traces. The bottom panel shows the typical variation in height above the sea floor.

To aid in picking anomalies the analytic signal was created from the magnetometer data. The analytic signal is the square root of the sum of the gradients in three directions:

$$AS = \sqrt{\left|\frac{\partial B}{\partial x}\right|^2 + \left|\frac{\partial B}{\partial y}\right|^2 + \left|\frac{\partial B}{\partial z}\right|^2} \quad ,$$

where the z-gradient is formed from the data in the (x,y) plane by upward continuation in the Fourier domain:

$$\frac{\partial B(k)}{\partial z} = kB(k), \quad k = 2\pi / \lambda \quad .$$

The analytic signal is a positive quantity and can easily be thresholded for target detection. The grid was filtered with two passes of a 9 point hanning filter and anomalies were picked using the Blakely method which is a target picking option found in Oasis montaj™. The Blakely method compares the value of each grid cell with values of the eight (8) nearest grid cells in four directions (along the row, column, and both diagonals). If the grid value is greater than the input threshold and all the nearest grid cells are lower, it is selected as a peak. A threshold of 5nT/m was used to automatically select potential anomalies. The threshold has set at a value that selected most of the anomalies without spurious picks due to noise in the data. The anomalies were manually reviewed by posting their locations on the gridded image of the data and simultaneously analyzing the profile data. Some anomalies were removed due to multiple picks over the same anomaly while other anomalies were added that were below the selected threshold but were clearly potential targets. This resulted in a total of 303 anomalies which are overlain on the survey lines in Figure 3. Studies show that for an expected average sized object (10 inch caliber) and a 1.7m sensor height above sea floor we can assume the array will detect objects up to about 4.1 meters to each side of the survey track. 35.6 km of survey data were analyzed which results in an area of 29.2 hectares. Assuming that all 303 anomalies correspond to targets gives an average target density of 10.4 per hectare.

Figure 4 shows the locations where noise statistics were calculated for the survey area. The noise was estimated by calculating the standard deviation of the data contained within a 15 meter box surrounding the locations displayed on the map. The boxes were located in areas that contained various noise levels and were void of any anomaly picks. Table 1 tabulates the noise statistics for these data. The noise ranged from 0.04nT to 0.402nT with an average of 0.120 for the different noise windows. This average value was used to calculate the signal to noise ratios which are shown in Figure 5. The signal to noise was calculated using an algorithm that is part of the Oasis montaj software suite. The signal strength of an anomaly is calculated as the sum of the squares of all points with a user defined window and above the background. The signal to noise is calculated as the normalized ratio of the signal strength over the noise. The value is converted to dB and presented in histogram format.

Figure 6 shows the standard deviation of the sensor height above the sea floor. In general, the standard deviations hover around 0.5m which indicates the array was kept at a fairly constant height above the sea floor.

Figure 7 to Figure 9 show the distributions of the fit coherence, fit depth and fitted effective size respectively. The magnetometer data were analyzed using the inversion routines in IDL which assume a dipole source. The magnetic dipole model inverts for the location (X_0, Y_0, Z_0), magnetic moment, and orientation angles (*declination and inclination*). Initial guesses for the fit parameters are determined internally within the

code based on the measured signature. The fit coherence, which is the squared correlation coefficient between the measured and modeled data, is a goodness of fit metric. In general the majority of anomalies gave good fit coherences (>0.95). Most of the anomalies appear to be buried in the top 1m of the sea floor. Several of the anomalies show negative depths which could indicate they are due to objects on the surface of the sea floor or long objects that are protruding from the sea floor or they could point to problems with altitude sensor or errors induced by the pitch and roll of the sensor platform. The apparent dipole equivalent radius which is approximately ordnance caliber clusters between .1m and .4m which equate to caliber rounds between 4inch and 16inch. These sizes area consistent with the size of objects recovered during a limited raking operation (Figure 10).

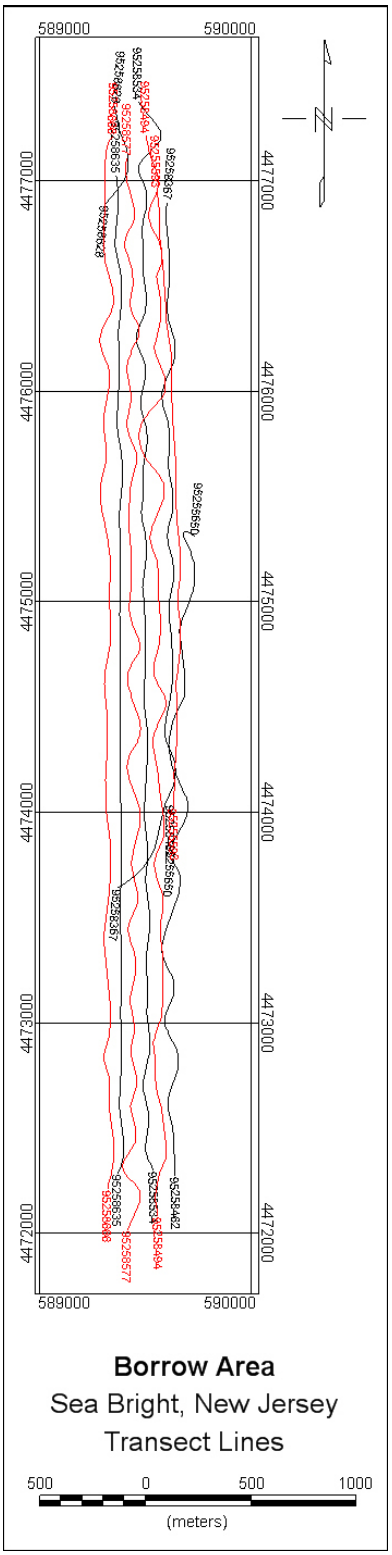

Figure 1. Magnetic survey transect line locations. The lines are plot in black and red to facilitate correlating the lines to the respective line numbers.

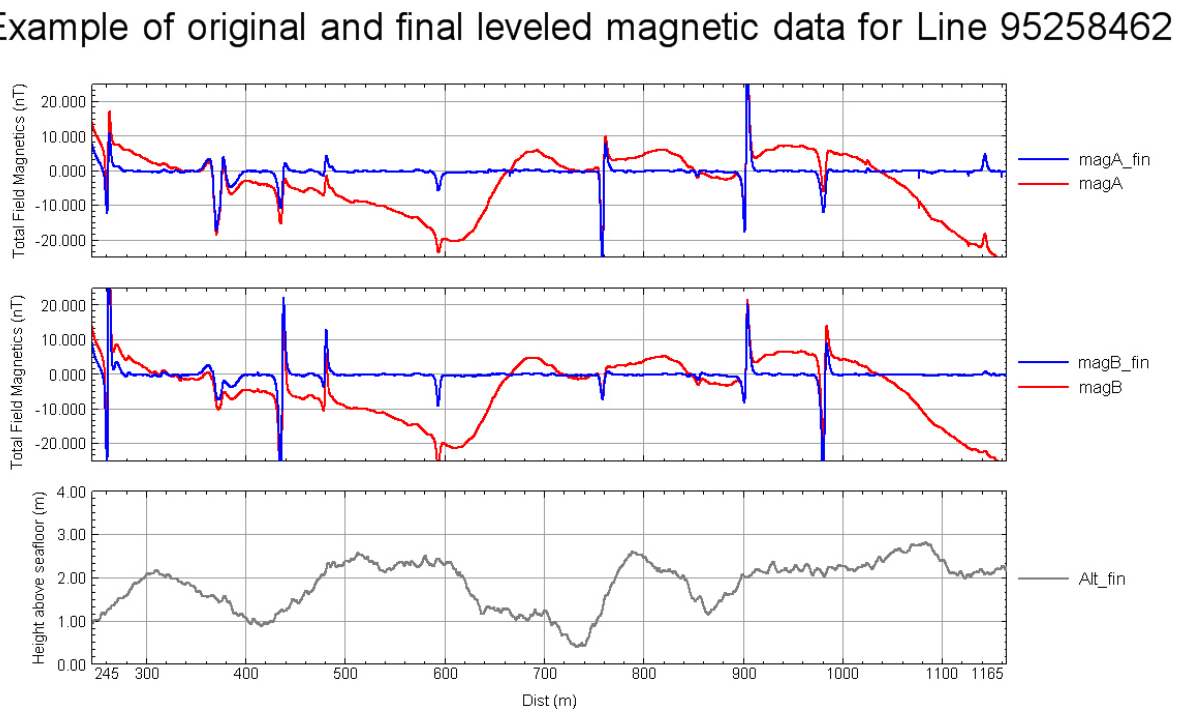

Figure 2. Final leveled magnetics with magnetic sensor locations overlain.

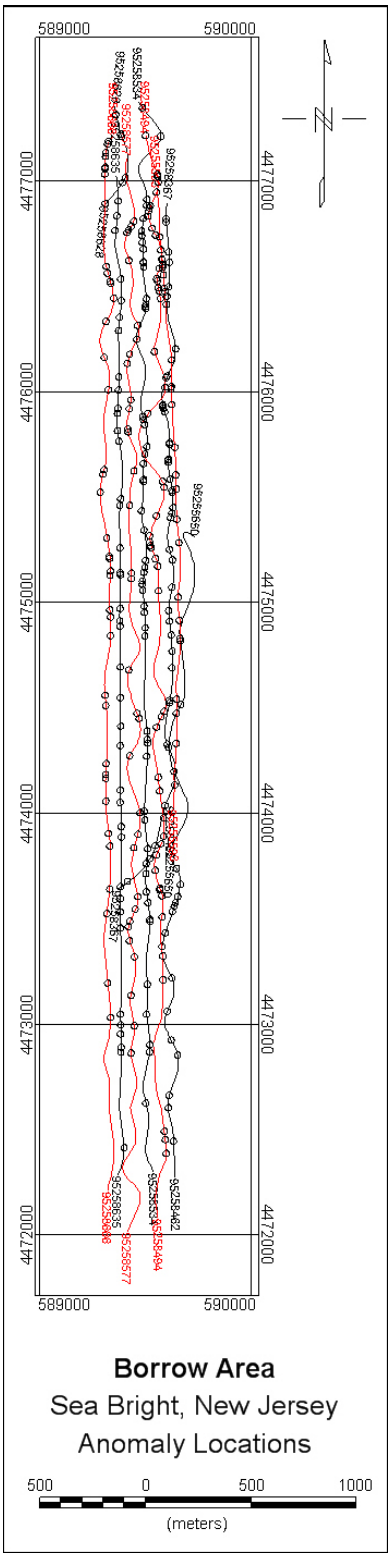

Figure 3. Anomaly locations plotted as circles overlain on the survey lines.

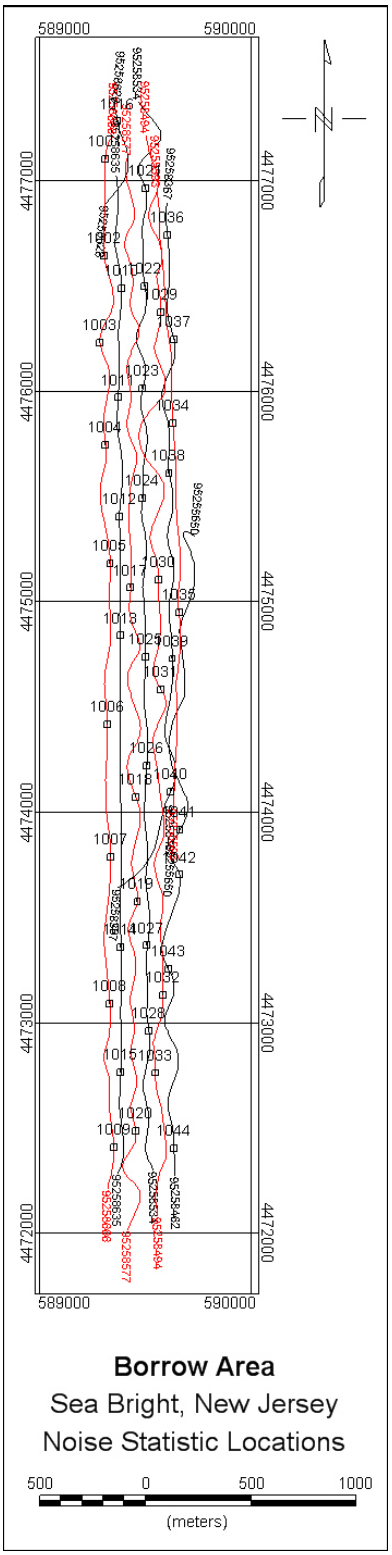

Figure 4. Survey lines with noise statistic locations overlain. The magnetic data located within 15meters of the boxes shown were used to derive the noise level statistics.

Table 1. Total Field Magnetics statistics for each of the defined noise regions in Figure 4

Noise region	Minimum (nT)	Maximum (nT)	Mean (nT)	Std.dev. (nT)	# of points
1001	-1.13	0.07	-0.064	0.165	152
1002	-0.37	0.21	-0.09	0.156	150
1003	-0.35	0.09	0.006	0.09	187
1004	-0.09	0.06	-0.008	0.05	150
1005	-1.08	0.23	-0.008	0.178	115
1006	-0.08	0.11	0.003	0.037	140
1007	-0.11	0.23	0.029	0.07	156
1008	-0.08	0.1	-0.013	0.04	122
1009	-0.14	0.11	-0.055	0.055	167
1010	-0.4	0.16	-0.067	0.103	157
1011	-0.09	0.14	0.016	0.059	149
1012	-0.31	0.29	0.001	0.162	133
1013	-0.21	0.28	0.01	0.114	114
1014	-0.29	-0.06	-0.143	0.06	127
1015	-0.22	0.14	-0.101	0.089	145
1016	-0.46	0.7	-0.014	0.307	151
1017	-0.01	0.12	0.057	0.033	143
1018	-0.25	0.22	-0.038	0.153	136
1019	-0.42	0.44	0.003	0.248	210
1020	-0.27	0.17	-0.094	0.096	184
1021	-2.26	0.37	0.004	0.31	226
1022	-3.03	0.38	0.053	0.402	217
1023	-0.48	0.48	-0.058	0.19	204
1024	-0.28	0.2	-0.059	0.139	201
1025	-0.24	0.13	-0.003	0.091	180
1026	-0.31	0.11	-0.104	0.137	181
1027	-0.04	0.3	0.125	0.079	182
1028	-0.21	0.12	-0.018	0.087	183
1029	-0.1	0.07	0.008	0.04	133
1030	-0.13	0.13	0.018	0.076	154
1031	-0.25	0.05	-0.071	0.082	219
1032	-0.21	0.05	-0.111	0.056	144
1033	-0.19	0.16	-0.07	0.085	161
1034	-0.4	0.2	-0.133	0.149	207
1035	-0.68	0.16	-0.122	0.213	220
1036	-0.1	0.17	0.043	0.071	138
1037	-0.37	0.4	-0.063	0.173	242
1038	-0.33	0.32	-0.085	0.165	216
1039	-0.15	0.42	-0.003	0.099	206
1040	-0.1	0.17	-0.004	0.062	192
1041	-0.06	0.21	0.066	0.077	152
1042	-0.19	0.09	-0.055	0.067	212
1043	-0.18	0.13	-0.006	0.065	218
1044	-0.35	0.12	-0.06	0.112	222
Averages			-0.029	0.120	

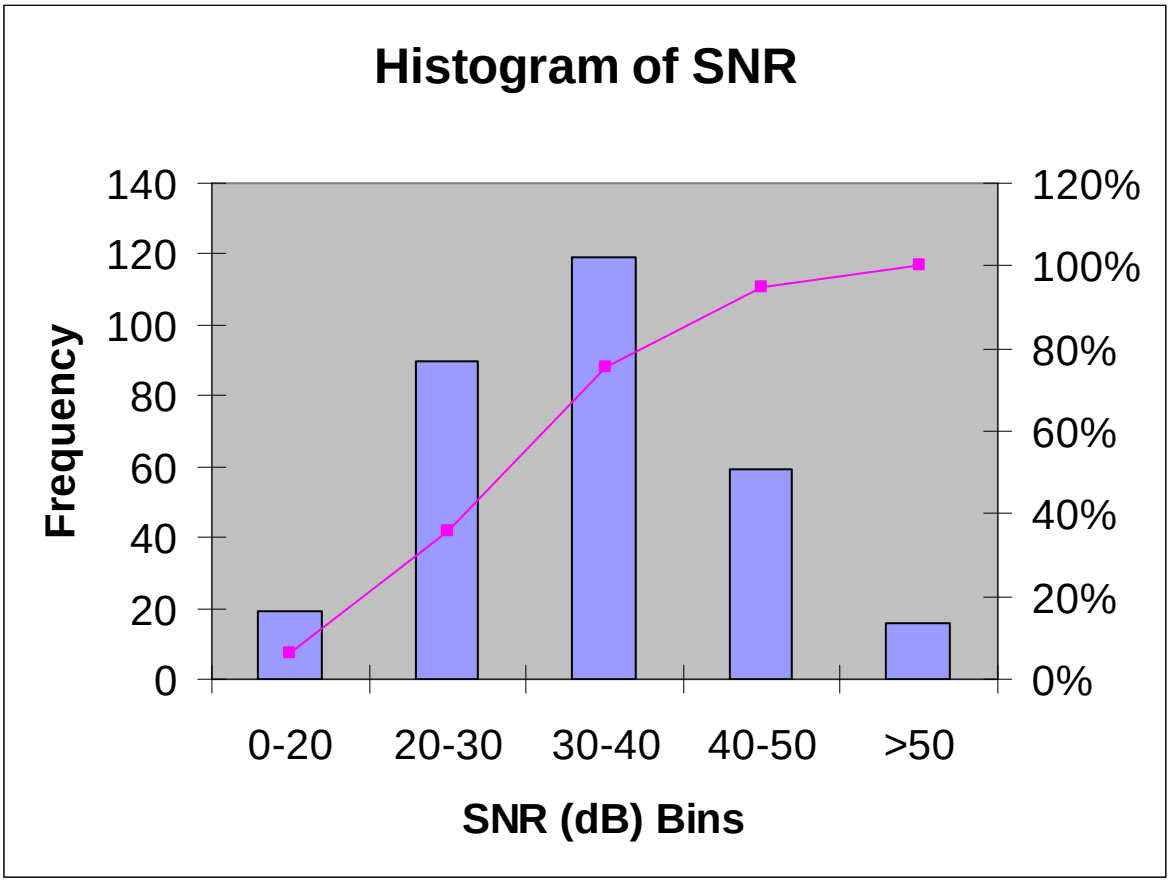

Figure 5. Distribution of Magnetic Signal to Noise ratios for all anomalies

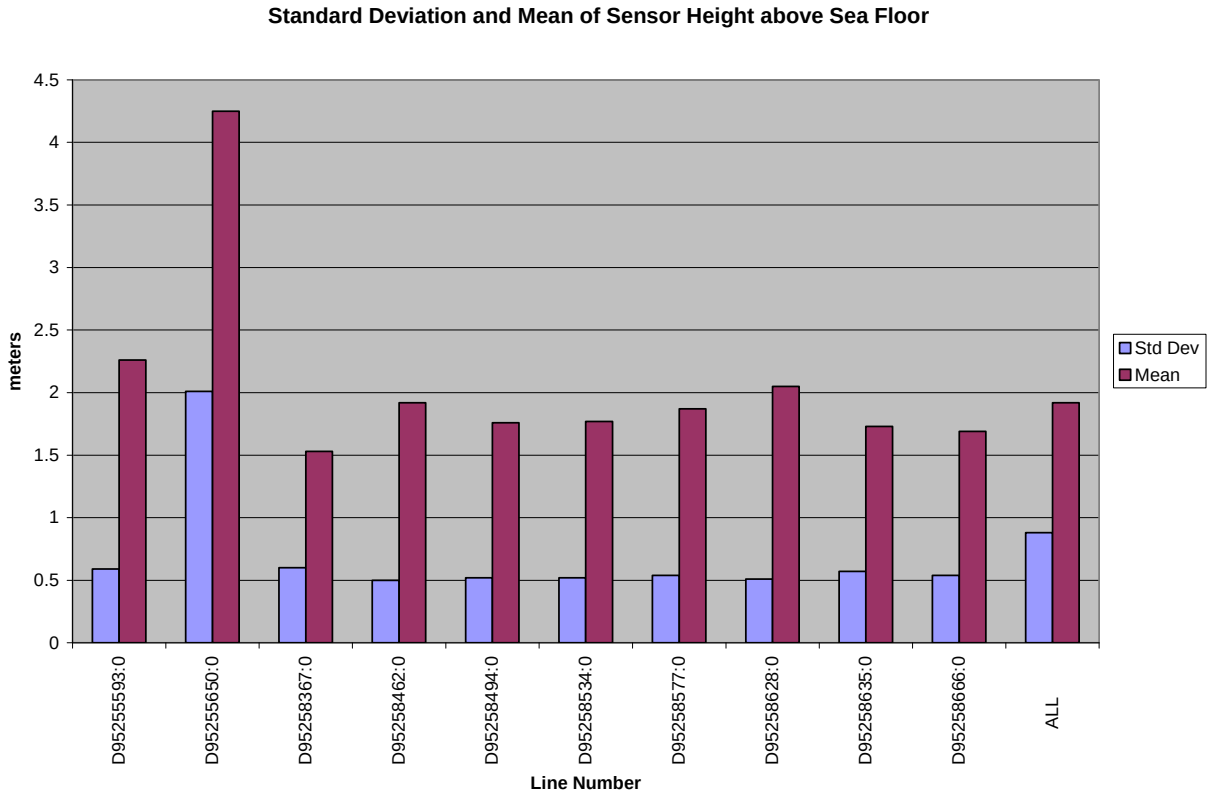

Figure 6. Standard deviation and mean of the sensor height above the sea floor.

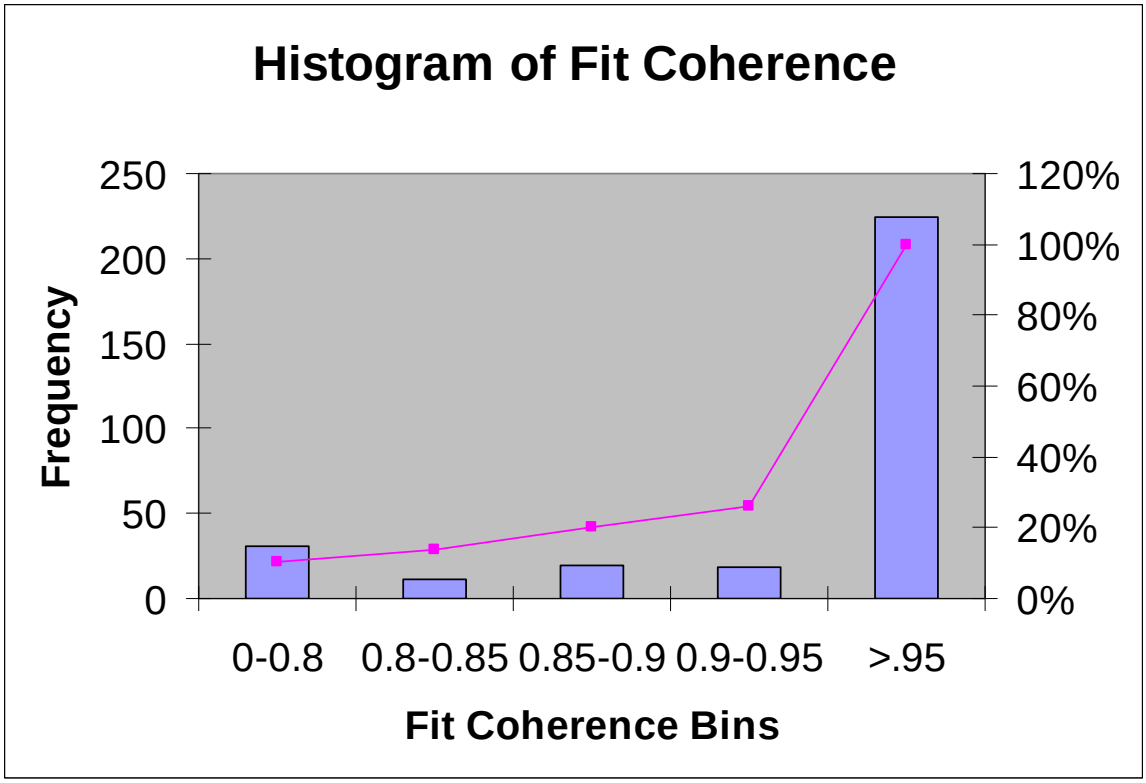

Figure 7. Histogram of the fit coherence output from the dipole inversions

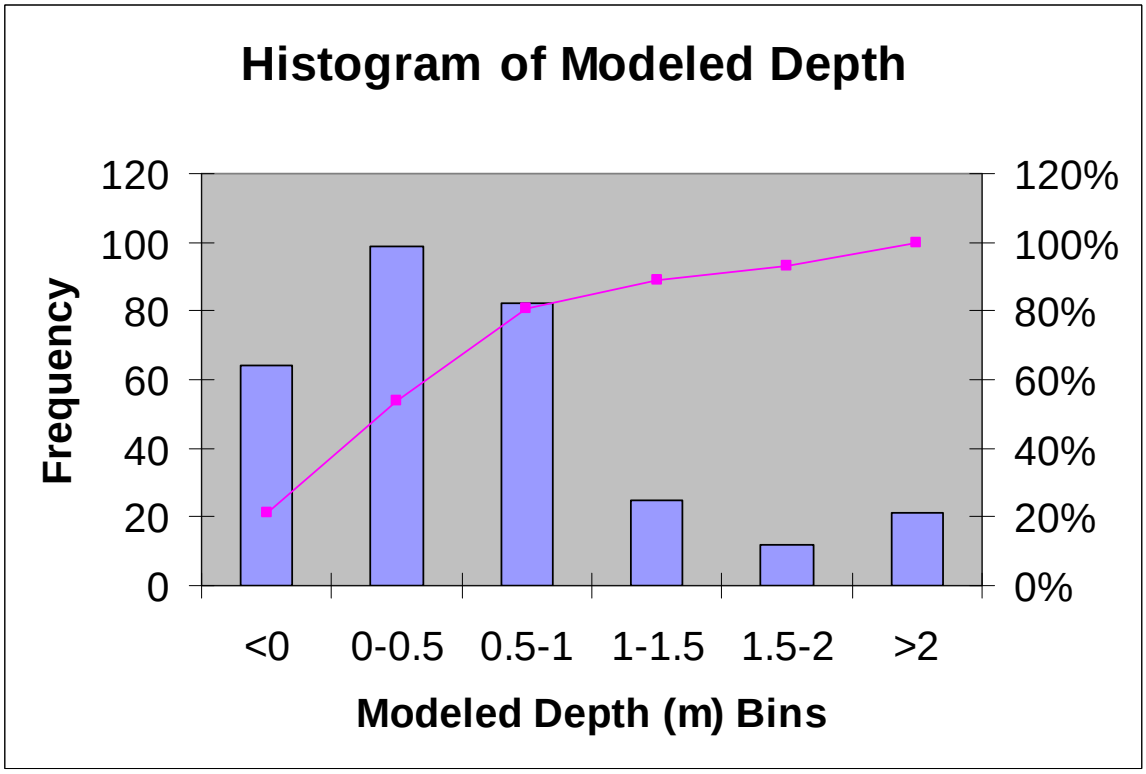

Figure 8. Histogram of fitted depth output from the dipole inversions

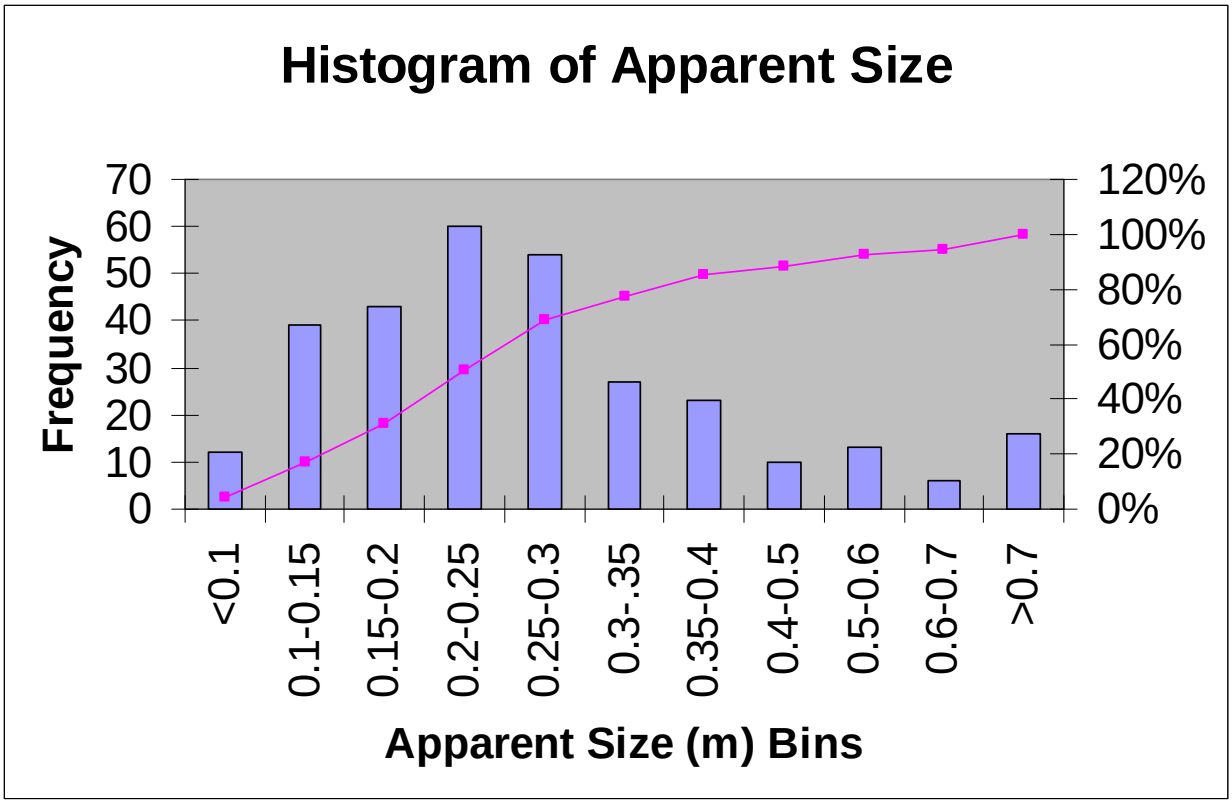

Figure 9. Histogram of the effective size output from the dipole inversions.

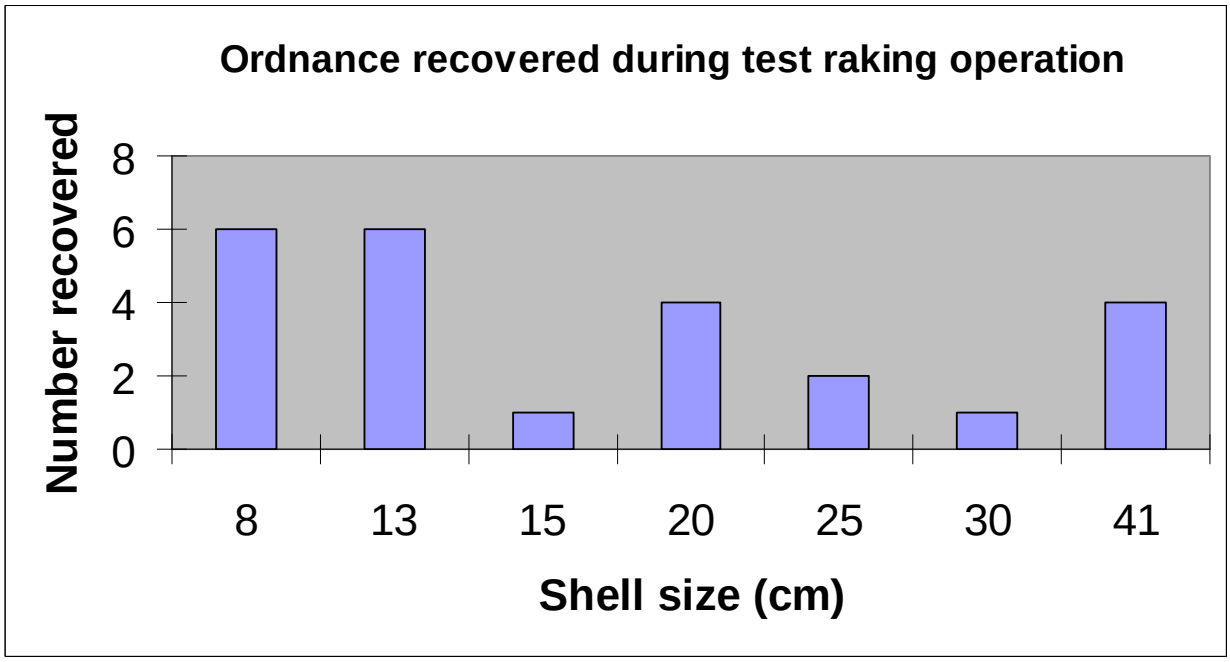

Figure 10. Distribution of ordnance recovered during a test raking operation.

APPENDIX B: Analysis report MFS Hawaii survey

Introduction

This is a brief writeup that summarizes the analysis conducted on the Marine Transverse Gradiometer (TG) Data acquired during survey at the Navy Degaussing range on Oahu, Hawaii. The objective of the analysis is to characterize the data set to determine noise levels, survey statistics and quality of the dipole fits.

Equipment:

Geometrics 1.2 Meter Transverse Gradiometer consisting of:

- G-882, S/N 882156, with depth and altimeter
- G-882, S/N 882186 with depth
- Gradiometer tow bar assembly
- 61 Meter Clevis Tow Cable with Kellems Grip
- Power Supply and Inverter for boat operation
- DC/Data Junction Box

Magnetometer array was towed from a point on the aft deck forward of and centered between the outboard engines. Distance between the GPS antenna and the magnetometer sensors was 27 Meters.

Trimble AgGPS 132 DGPS with Parallel Steering Option DGPS provided by Omni Star GPS antenna was mounted on top of the aft part of the boat cabin for survey operations.

Compaq EVO N800c laptop computer with Windows XP Professional operating system and MagLog data logging software RS 232 data converted to USB by Keyspan 4-port USB Serial converter, model USA-49.

Data

The nominal survey line spacing was 9 meters. As mentioned above the array consisted of 2 magnetometers spaced 1.2 meters apart to almost create a full coverage survey. Figure 1 shows the final diurnal corrected magnetic data received from Geometrics. As evident in the figure, geology significantly affects the magnetic data across the entire area. The low frequency geologic signature was removed using a combination of splines and filters to create the final leveled magnetic data presented in Figure 2. The two figures also show the survey line locations to give an indication of survey coverage.

To aid in picking anomalies the analytic signal was created from the magnetometer data. The analytic signal is the square root of the sum of the gradients in three directions:

$$AS = \sqrt{\left|\frac{\partial B}{\partial x}\right|^2 + \left|\frac{\partial B}{\partial y}\right|^2 + \left|\frac{\partial B}{\partial z}\right|^2} \quad ,$$

where the z-gradient is formed from the data in the (x,y) plane by upward continuation in the Fourier domain:

$$\frac{\partial B(k)}{\partial z} = kB(k), \quad k = 2\pi / \lambda \quad .$$

The analytic signal is a positive quantity and can easily be thresholded for target detection. The grid was filtered with two passes of a 9 point hanning filter and anomalies were picked using the Blakely method which is a target picking option found in Oasis montaj™. The Blakely method compares the value of each grid cell with values of the eight (8) nearest grid cells in four directions (along the row, column, and both diagonals). If the grid value is greater than the input threshold and all the nearest grid cells are lower, it is selected as a peak. A threshold of 3nT/m was used to automatically select potential anomalies. The anomalies were manually reviewed by posting their locations on the gridded image of the data and simultaneously analyzing the profile data. Some anomalies were removed due to multiple picks over the same anomaly while other anomalies were added near perimeters and data gaps where the automatic method failed because the test relies on complete data coverage surrounding the anomaly. This resulted in a total of 253 anomalies which are overlain on the magnetic data in Figure 3. The survey area was calculated to be 25.3 hectares. For large caliber objects (>10 inch) and a 4m sensor height above sea floor we can assume the survey was essentially full coverage. Assuming that all 253 anomalies correspond to targets gives an average target density of 10.0 per hectare. This is a conservative number since smaller sized ordnance will not be detected because of the line spacing used and the 4m sensor height.

Figure 4 shows the locations where noise statistics were calculated for the survey area. The noise was estimated by calculating the standard deviation of the data contained within each box displayed on the map. The boxes were located in areas that contained

various noise levels and were void of any anomaly picks. Table 1 tabulates the noise statistics for these data. The noise ranged from 0.098nT to 0.425nT with an average of 0.219 for the different noise windows. This average value was used to calculate the signal to noise ratios which are shown in Figure 5. The signal to noise was calculated using an algorithm that is part of the Oasis montaj software suite. The signal strength of an anomaly is calculated as the sum of the squares of all points with a user defined window and above the background. The signal to noise is calculated as the normalized ratio of the signal strength over the noise. The value is converted to dB and presented in histogram format.

Figure 16 presents the height above the sea floor of the magnetic sensors as a color coded profile line map. A pseudo digital terrain model of the sea floor was calculated using the altimeter and depth sensors. The data were not corrected for changes in tide except to apply a constant offset to the repeated lines collected on the second day. The data are all relative to the water surface which is assumed to be 0. The terrain model is presented as a color contour map in Figure 17. Figure 18 shows the location of the selected lines for which altitude profile maps were generated. Figure 19 and Figure 20 present depth profiles for select lines. The actual depth values are all relative to the surface of the water with the negative values meaning depth below the water surface. The red lines represent the shape of the sea floor and the green lines show the height of the magnetic sensors.

Figure 21 presents a bar chart showing the average sensor depth and sensor height above the sea floor fro each survey line. The sum of the two components gives the water depth. Figure 6 shows the standard deviation of the sensor height above the sea floor. In general, the standard deviations hover around 0.3m which indicates the array was kept at a fairly constant height above the sea floor. Figure 23 shows the standard deviation of the sea floor relief model. The standard deviations range from about .07 to 0.4m which indicates the sea floor relief for this survey was relatively benign.

Figure 7 to Figure 9 show the distributions of the fit coherence, fit depth and fitted effective size respectively. The magnetometer data were analyzed using the inversion routines in IDL which assume a dipole source. The magnetic dipole model inverts for the location (X_0, Y_0, Z_0), magnetic moment, and orientation angles (*declination and inclination*). Initial guesses for the fit parameters are determined internally within the code based on the measured signature. The fit coherence, which is the squared correlation coefficient between the measured and modeled data, is a goodness of fit metric. In general the majority of anomalies gave good fit coherences (>0.9). Most of the anomalies appear to be buried in the top 5m of the sea floor. Some of the anomalies show negative depths which could indicate they are due to objects on the surface of the sea floor or long objects that are protruding from the sea floor. The apparent dipole equivalent radius which is approximately ordnance caliber clusters between .25m and .75m which equate to large caliber rounds (10inch to 30inch). There was no ground truth information available to confirm if these sizes are consistent with the actual items.

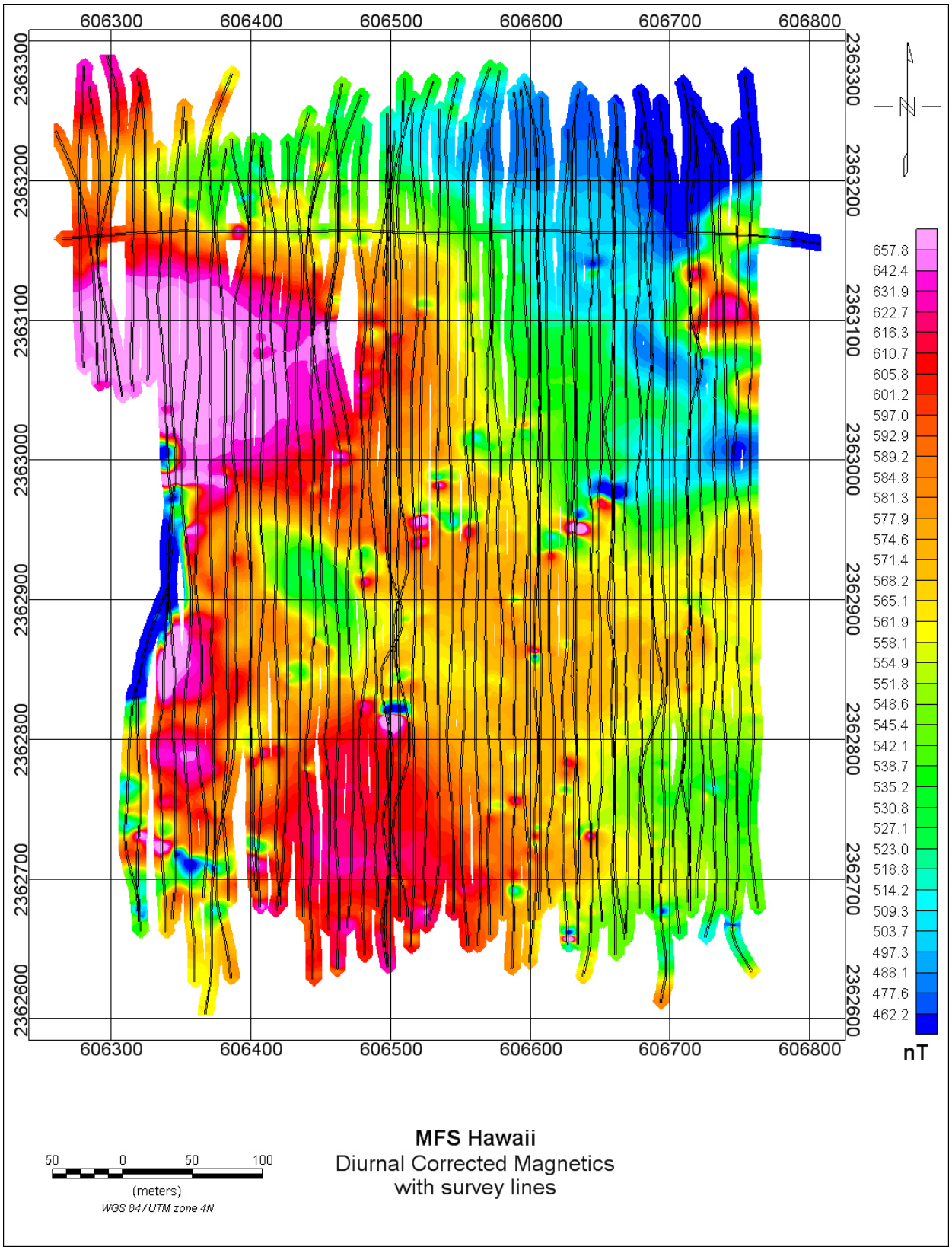

Figure 11. Diurnal corrected magnetics with magnetic sensor locations overlain. Although difficult to see, each survey line consists of two sensors spaced 1.2 meters apart.

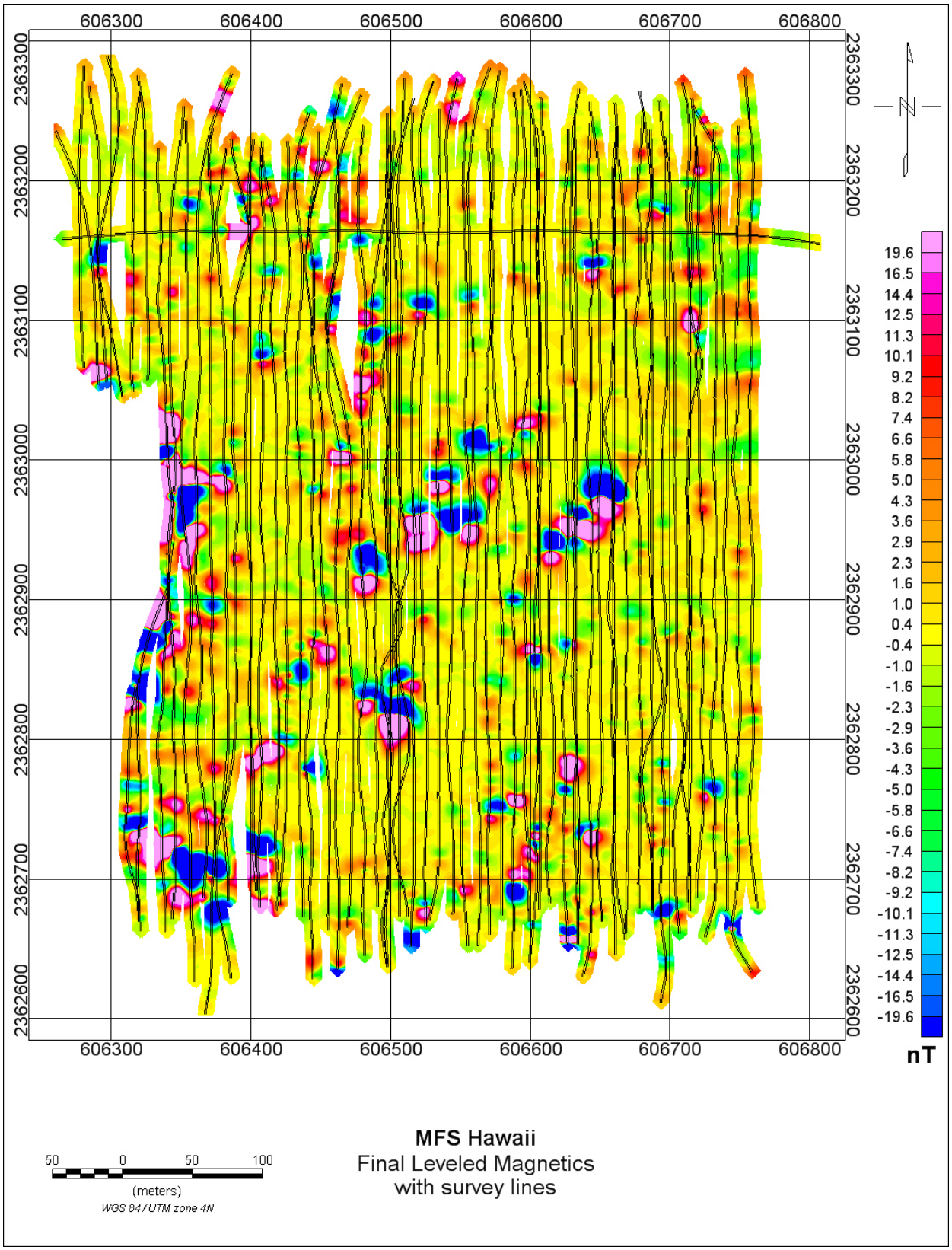

Figure 12. Final leveled magnetics with magnetic sensor locations overlain.

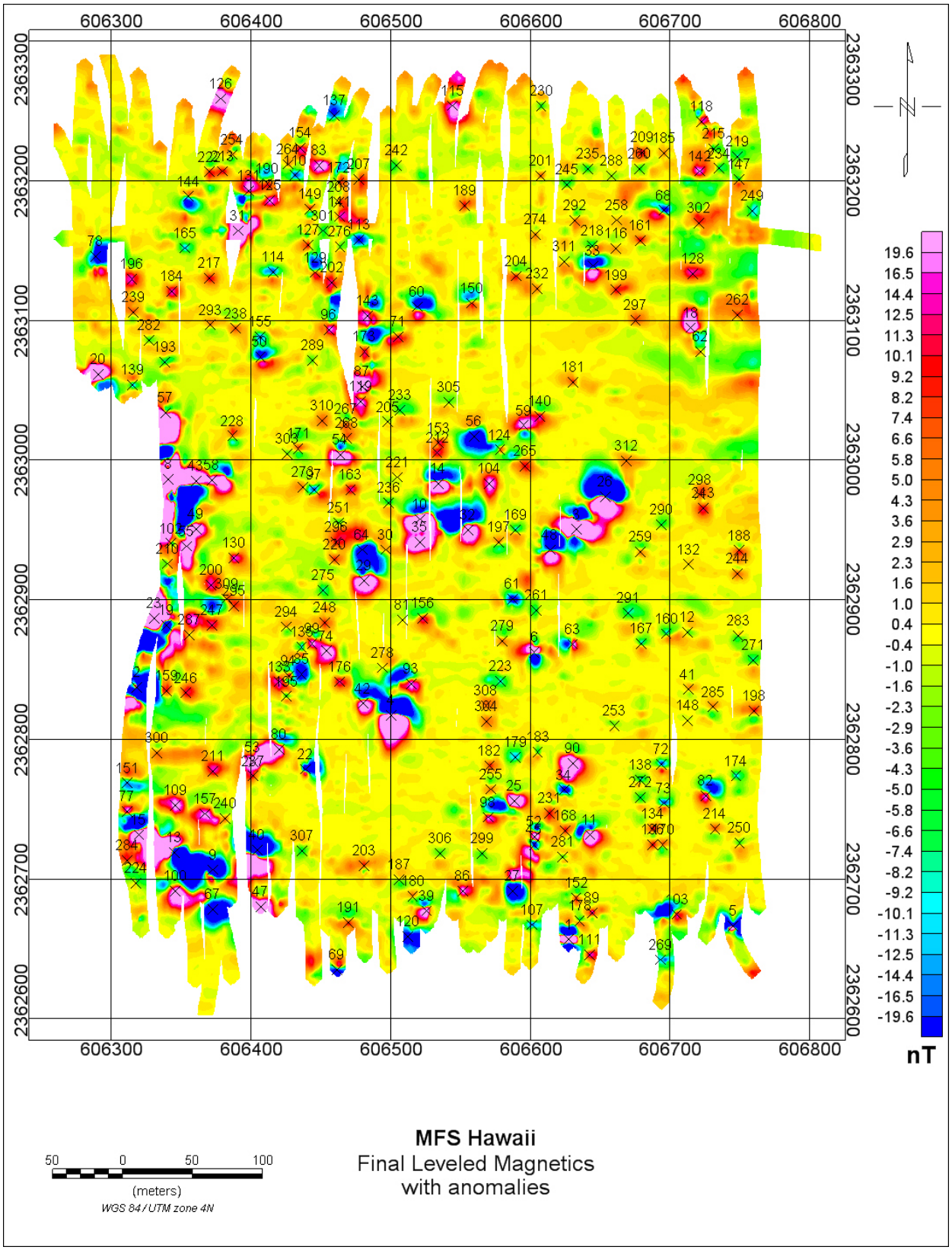

Figure 13. Final leveled magnetics with anomaly locations overlain.

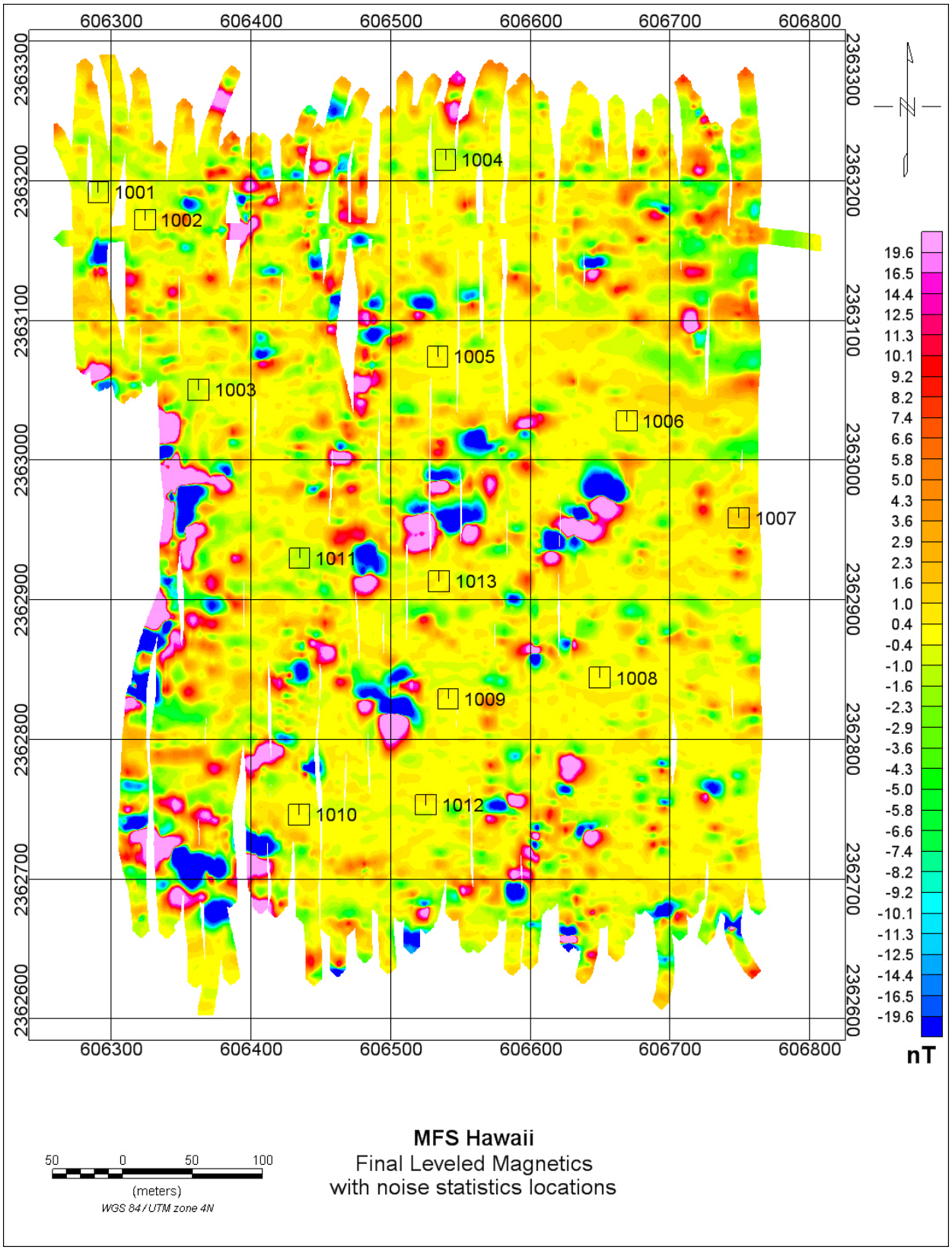

Figure 14. Final leveled magnetics with noise statistic locations overlain. The magnetic data located within the boxes shown were used to derive the noise level statistics.

Table 2. Total Field Magnetics statistics for each of the defined noise regions in Figure 4

Noise region	Minimum (nT)	Maximum (nT)	Mean (nT)	Std.dev. (nT)	# of points
1001	-0.655	0.101	-0.351	0.191	184
1002	-0.436	0.694	-0.074	0.289	124
1003	-0.874	-0.289	-0.534	0.129	140
1004	-1.226	-0.414	-0.764	0.187	266
1005	-0.643	0.599	0.045	0.322	212
1006	-0.145	0.338	0.107	0.11	130
1007	0.362	1.859	1.186	0.368	184
1008	-0.235	0.181	-0.014	0.098	219
1009	-0.146	0.687	0.2	0.196	212
1010	-0.639	0.218	-0.083	0.206	171
1011	-1.583	-0.774	-1.114	0.161	132
1012	-0.652	0.562	0.083	0.425	144
1013	0.079	0.666	0.372	0.161	138
Averages			-0.072	0.219	

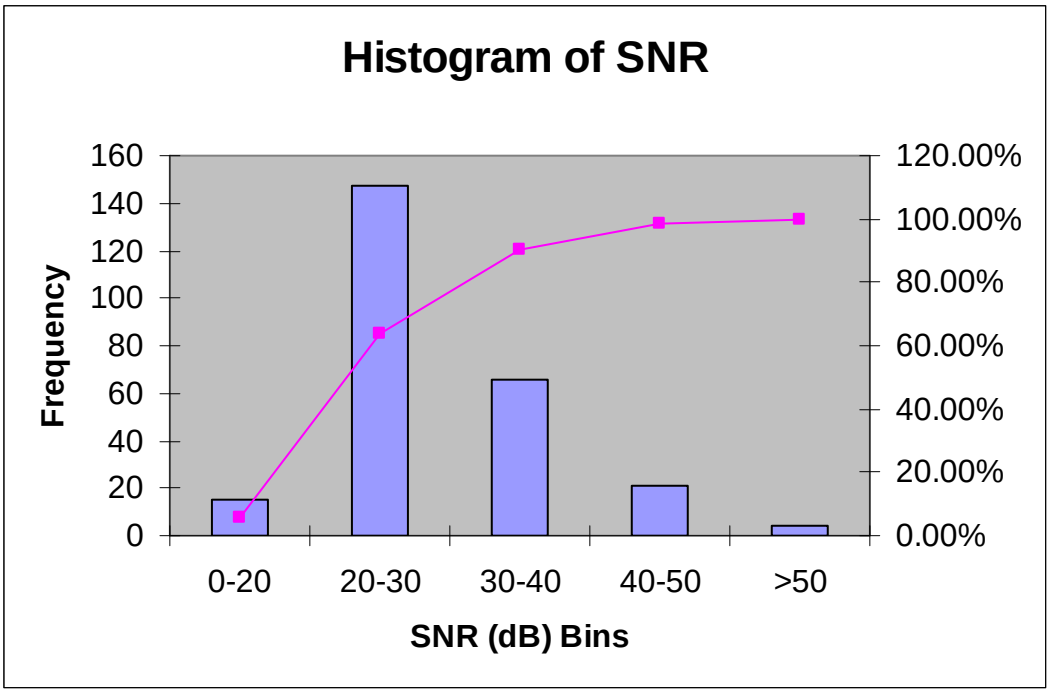

Figure 15. Distribution of Magnetic Signal to Noise ratios for all anomalies

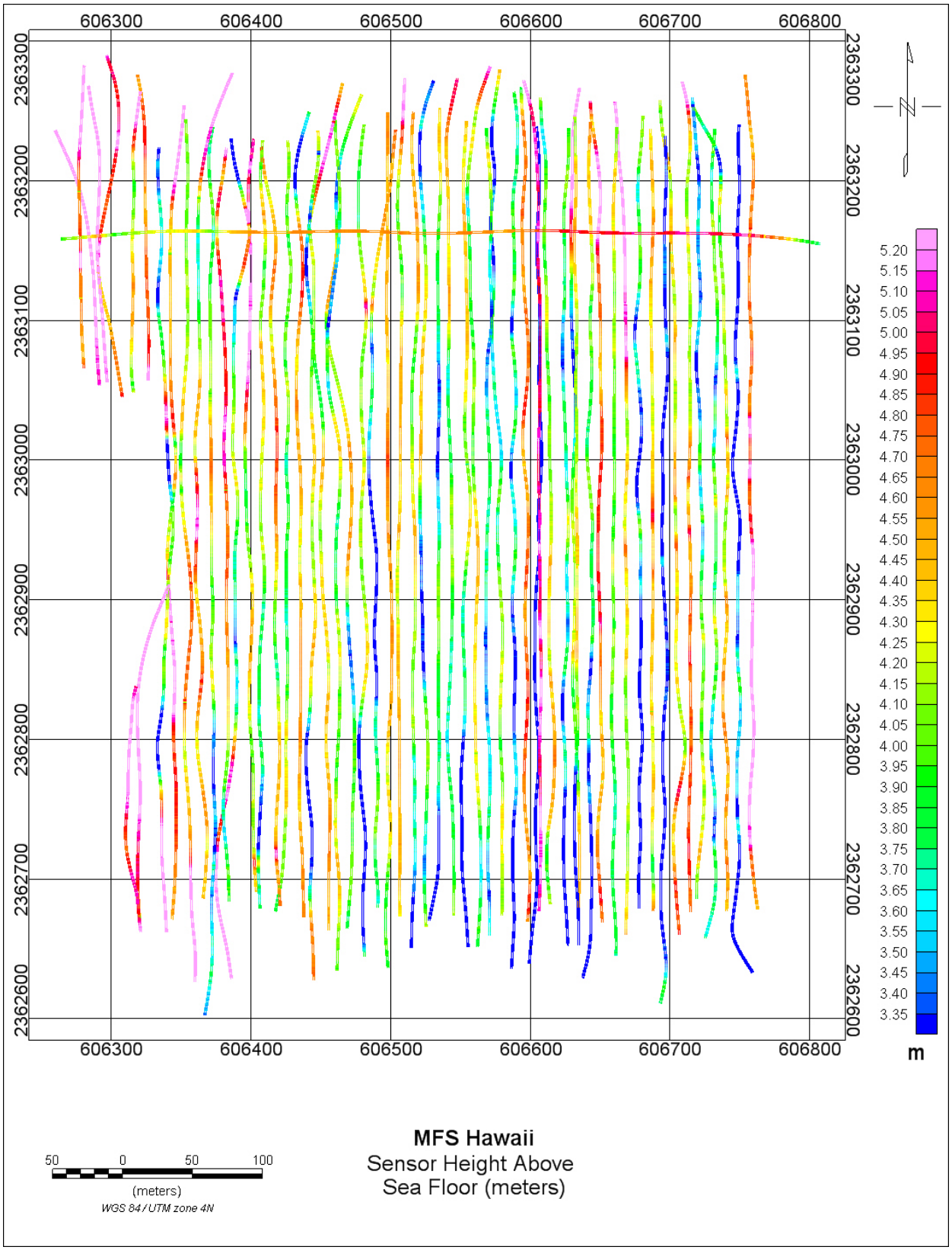

Figure 16. Height of magnetic sensors above the sea floor (meters)

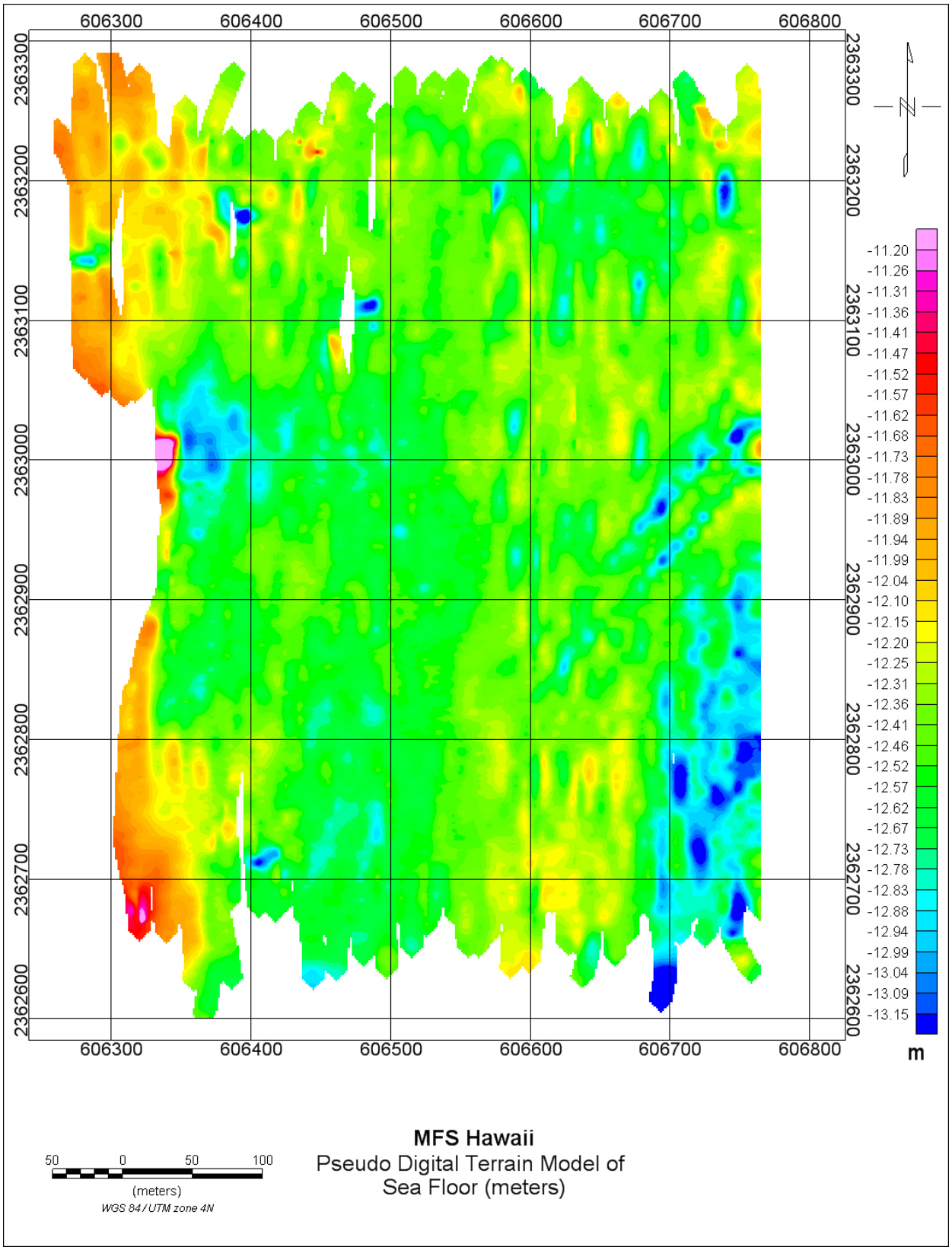

Figure 17. Pseudo digital terrain model of sea floor calculated using the altimeter and depth sensors. The data were not corrected for the changes in tide and are relative to the surface of the water which is assumed to be equal to 0.

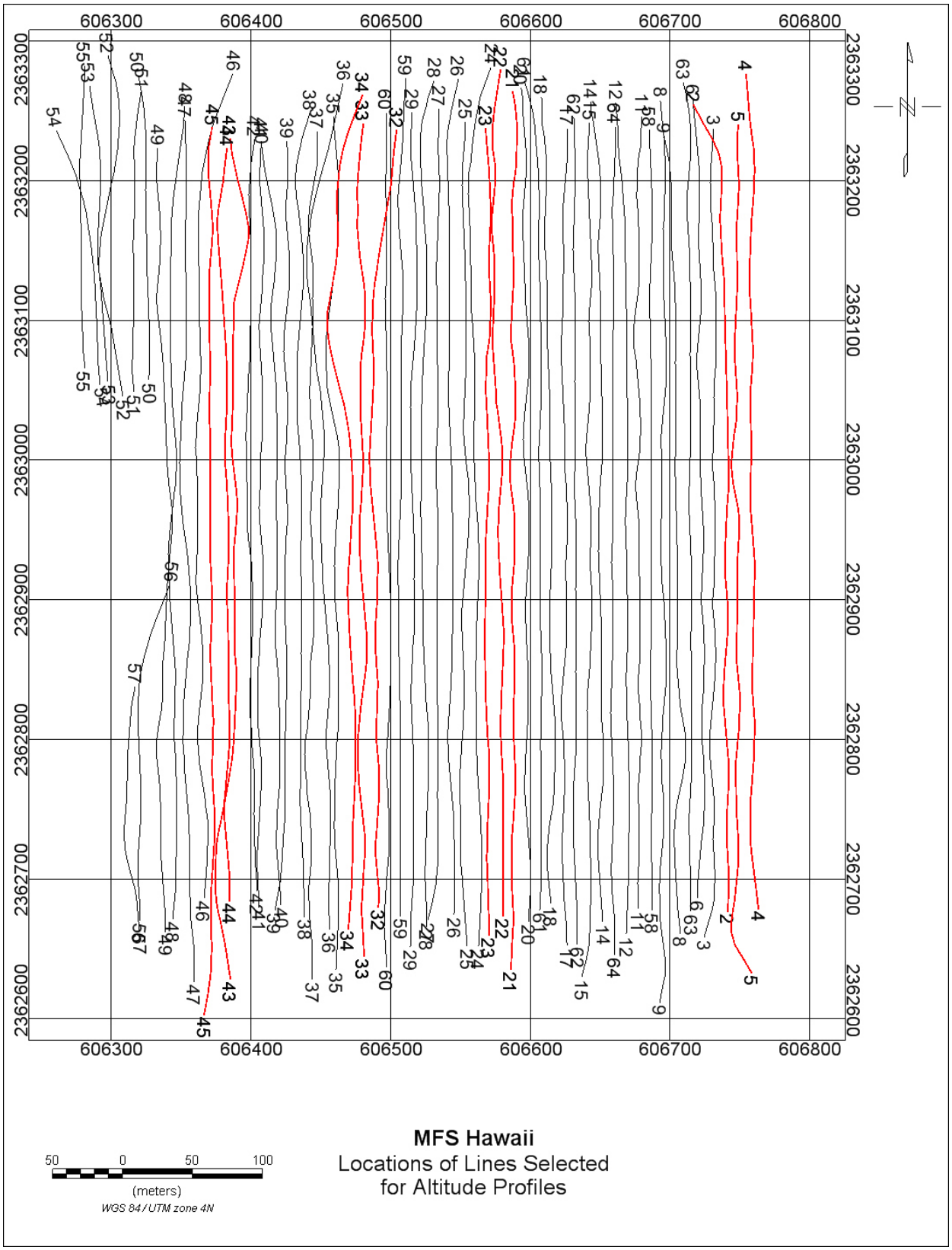

Figure 18. Map showing the location of the selected lines (red) for which altitude profile maps were generated.

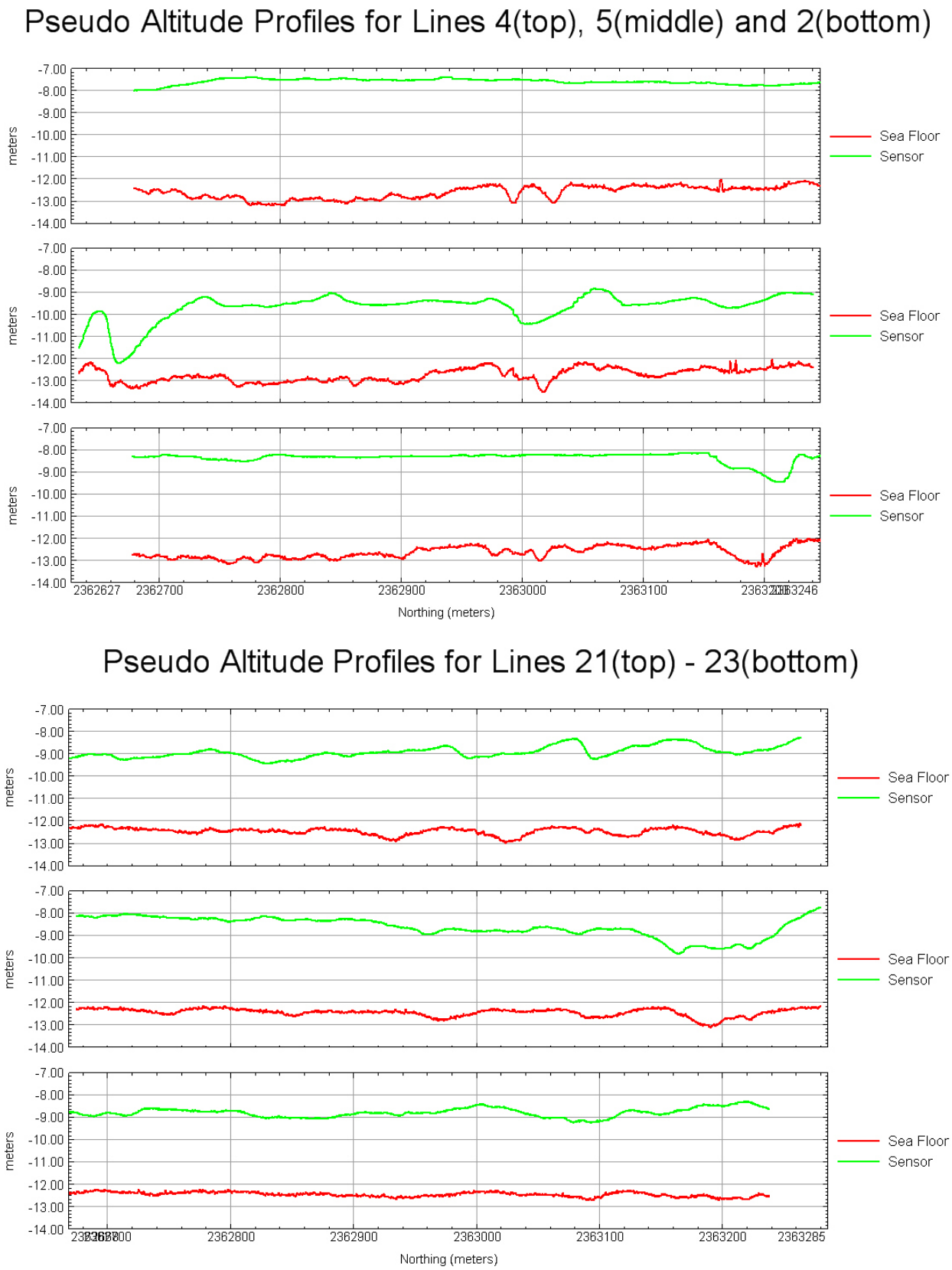

Figure 19. Pseudo altitude profiles for selected lines. The red line represents the sea floor and the green line shows the height of the sensor above the sea floor.

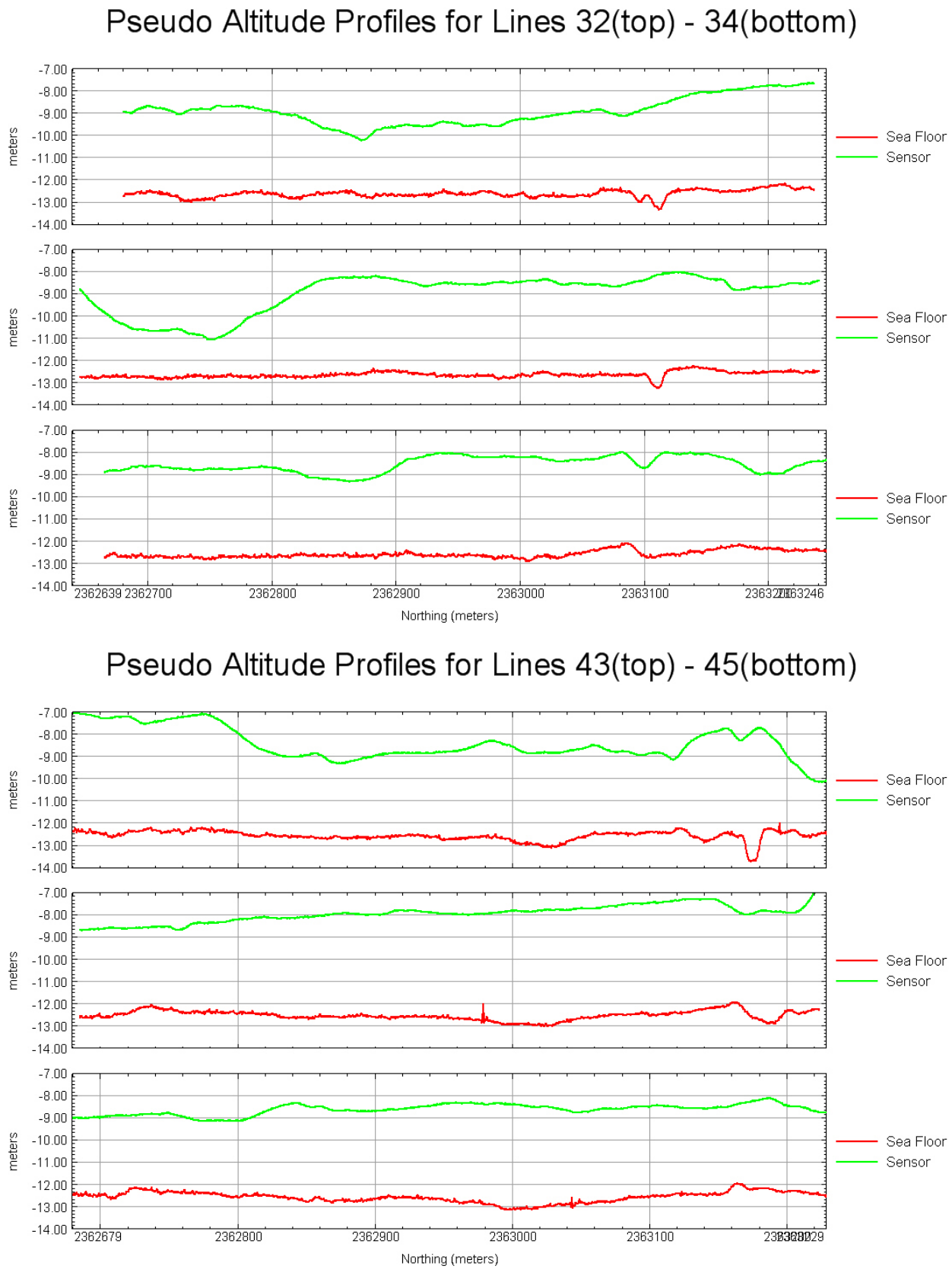

Figure 20. Pseudo altitude profiles for selected lines. The red line represents the sea floor and the green line shows the height of the sensor above the sea floor.

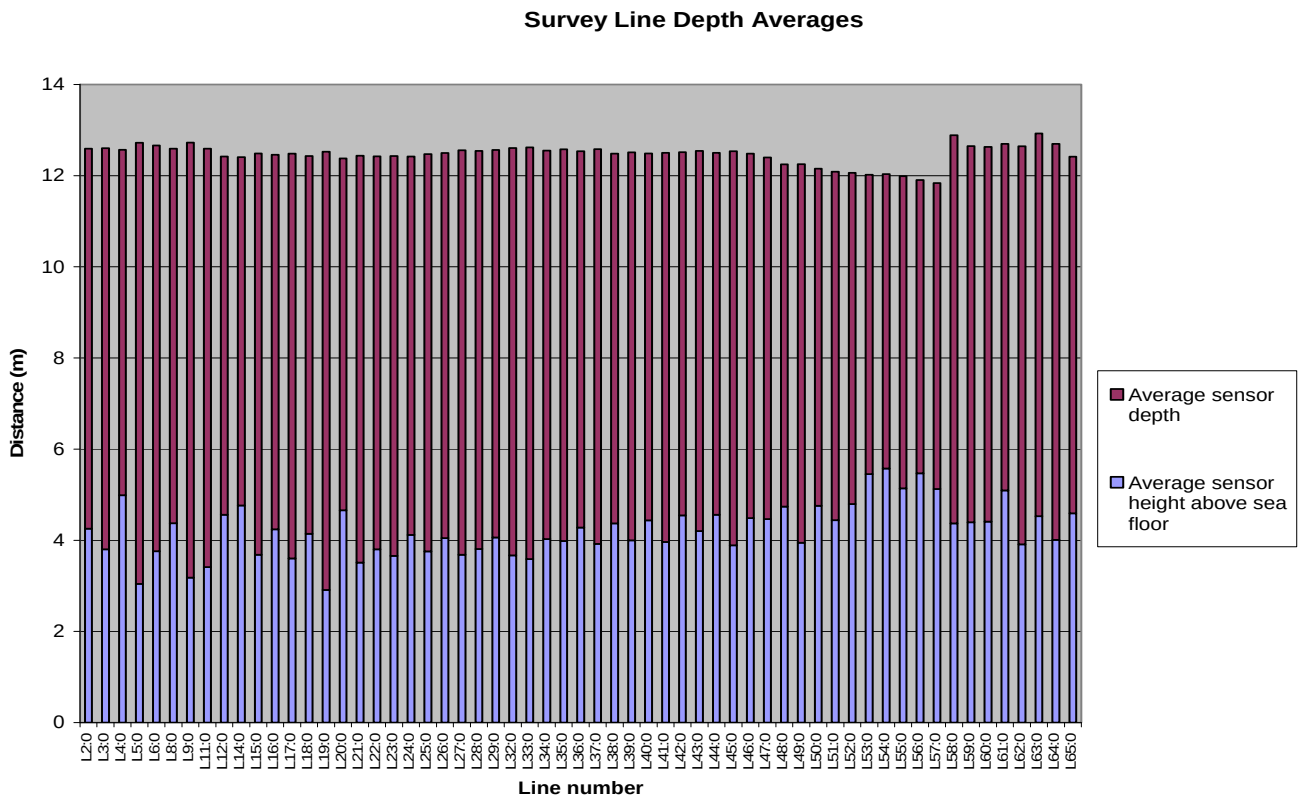

Figure 21. Average sensor depth and sensor height above the sea floor for each survey line. The sum of these two components gives the water depth.

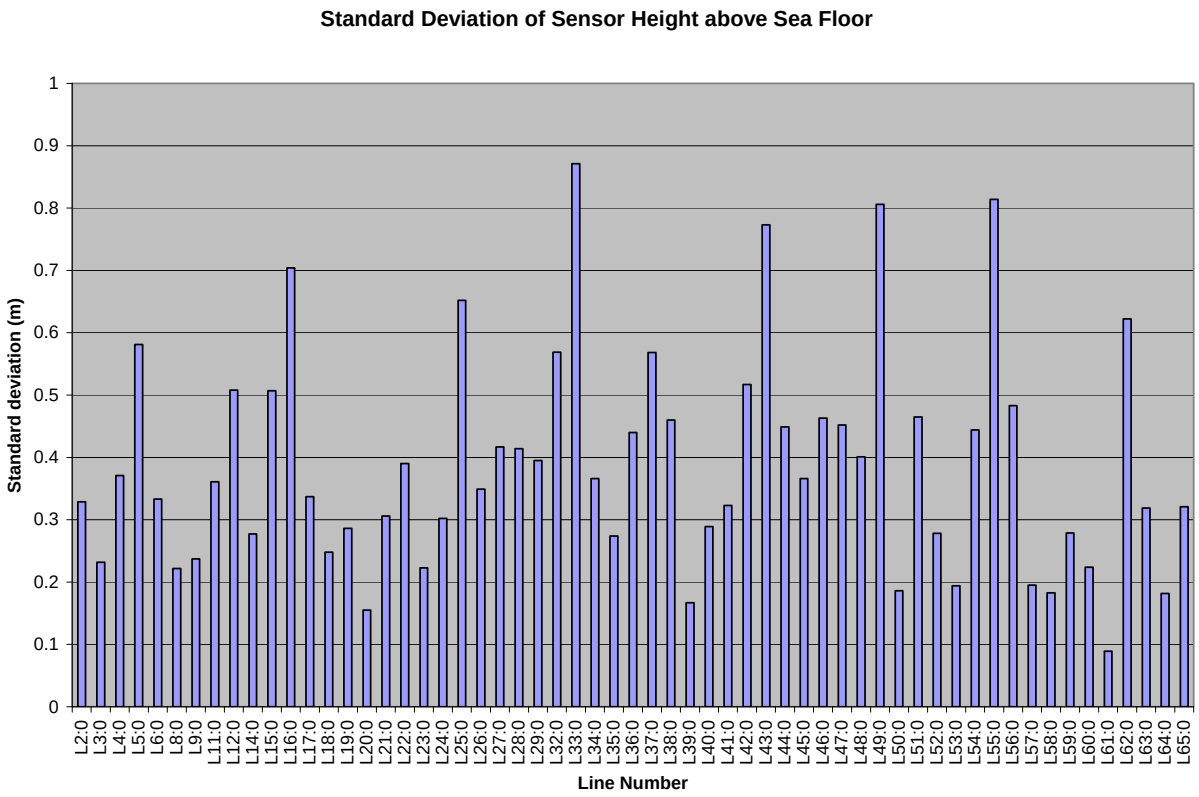

Figure 22. Standard deviation of the sensor height above the sea floor.

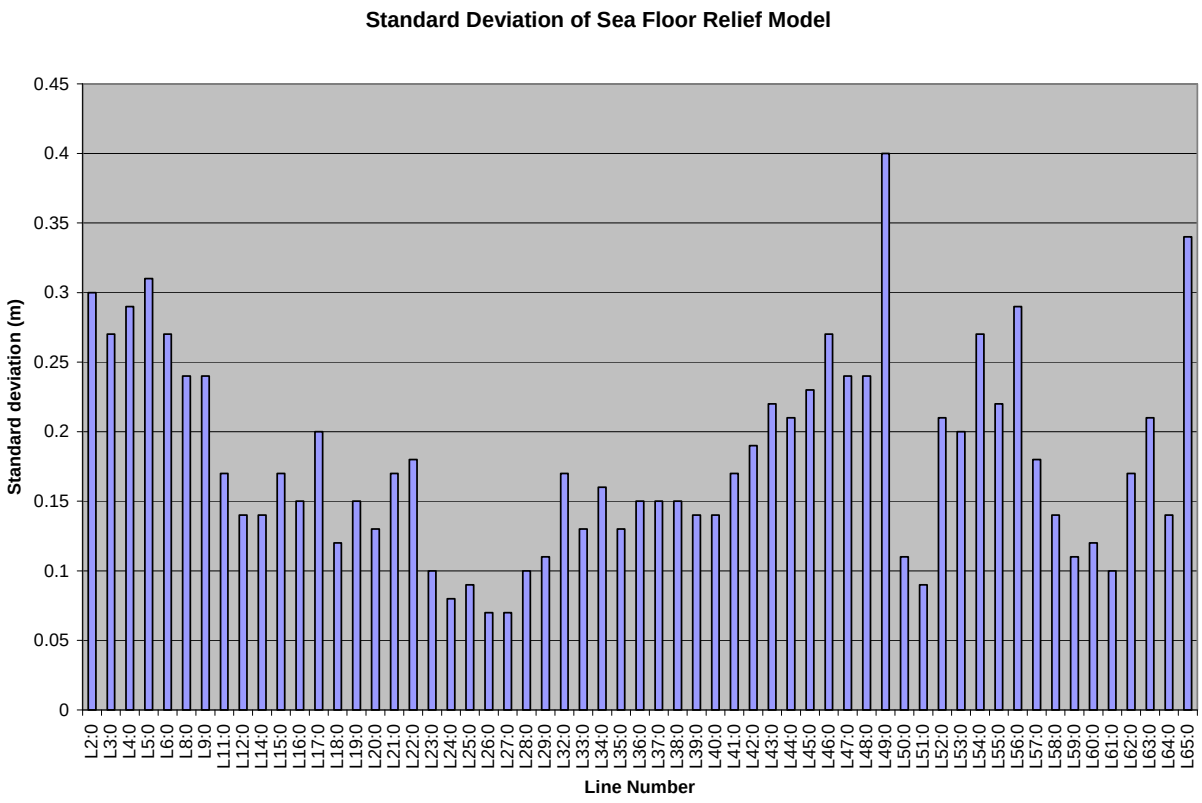

Figure 23. Standard deviation of the sea floor relief model calculated from the depth and altimeter sensors.

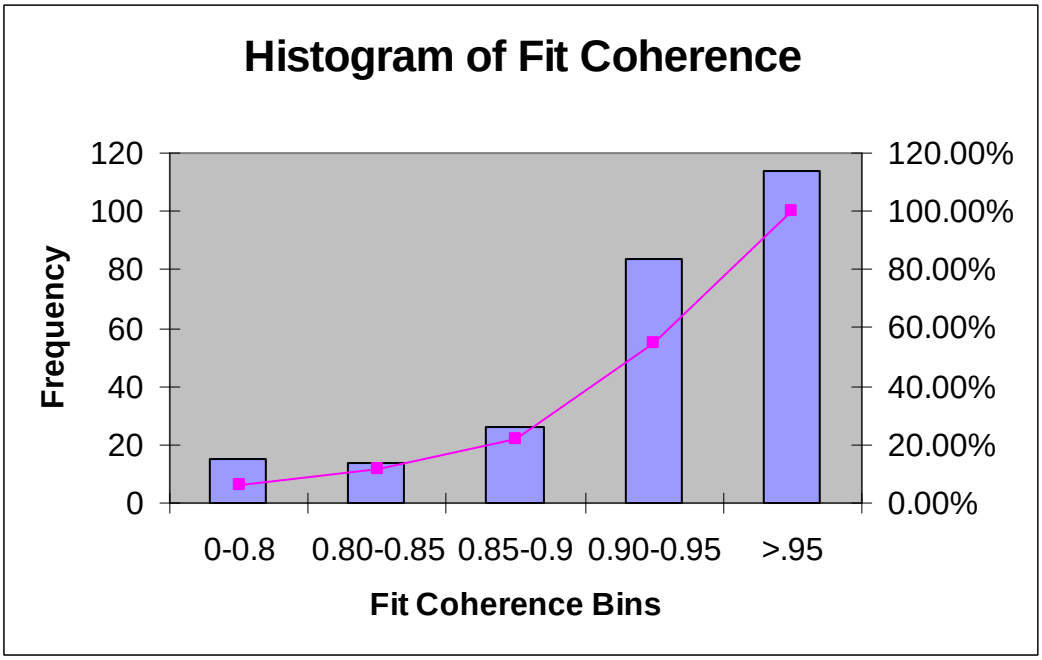

Figure 24. Histogram of the fit coherence output from the dipole inversions

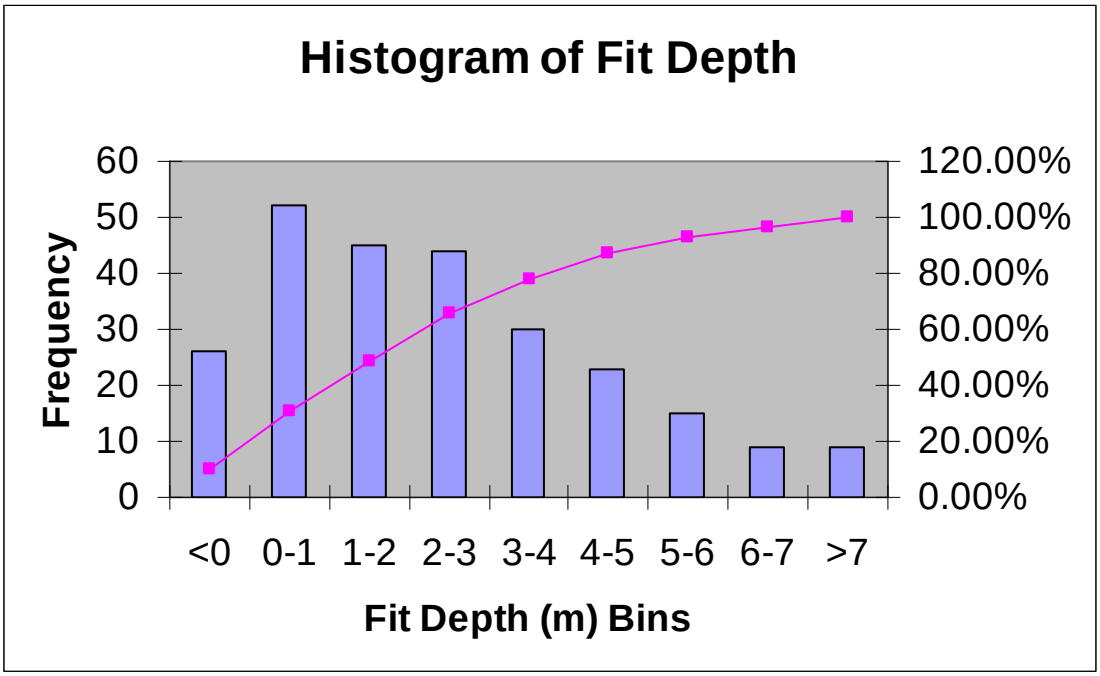

Figure 25. Histogram of fitted depth output from the dipole inversions

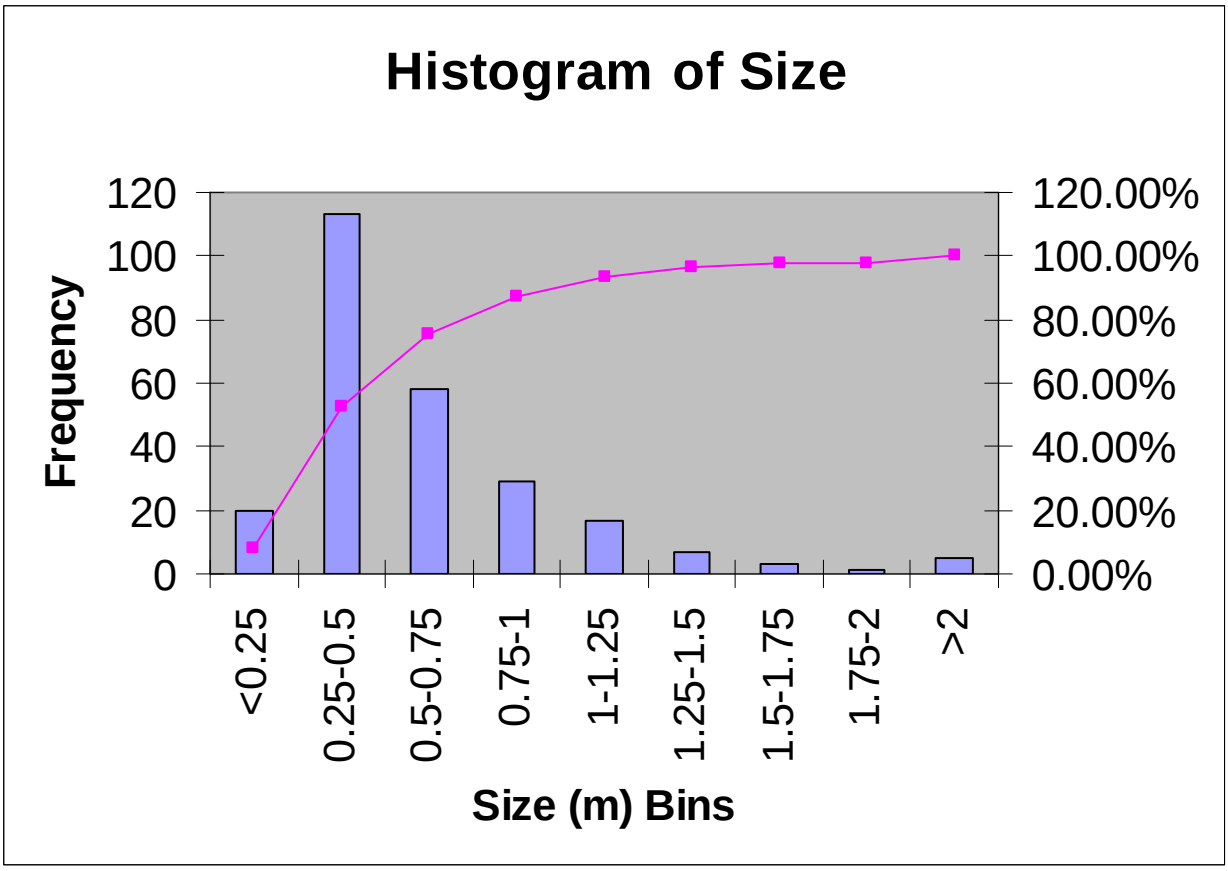

Figure 26. Histogram of the effective size output from the dipole inversions.

APPENDIX C: Analysis report MTA data sets

This section briefly summarizes the characteristics and analyses of the magnetometer data collected with the Marine Towed Array (MTA) system at the various visited sites. The MTA system is composed of a submersible sensor platform towed by a piloted vessel (see [1]-[5] for details). The towed platform array consists of eight magnetometers, equally spaced by 61 cm so as to provide a swath of over 4.5 m on a single traversal, and is automatically controlled, based on operator choice, to either (1) maintain a constant height above the bottom; or (2) maintain a constant depth below the water surface.

The magnetometer data was collected in either one of two survey modes: blanket coverage or transect. Under the blanket coverage survey mode, the entire survey area is of high interest and usually of limited size (i.e. under a hundred hectares). Complete coverage is generally achieved by navigating along tracks (long and straight, where possible) spaced 4 m apart. Under the transect survey mode, on the other hand, the objective typically is to define the area(s) of contamination within a very large area, and so much coarser coverage is sought by navigating along tracks spaced hundreds of meters apart.

Surveyed Sites

The characterized and analyzed magnetometer MTA data sets represent the first two system demonstrations in Currituck Sound and Ostrich Bay, respectively, along with three subsequent surveys in Lake Erie, Bahia Salinas del Sur and the Potomac River, respectively.

The first MTA system demonstration took place in May 2005 on Currituck Sound (adjacent to the former Naval Target Facility in Duck, NC) and entailed surveying a blanket coverage area of more than 60 hectares at depths of less than 4 meters [1]. The resulting leveled and mapped magnetometer data is shown in Figure 1.

The second demonstration took place in June 2006 on Ostrich Bay (adjacent to the former Naval Ammunition Depot in Bremerton, WA) and entailed surveying a blanket coverage area of more than 75 hectares to depths reaching 10 meters [2]. The resulting leveled and mapped magnetometer data is shown in Figure 2.

The first post-demonstration survey took place during the 2006 August/September period on Lake Erie (adjacent to the former Erie Army Depot in Ottawa County, OH) and was part of a wide area assessment effort covering a total area of over 20,000 hectares [3]. Because the goal here was to establish the extent and make up of the UXO contamination, rather than to locate and identify every single item, a number of transects (spaced 165 m apart within a predefined enclosed area) were proposed. Figure 3 shows, in yellow, all transects that were actually surveyed. Note that starting at the southern end, every other proposed transect was surveyed, eventually thinning out to every fourth transect as the northern site boundary was approached. More proposed transects (spaced

330 m apart) were extended to the north in order to better define the extent of the UXO contamination. The red dots falling on the surveyed transects represent magnetic anomalies with peaks exceeding a threshold of 7.5 nT, and are presumably good candidates for potential UXO items.

In addition to transects on the lake, a blanket coverage area of the accessible parts of the inlet leading to the Toussaint River was also surveyed. The resulting leveled and mapped magnetometer data is shown in Figure 4.

The second post-demonstration survey of the MTA system was the first to be conducted in sea water, and occurred in June 2006 in Bahia Salinas del Sur off the southeastern coast of the Puerto Rican island of Vieques [4]. Because a large portion of the bay was inaccessible to the MTA system, either due to the shallowness of the water or the fragility of the marine life (coral, sea grass, etc.), a flat bottom fiberglass skiff was also used. In this case, an array of three magnetometers was rigidly mounted inside the skiff. The magnetometers were equally spaced by 71 cm so as to provide a swath of over 2 m on each traversal, and their heads lay on the bottom of the skiff so as to provide a fixed position relative to the water surface. The resulting leveled and mapped magnetometer data collected using the MTA system and the skiff are shown, respectively, in Figure 5 and Figure 6. Note that the combined survey covered an area of more than 80 hectacres, with the MTA system covering more than 60 hectacres and the skiff covering more than 20 hectacres.

The third post-demonstration survey took place in October 2007 on the Potomac River (adjacent to the Blossom Point Research Facility in Welcome, MD). Like the Lake Erie survey, the goal here was to assess the extent and makeup of the current UXO contamination and so a number of transects were again proposed, this time spaced 125 m apart over an area of more than 3,500 hectares. Just as in Vieques, the skiff was used for portions of the site that were inaccessible to the MTA system. Figure 7 shows, in blue, all transect portions that were initially surveyed using the MTA system, and in green, all transect portions that were initially surveyed using the skiff. Based on a review of this initial transect data, a number of additional transects were proposed to provide the most useful supplementary information. These are shown in Figure 7, in black, and appear as shorter transects oriented either transversely or at an angle to the original set of transects. Most of these, in addition to a 30 hectare blanket coverage rectangular area, were subsequently surveyed. The resulting leveled and mapped blanket coverage magnetometer data is shown in Figure 8, while Figure 9 shows the magnetometer data for a close-up of the two transects that traversed the blanket coverage area.

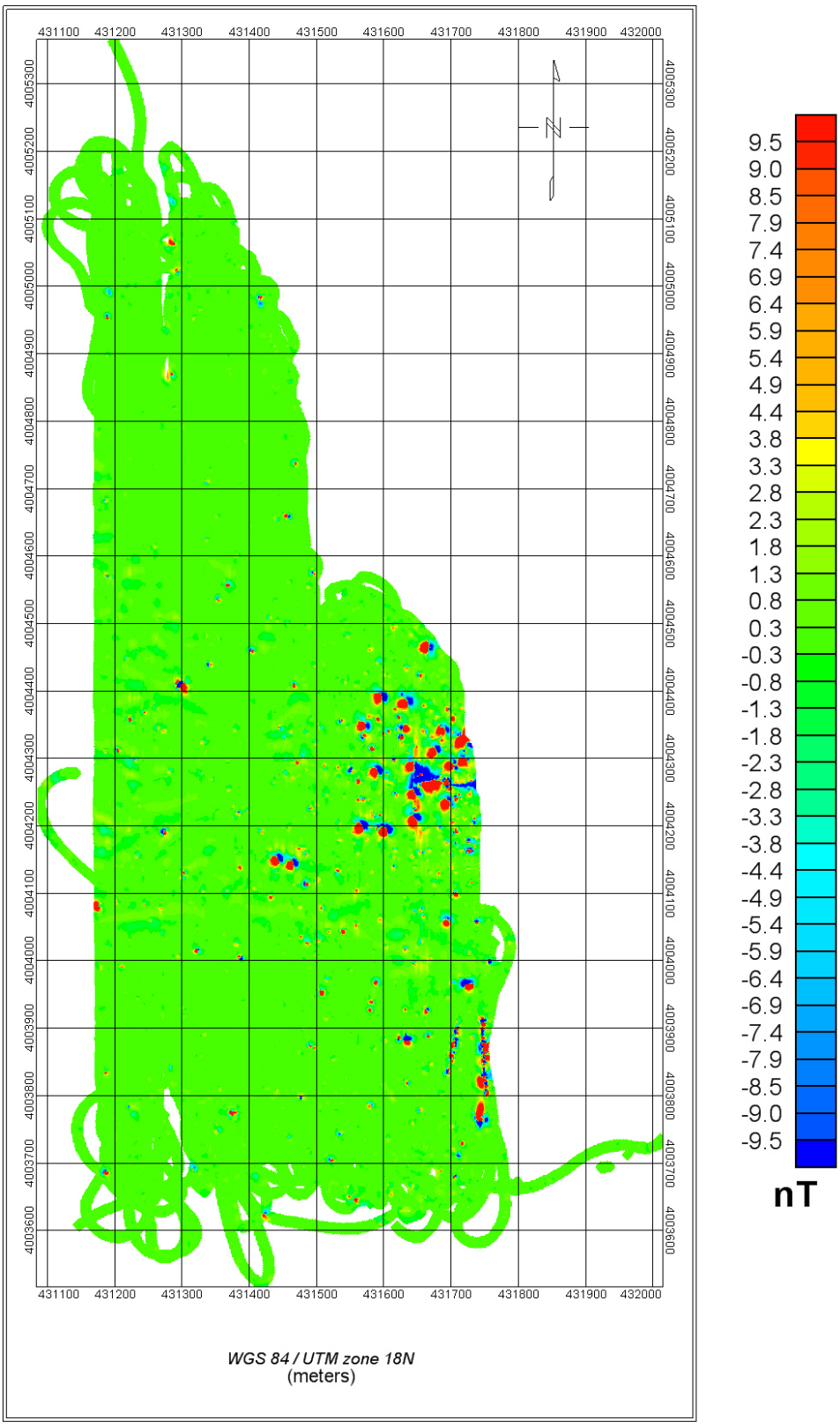

Figure 1 –MTA magnetometer data collected at the first demonstration of the system in Currituck Sound, off of Duck, NC [1].

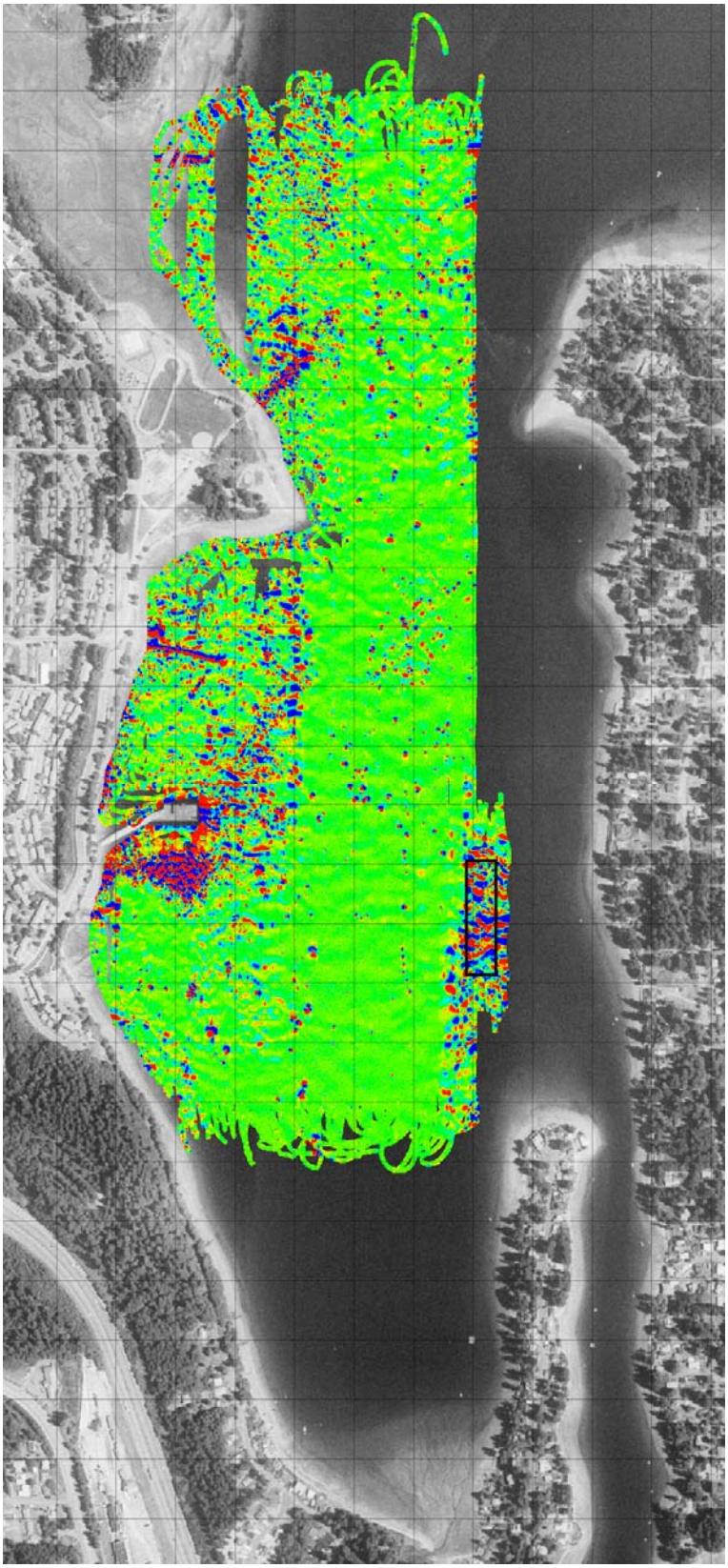

Figure 2 – The MTA magnetometer data collected on Ostrich Bay during June 2006 and presented on the same ±10 nT scale as Figure 1. The rectangular area on the southeastern end of the site was set up as a prove-out site, and coincidently represents the magnetically noisiest section of the site [2].

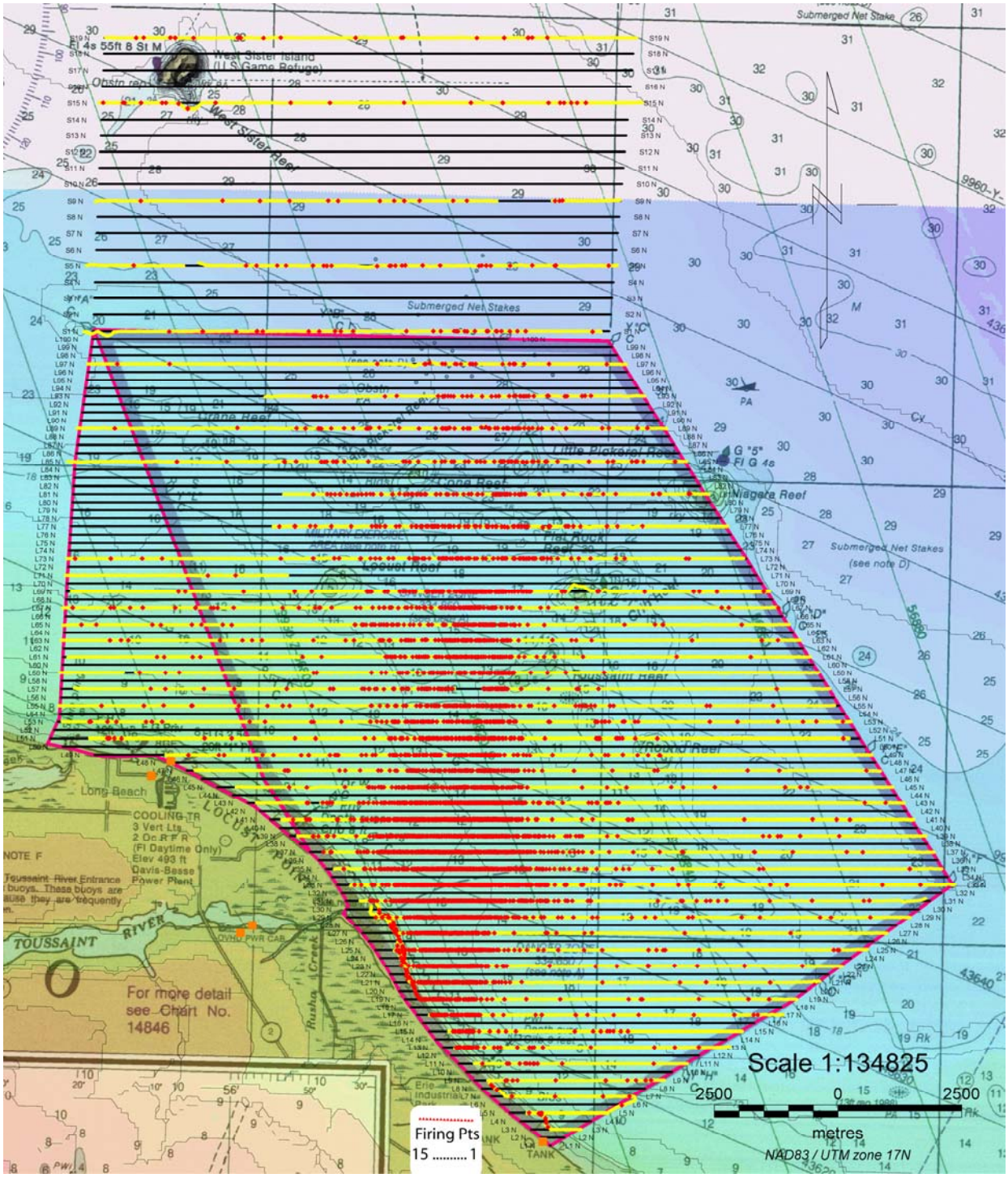

Figure 3 – Map showing all the originally planned transects on Lake Erie (black) with those transects surveyed using the MTA system (yellow) and all anomalies of peaks exceeding a threshold of 7.5 nT (red). The anomalies form a dense fan that emanates from the fifteen firing points at the bottom of the figure, and dissipates outward as a function of radial distance [3].

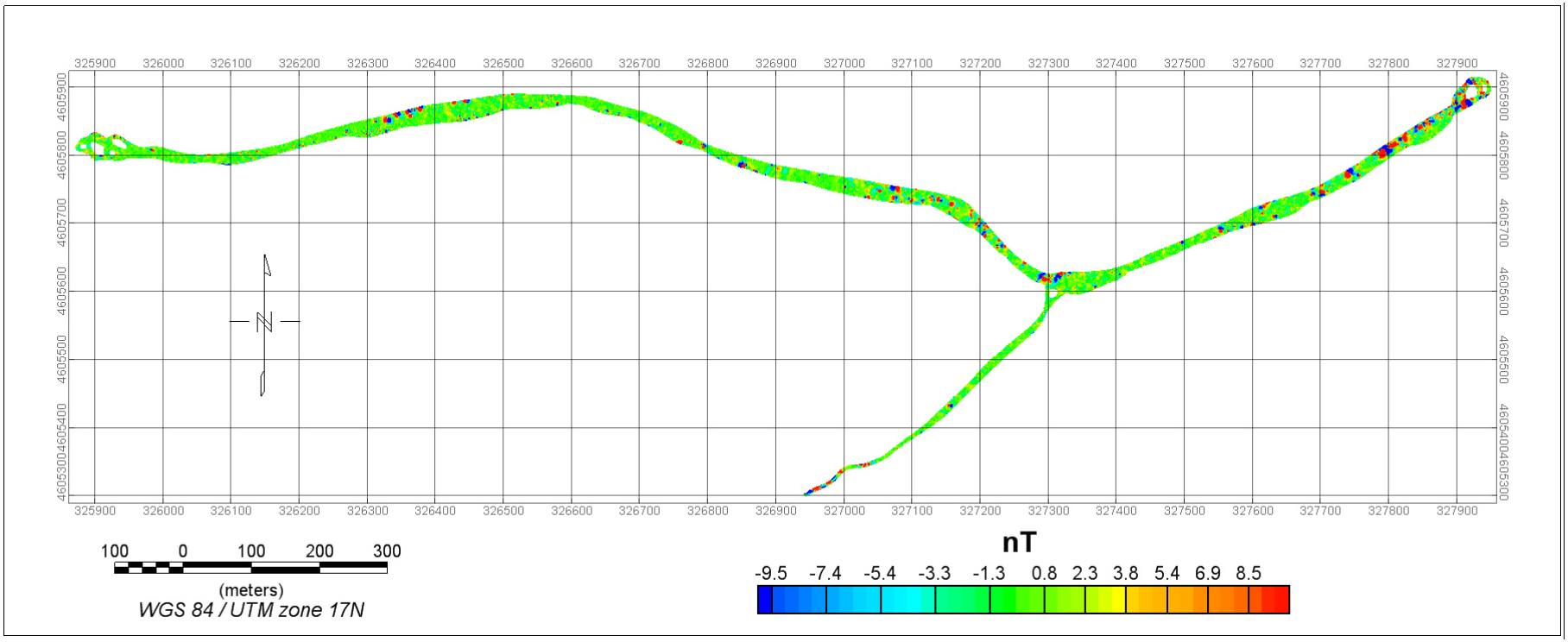

Figure 4 – MTA magnetometer data collected in the inlet leading to the Toussaint River (visible in the lower left side of Figure 3).

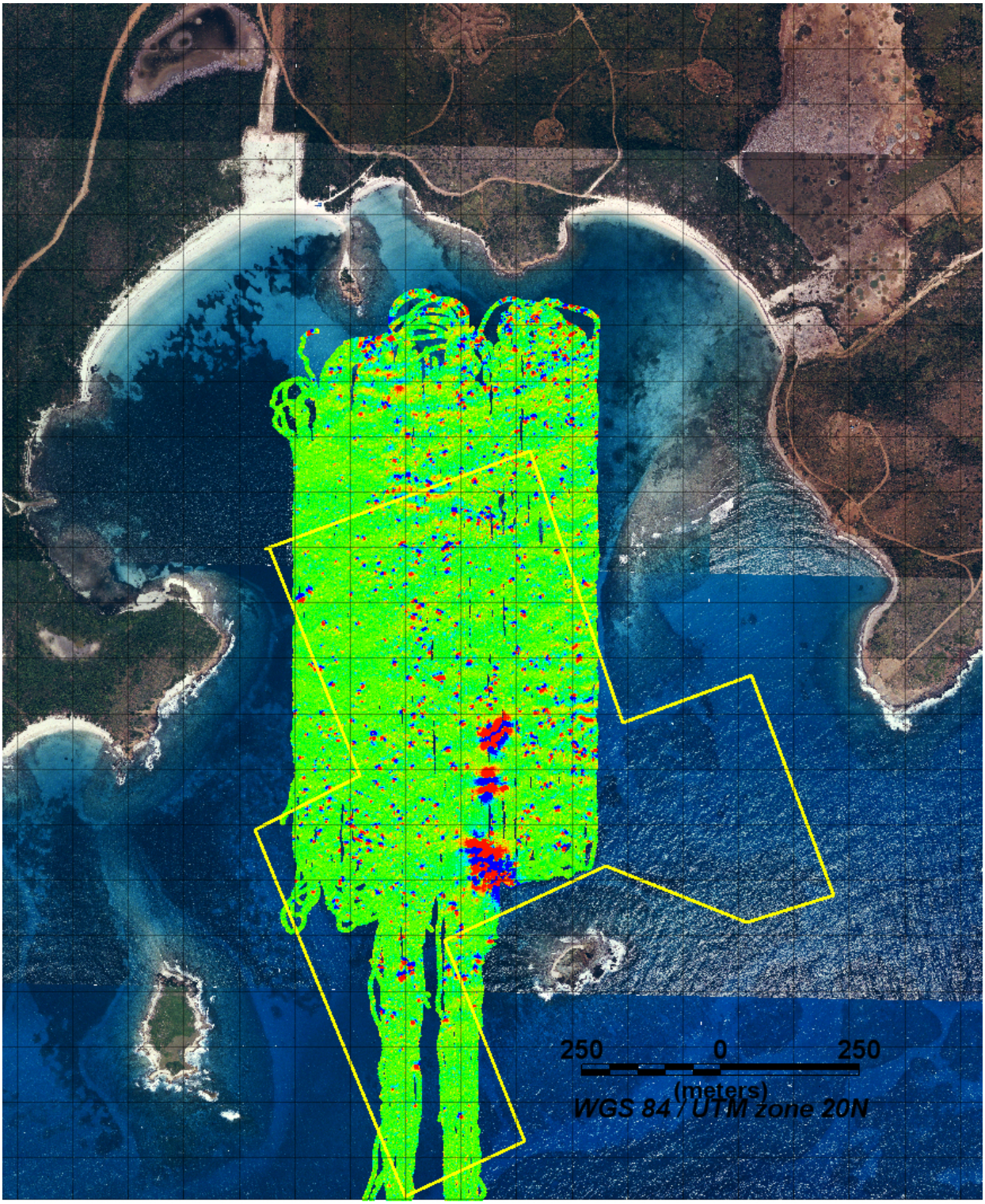

Figure 5 – The MTA magnetometer data collected in Bahia Salinas del Sur off the southeastern coast of the Puerto Rican island of Vieques. Scale is ±10 nT. The oddly-shaped yellow polygon represents the area where previous high density bathymetry data had been collected [4].

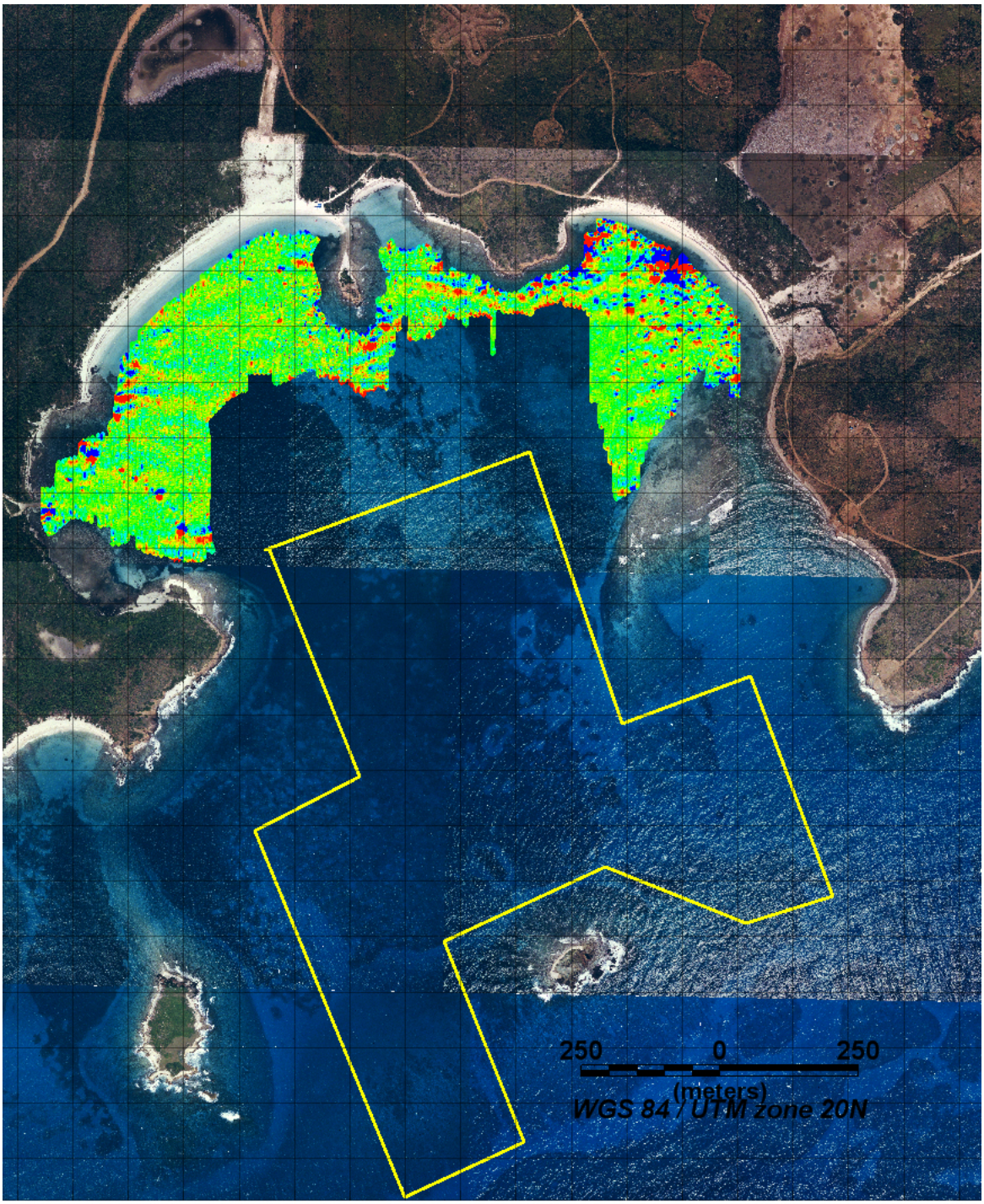

Figure 6 – Magnetometer data collected with the skiff. The skiff was deployed to survey sections of the bay that were shallow and/or inaccessible to the MTA system. Note that unlike the MTA data of Figure 5, which is presented on a ±10 nT scale, the data here is presented on a ±25 nT scale.

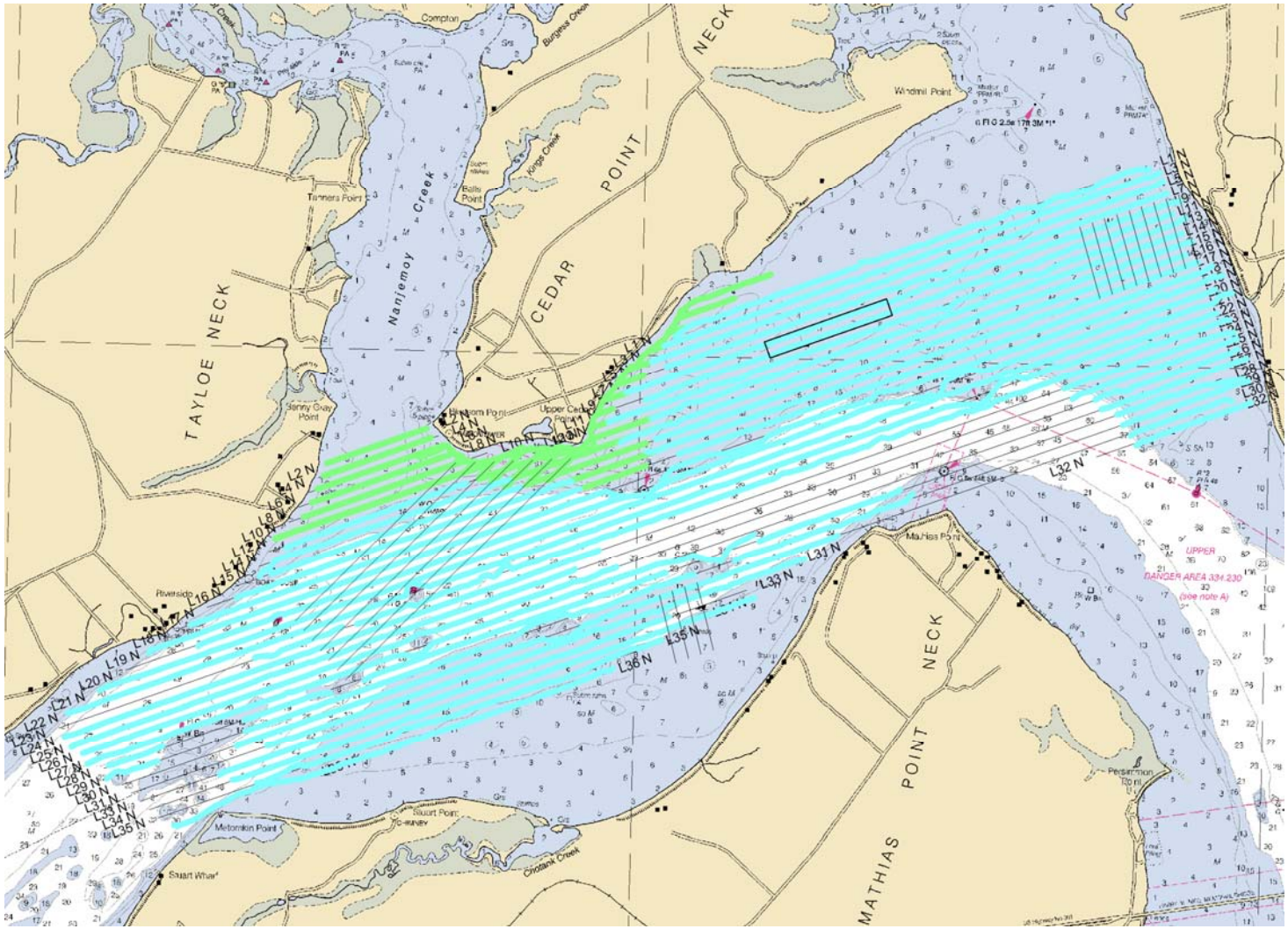

Figure 7 – Map showing transects surveyed at Blossom Point using the MTA system (blue) and the skiff system (green). The deepest and shallowest sections were generally avoided by the MTA, with the skiff used to fill in the shallow sections of particularly high interest. The shorter sets of angled lines and the rectangle were proposed as additional transects and an area to conduct blanket coverage, respectively. Most of the additional transects were surveyed, as was the blanket coverage area [5].

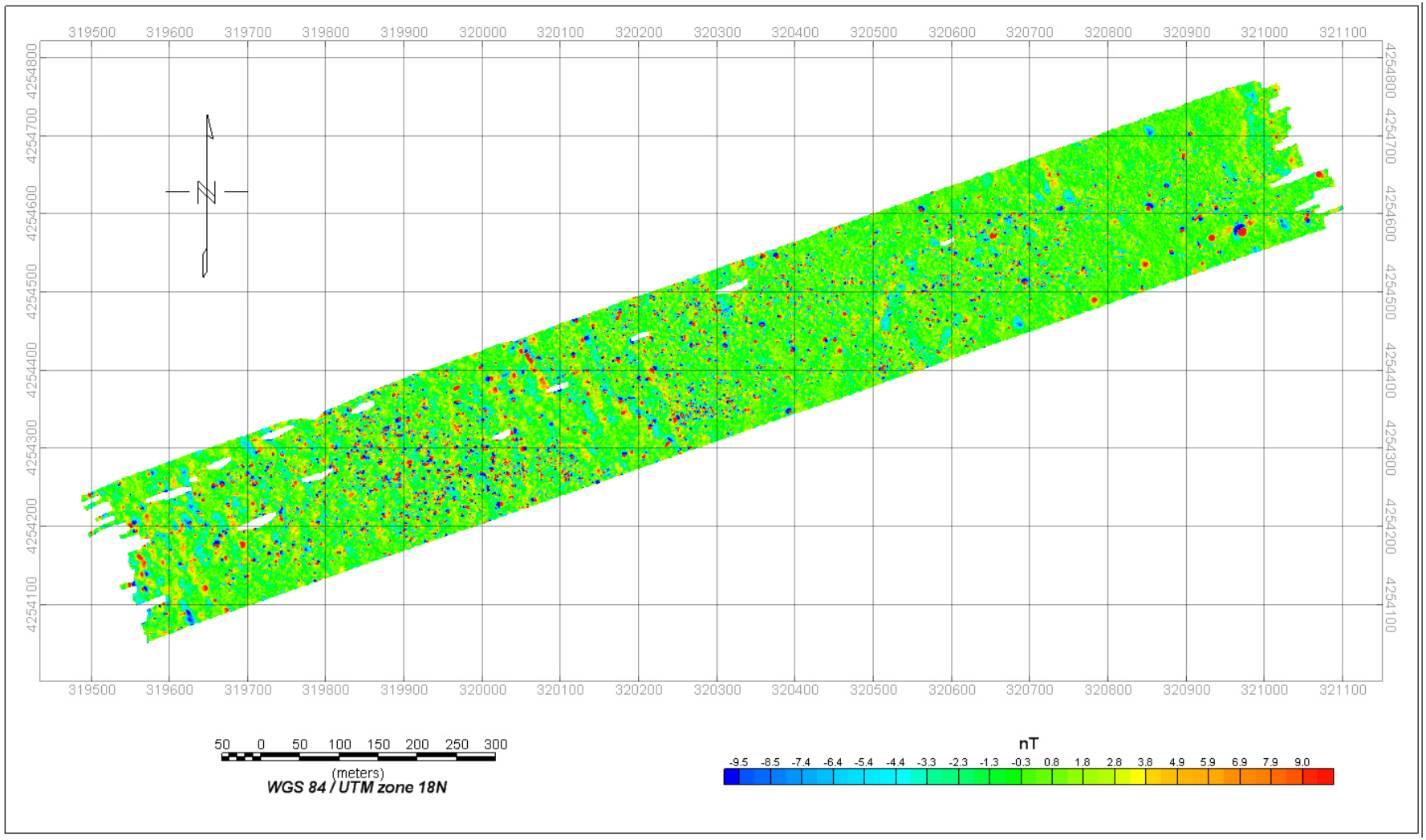

Figure 8 – The MTA magnetometer data, for the blanket coverage area shown in Figure 7, leveled and mapped to reveal numerous anomalies.

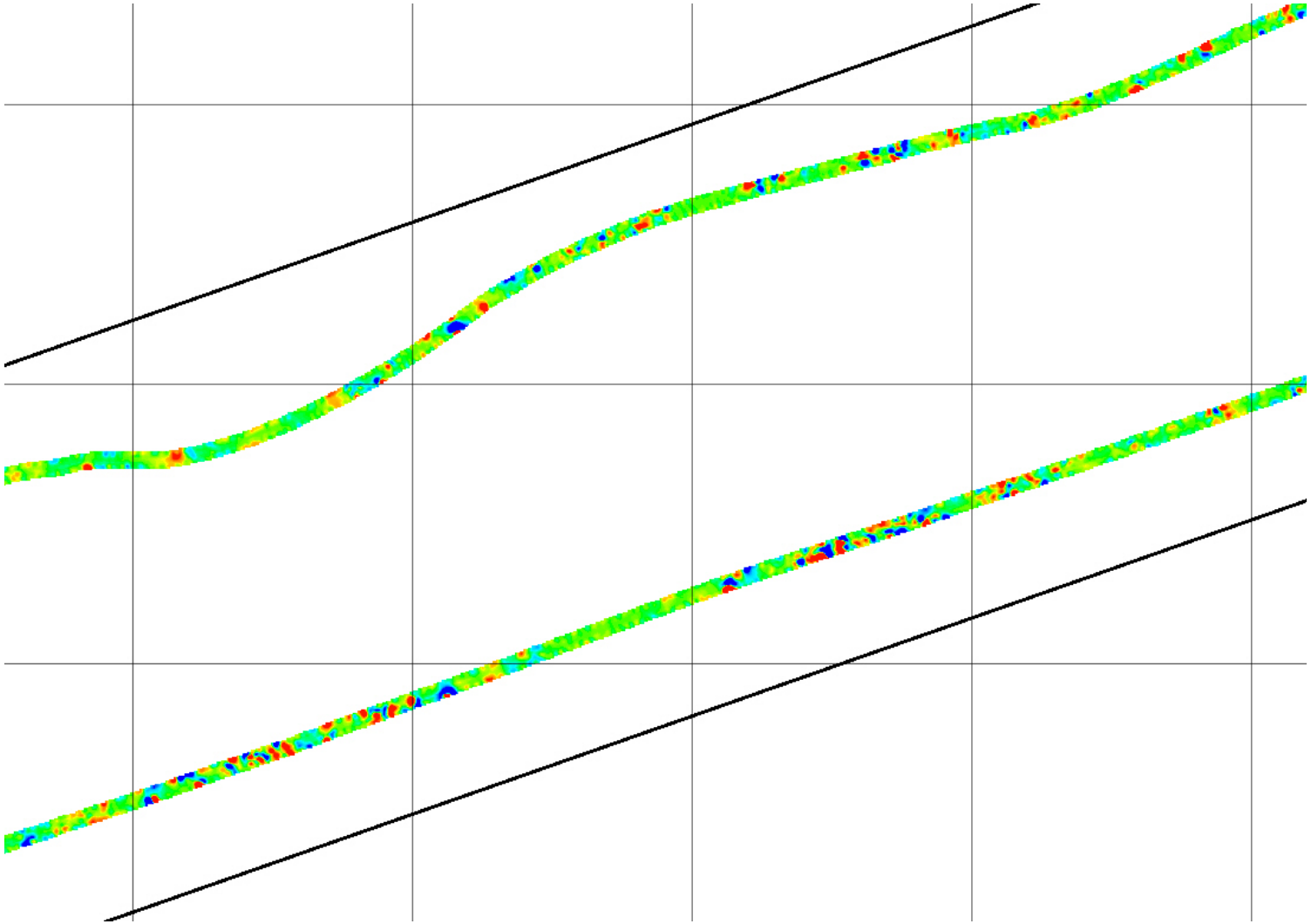

Figure 9 – A close-up showing the magnetometer data for sections of the two transects that traverse the blanket coverage area. Although the intention was to stay on the transect course, every now and then as the upper transect section reveals, the presence of obstacles (crab pot floats, steep protrusions from the bottom topology, etc.) demanded temporary deviation from the straight course.

Data Characteristics and Analyses

In order to compare the various magnetometer data sets at the aforementioned sites, the following will be examined:

1. Background noise levels;
2. Anomaly signal to noise ratio (SNR) values; and
3. Estimates of object sizes and burial depths from anomaly data.

In addition, fit coherences for the estimates and water depths at the estimated object locations will also be examined.

To begin with, however, relevant differences in survey operational details of the MTA system should be noted on a per site basis.

Height of Towed Array above Bottom

The towed platform altimeter data collected at the aforementioned sites are summarized in Figures 10–15 and further condensed into Table 1 below.

Site (in chronological order)		Height of Towed Sensor Platform above Bottom (m)		
		Median	Mean	Std Dev
Duck		1.05	1.15	0.40
Ostrich Bay		1.31	1.84	1.42
Lake Erie (Transects)		1.51	1.48	0.15
Vieques		2.03	2.55	1.42
Blossom Point	Transects	1.25	1.38	1.06
	Blanket Coverage	1.26	1.29	0.21

Table 3 – "Height above Bottom" statistics for the towed array, given in meters. The median, mean and standard deviation values over all survey legs are tabulated.

It is clear from Table 1 that the smallest sensor standoff occurred at Duck. Since this was the first demonstration of the system, an effort was made here to establish the closet practical standoff for the array. As Figure 10 shows, there were instances (e.g. legs 10–14) where the water was so shallow that no usable altimeter data was available. For those legs, the towed array had to be operated in the constant depth mode, with approximately zero depth automatically maintained. Fortunately, this had no significant effect on detection results due to the shallowness of the water.

Although standoff distances were, on the whole, not significantly greater for the second demonstration survey on Ostrich Bay, the means and standard deviations of the individual legs shown in Figure 11 reveal much greater variability. The high variability in the height of the towed platform above the bottom is explained by the site conditions, where remnants of old pier structures and other debris scattered throughout large portions of the survey site forced the repeated raising and lowering of the platform based on careful monitoring of the altimeter data from the leading tow vessel.

For similar reasons based on site conditions, the Lake Erie transects survey reveals relatively low standoff variability, as shown in Figure 12, while the survey at Vieques reveals rather high standoff variability, as shown in Figure 13. At Lake Erie, where a slowly varying topography of the bottom existed and where the surveyed transects were generally long with few obstructions, the platform was able to maintain a height above bottom of ~1.5 m (sometimes even ~1.25 m) with very little variation. In contrast, at Vieques, where many items, both natural and man-made, protrude from the sea floor and where a blanket coverage survey was conducted, the platform had to not only maintain a greater height above bottom of ~2 m, but also be raised and lowered a number of times creating the observed variability shown in Figure 13.

Finally, the array height above bottom statistics for Blossom Point are shown in Figures 14 and 15 for the transect surveys and the blanket coverage survey, respectively. Although a consistent height above bottom of ~1.25 m was maintained throughout, the high variability during some transects was due to the fast varying topography of the bottom along those transects. Note that the relatively small variability during the blanket coverage survey was maintained by circumnavigating the few obstacles that existed on the bottom within the defined blanket coverage area.

In summary, it is clear that under good conditions (i.e. where the bottom is relatively smooth and where very few obstructions exist) the platform can capably maintain a standoff distance of 1.25 m ± 0.25 m from the bottom. Beyond that, the platform standoff distance and variability will depend heavily on the particular characteristics of the bottom topology.

Background Noise Levels

The process of estimating magnetometer background noise levels is, to a certain extent, a subjective one. This is because it is not always clear where the background ends and the signal begins. This is most evident in environments where there exists either significant magnetic variability due to geology, or pockets of high concentrations of signal (see Figure 2 for examples of both).

In order to remove some of the subjectivity, the background noise levels are estimated via two independent methods, whereupon the results are verified to be consistent. The first method estimates noise levels directly from the magnetometer time series data. Note that a time series data set is associated with every survey leg conducted at a particular site. The second method derives noise estimates from the mapped anomaly data used in the target characterization stage. These data are manually extracted from the processed magnetometer data site map by an operator boxing each viable anomaly using a polygon.

<u>Noise Estimates from Time Series Data</u>

The collection of MTA data at a site is carried out by following a set of pre-planned tracks over the entire site. Each uninterrupted survey conducted over a section of track(s)

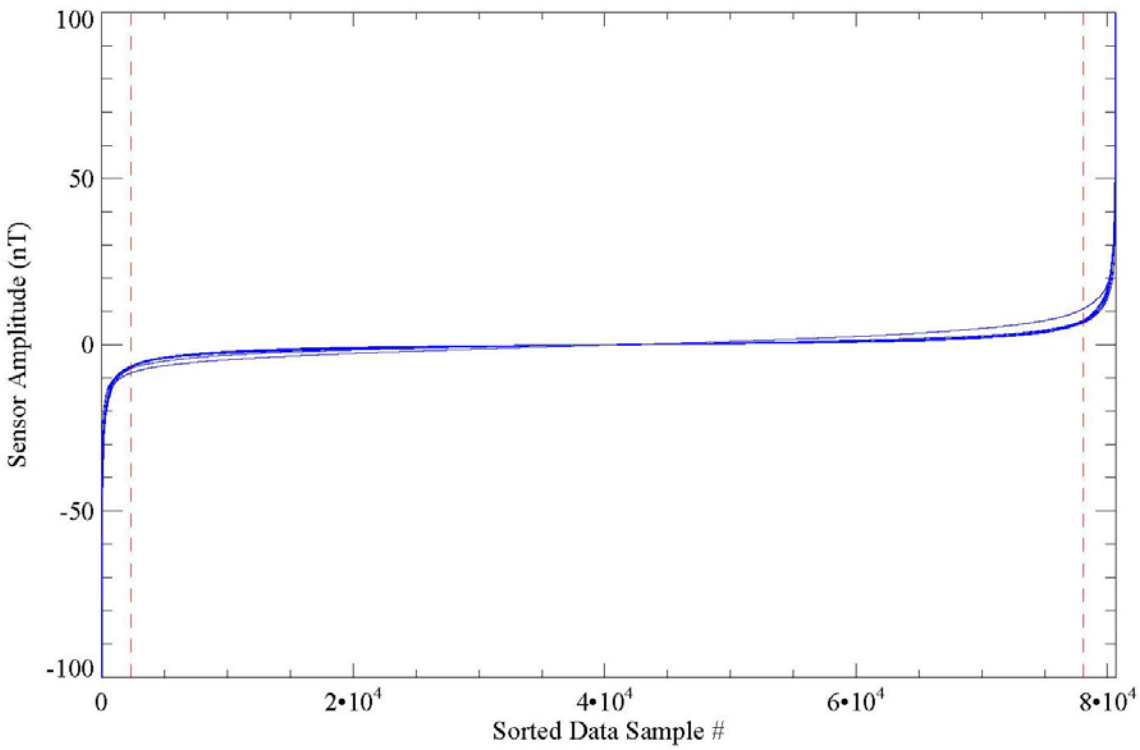

Figure 16 – One of the thirteen time series data sets collected in the blanket coverage area at Blossom Point. The multiple blue curves represent the data for each of the eight sensors, sorted by ascending amplitude. The data between the red dashed lines are attributed to the background, and represent 93.9% of the time series data shown above. It is this data that is used in the noise level computation.

defines a separate time series of data. This method examines the magnetometer data from each time series and, in an automated fashion, determines a corresponding background noise level. The method relies on isolating those data points attributed to the background and using these to compute the noise, N, defined as $N = \sigma\{\text{background data}\}$, where $\sigma\{\text{background data}\}$ denotes the standard deviation of the background data. The process by which the time series background data is isolated is outlined below and supported by Figure 16:

1. Sort the leveled time series data by ascending amplitude for each sensor;
2. Neglecting the first and last 10% of the data points, determine an average gradient for the intermediate 80% of the data for each sensor;
3. For each sensor, determine the lower and upper data sample numbers where the gradient starts to diverge significantly from the average gradients computed in step 2;
4. The red dashed lines represent, at the lower end, the maximum of the lower limits over all sensors, and at the upper end, the minimum of the upper limits over all sensors;
5. All sorted data points between the dashed red lines of Figure 16 are attributed to the background (and conversely, those high negative and positive amplitudes at either end are attributed to signal).

Site	% Data Used	Sensor Noise, *N* (nT) – mean & [*min,max*] values								
		1	**2**	**3**	**4**	**5**	**6**	**7**	**8**	**Overall**
Duck	96.4	0.41 [*0.12,1.36*]	0.46 [*0.17,1.47*]	0.40 [*0.10,1.45*]	0.42 [*0.12,1.43*]	0.44 [*0.13,1.45*]	0.43 [*0.11,1.49*]	0.43 [*0.12,1.49*]	0.46 [*0.12,1.56*]	0.43
Ostrich Bay	90.6	3.50 [*1.08,6.31*]	3.12 [*0.63,6.80*]	2.76 [*0.57,6.41*]	2.66 [*0.39,6.21*]	2.61 [*0.41,6.00*]	2.59 [*0.45,6.04*]	2.69 [*0.51,6.13*]	3.23 [*0.68,6.29*]	2.90
Lake Erie (Transects)	95.8	2.04 [*1.06,2.96*]	1.45 [*0.80,2.14*]	0.91 [*0.37,1.70*]	0.79 [*0.18,1.65*]	0.76 [*0.15,1.61*]	0.81 [*0.19,1.62*]	1.10 [*0.45,1.82*]	2.09 [*0.73,7.72*]	1.24
Vieques	91.3	2.86 [*2.21,3.36*]	1.82 [*1.12,2.29*]	1.58 [*0.82,2.11*]	1.57 [*0.77,2.03*]	1.58 [*0.78,2.09*]	1.58 [*0.78,2.18*]	1.77 [*1.04,2.45*]	3.00 [*2.01,3.97*]	1.97
Blossom Point (Transects)	94.7	1.95 [*0.87,2.57*]	1.23 [*0.62,1.84*]	0.66 [*0.31,1.30*]	0.53 [*0.17,1.22*]	0.59 [*0.16,1.20*]	0.71 [*0.21,1.28*]	1.20 [*0.62,1.63*]	2.32 [*1.78,3.23*]	1.15
Blossom Point	92.9	2.61 [*2.21,3.07*]	2.16 [*1.78,2.51*]	1.89 [*1.61,2.12*]	1.86 [*1.63,2.13*]	1.89 [*1.66,2.14*]	1.99 [*1.72,2.30*]	2.25 [*1.96,2.73*]	3.71 [*2.92,5.22*]	2.29

Table 2 – Sensor noise estimates obtained from the MTA time series data, given in nano-Teslas. The data were collected via the blanket coverage survey mode, unless otherwise noted. The mean levels over all survey legs conducted at a particular site are tabulated on a per sensor basis, along with the minimum and maximum values (respectively, in square brackets). Also included for each site are the overall mean noise levels, averaged over all sensors, and the total percentage of data attributed to the background.

The results of computing the background noise levels from each time series at all the visited sites are summarized in Figures 17-22 and further condensed in Table 2. The noise levels are organized by sensor numbers, with each blue diamond symbol in Figures 17-22 corresponding to a separate time series. The red vertical lines connect the minimum and maximum values for each sensor, with the mean noise levels denoted by the cross symbols. The mean, minimum and maximum values for each sensor at each visited site are presented in Table 2. Just as in Table 1, the sites are organized in chronological order. The overall noise levels are also computed for each site by averaging over all sensors, and these are likewise presented in Table 2.

Upon examining the overall noise levels in Table 2, it is immediately evident that the noise level at the first demonstration at Duck was considerably lower than those at all subsequent survey sites. In fact, the next lowest noise levels occurred during the transect surveys at Lake Erie and Blossom Point, at nearly three times the level encountered at Duck. Restricting consideration to the blanket coverage surveys, the overall noise levels of Table 2 are well supported by the magnetometer data maps shown in earlier figures. For example, the Duck and Ostrich Bay magnetometer data maps of Figures 1 and 2, respectively, provide evidence of the lowest and highest noise levels, respectively, with the Vieques and Blossom Point data maps of Figures 5 and 8, respectively, falling somewhere in between. At the same time that the Blossom Point noise level was determined to be slightly higher than the Vieques noise level, it should be noted that the standoff distance of the platform from the bottom was noticeably larger (and contained greater variability) at Vieques than at Blossom Point, as supported by the values given in Table 1.

The lower noise levels that were encountered at Duck are directly attributed to the superior magnetic field isolating capability of the original pair of actuators which were in use at Duck, but not at any of the subsequent sites. In fact, it was the failure of the tow platform actuators that prompted their replacement. And since the original actuators were no longer being manufactured, inferior alternatives had to be used. Examining the mean noise levels of Table 2 and Figures 17-22 on a per sensor basis, it is clear that apart from the Duck data, the outlying sensors closest to the actuators (i.e. sensors 1 & 8) have consistently higher mean noise levels than the inner sensors furthest from the actuators (i.e. sensors 4 & 5).

Noise Estimates from Extracted Anomaly Data

The information needed to locate and identify potential UXO items is obtained by analyzing spatially coherent anomaly data extracted from the processed (i.e. leveled and mapped) MTA magnetometer data. An example of such an extracted data set is shown below in Figure 23. Since for best results, the extracted spatial magnetometer data needs to include the item-related signals all the way down to the surrounding background level, these data provide a readily available alternative means for determining the background noise levels. In this case, this is accomplished by attributing to the background those data within a narrow region of the boundary – the data points highlighted in green in Figure 23

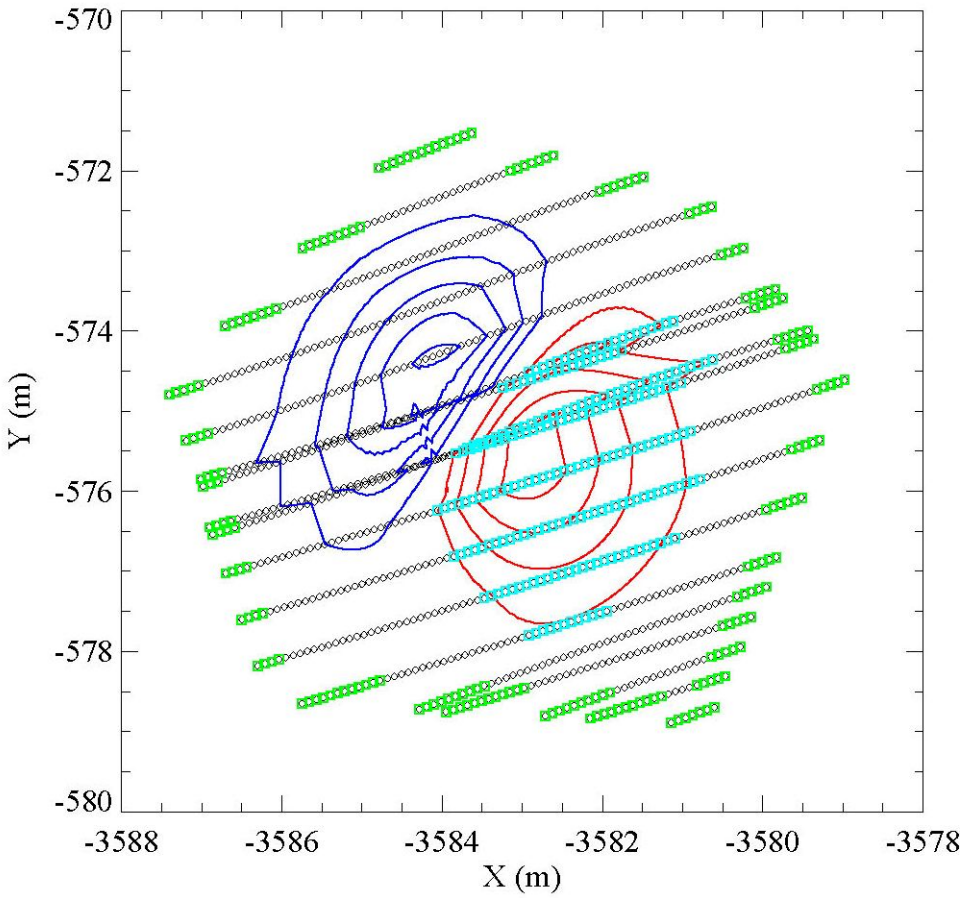

Figure 23 – An example of extracted mapped anomaly data from the Blossom Point blanket coverage area. The red and blue contour lines represent, respectively, the positive and negative item-related signals in levels of 5 nT. The data highlighted in green are attributed to the background and used in the noise level computation. The data highlighted in cyan are attributed to the (positive) signal and used in the signal calculation for SNR determination.

– and calculating a noise estimate from this data by using $N = \sigma\{\text{background data}\}$, as before.

The background noise levels determined from all the analyzed anomalies at each of the aforementioned sites are summarized in the right panels of Figures 24–28 and further condensed in Table 3 below.

Site	**# of Anomalies**	**Noise, N (nT)**	
		Median	**Mean**
Duck	432	0.56	1.33
Ostrich Bay	648	3.81	14.15
Lake Erie	779	2.86	4.51
Vieques	532	3.11	11.73
Blossom Point	619	1.48	1.91

Table 3 – Noise estimates obtained from extracted mapped anomaly data, given in nano-Teslas. The median and mean noise levels over all the anomalies are tabulated for each site.

The median values computed from the anomaly data provide good overall estimates of the background noise levels at the various sites. The mean values are indicators of the level of variability due to geology and other larger spatial scale magnetic sources across each site.

Consistent with conclusions reached using the noise level estimates obtained from time series data, it is clear from Table 3 that (1) the noise levels at Duck were considerably lower than those at all subsequent survey sites; and (2) the noise levels at Ostrich Bay were the highest of all sites. In addition, the large mean values at Ostrich Bay and Vieques are a direct consequence of the pervasive magnetic variability that exists on larger spatial scales at these sites. This is evident upon examining the mapped magnetometer data shown in Figure 2 and Figure 5 for Ostrich Bay and Vieques, respectively, where large geologic structure exists at both sites – though to a greater extent at Ostrich Bay – with additional structure stemming from pier remnants at Ostrich Bay and sunken vessels at Vieques.

Also consistent with earlier conclusions, are the estimates for Blossom Point. This is clear by referring to the right panel of Figure 28 and noting that the first 84 of the 619 anomalies were extracted from the blanket coverage area and have generally above average noise levels, while the remaining anomalies were extracted from the transect data and have generally below average noise levels – values consistent with those tabulated in Table 2.

Not so clearly reconcilable, however, are the estimates for both Vieques and Lake Eire. It should be noted that for Vieques, the noise estimates derived from the time series data were influenced by the geologic and high concentration areas to a lesser degree than the estimates derived from the extracted anomaly data. This is supported by the fact that a reasonable portion of the time series data at Vieques was collected at large platform standoff distances, as shown by Figure 13, resulting in overall lower estimates than those obtained using the anomaly data. For Lake Erie, on the other hand, the higher noise estimates derived from the extracted anomaly data stemmed from either: (1) cases of high concentration areas where neighboring signal bled into the extracted anomaly data; or (2) cases of incomplete anomaly coverage areas where signal from the anomaly was inevitably attributed to the background.

SNR Values

The SNR definition that is adhered to here is one that is used by the UXO community through the freely available UX-Process Software [6-7]. This definition expects data in the form of extracted mapped anomalies, an example of which was previously given in Figure 23. For the specific case shown in Figure 23, the data attributed to the signal are highlighted in cyan. The signal points were identified as all those non-green data points whose amplitude were above the background level, a quantity defined as

$$\text{background} = \text{Mean}\{\text{background data}\} + 3N$$

where Mean{background data} represents the mean of all background data (i.e. green) points and $N = \sigma\{\text{background data}\}$, as before.

With the signal points identified and a noise level estimate determined for each extracted anomaly data set, the SNR values were computed (in dB) using

$$\text{SNR} = 10\log_{10}\left(\frac{\sum_{i=1}^{n}\left(S_i - \text{background}\right)^2}{\sum_{i=1}^{n} N^2}\right).$$

Here S_i represents the amplitude of the *i*-th data point, and both summations are taken over all *n* data points attributed to the signal.

The left panels in Figures 24–28 show SNR histograms over all anomalies for each site. As expected, the highest overall SNR values were obtained at Duck, where the overall background noise levels were found to be smallest. The SNR distributions for all other sites peaked about 5 dB lower than that of Duck, with the flatter Blossom Point histogram stretching way out beyond the 40 dB mark.

Target Parameter Estimates

In order to locate and identify the targets that give rise to the magnetic anomalies, each extracted anomaly data set is fed to a parameter estimation procedure. This uses a nonlinear least squares algorithm, with a dipole model for the target, to determine location and effective size estimates for each target [8-9]. Histograms of the size and burial depth estimates, for all extracted anomalies, are presented in Figures 29-33 for each of the visited sites. Also included in the figures, are histograms of the fit coherences, as well as water depths at the estimated target locations.

Some observations worthy of mentioning, upon examination of Figures 29-33, are that:

- The most reliable estimates occurred for the Duck data, where most of the fit results had coherences of 0.9 and higher. For the remaining sites, most fit results had coherences of 0.8 and higher. This corresponds well with the earlier noted fact that the SNR values at Duck were by far the highest over all sites.

- Most of the targets, over all the sites, appear to be buried in the top 1m of the bottom sediment. Also, the negative depths represent targets protruding from, or laying on top of, the bottom surface.

- At all sites but Vieques, the estimated sizes mostly cluster between 0.05 and 0.25 m, with the upper limit extending beyond 0.4 m at Ostrich Bay. At Vieques, however, sizes mostly cluster between 0.1 and 0. 5 m, an observation supported by the earlier

noted fact that the standoff distances above the bottom were by far the largest (on average) at Vieques over all other sites.

- The water depths varied widely over the visited sites, but generally did not exceed depths of 10 m or go below depths of 1 m. The clear exception is at Blossom Point, where the skiff was used and water depths shallower than 1 m were capably surveyed.

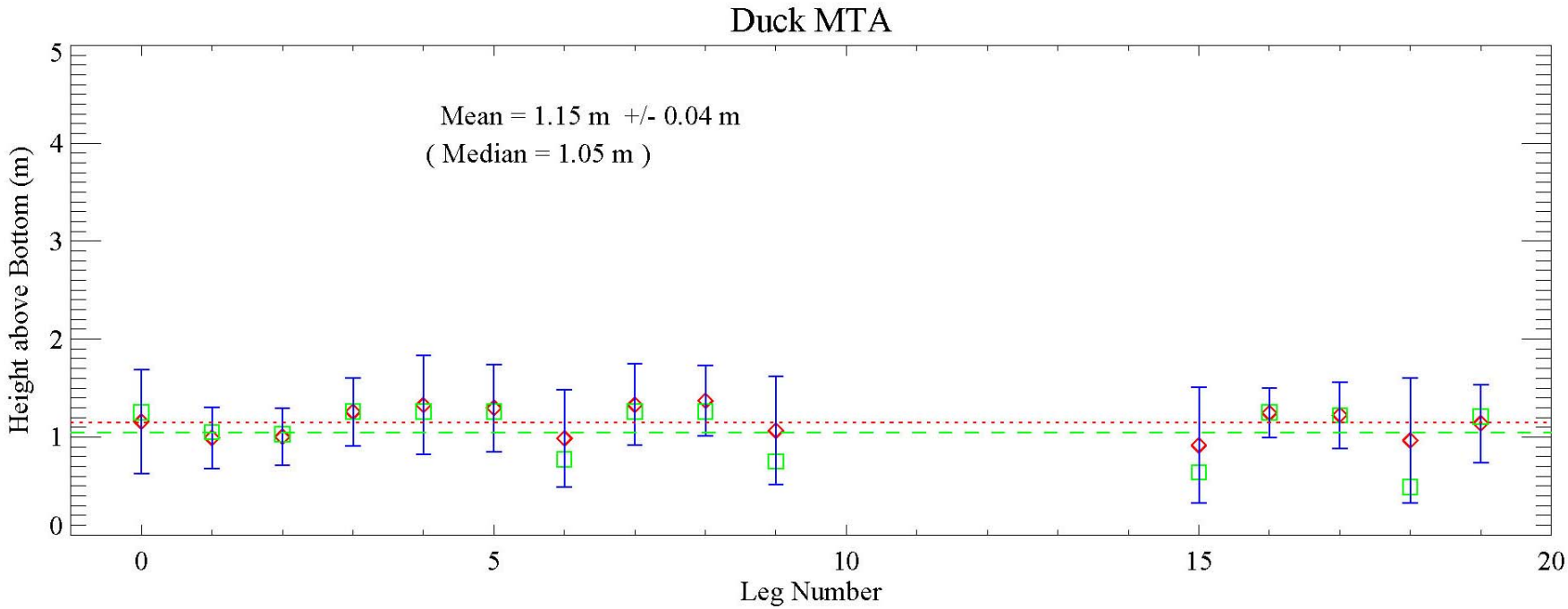

Figure 10 – Plot of the height statistics of the sensor array above the bottom for each leg of survey data. Each leg or separate time series of data is represented by it's mean (red diamond), median (green square) and standard deviation (blue bars) about the mean. The red dotted line signifies the mean of the means, while the green dashed lines signifies the median of the medians. In addition, the values of both these levels, along with the standard deviation of the means, are presented for completeness.

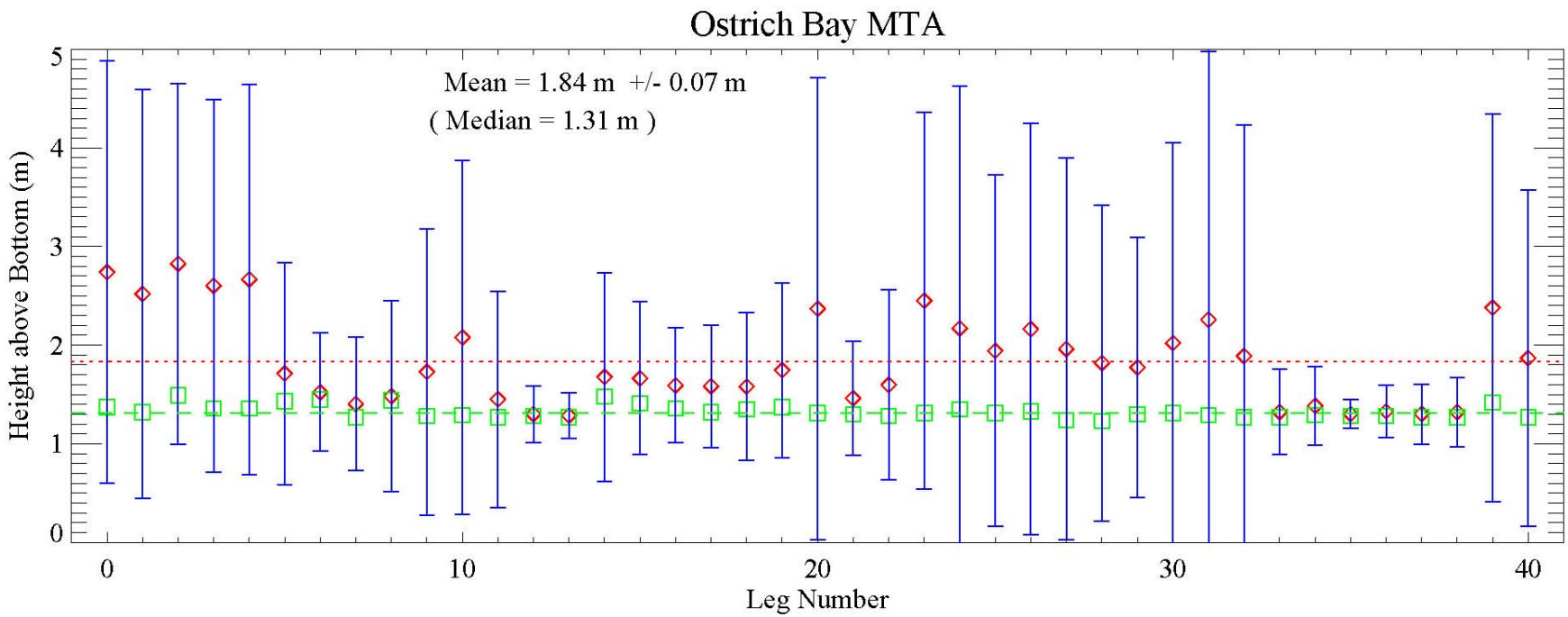

Figure 11 – Plot of the height statistics of the sensor array above the bottom for each leg of survey data. Each leg or separate time series of data is represented by it's mean (red diamond), median (green square) and standard deviation (blue bars) about the mean. The red dotted line signifies the mean of the means, while the green dashed lines signifies the median of the medians. In addition, the values of both these levels, along with the standard deviation of the means, are presented for completeness.

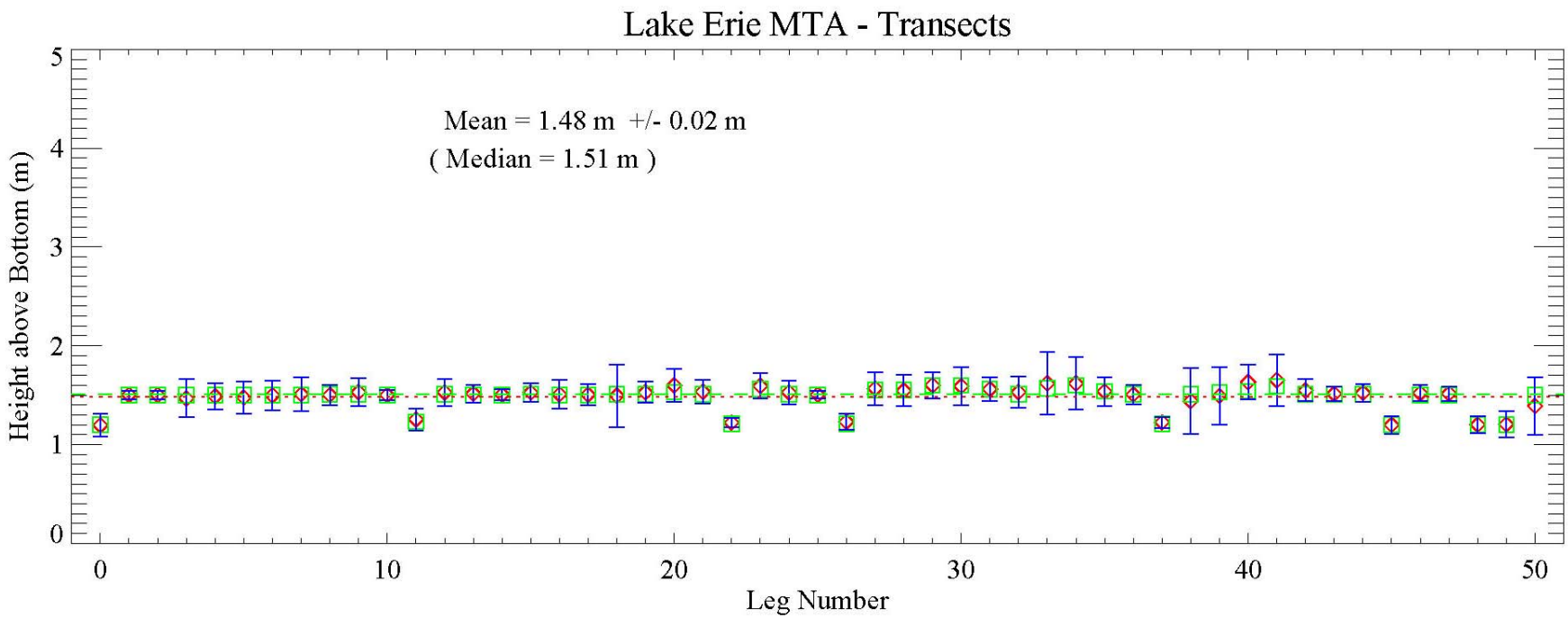

Figure 12 – Plot of the height statistics of the sensor array above the bottom for each leg of survey data. Each leg or separate time series of data is represented by it's mean (red diamond), median (green square) and standard deviation (blue bars) about the mean. The red dotted line signifies the mean of the means, while the green dashed lines signifies the median of the medians. In addition, the values of both these levels, along with the standard deviation of the means, are presented for completeness.

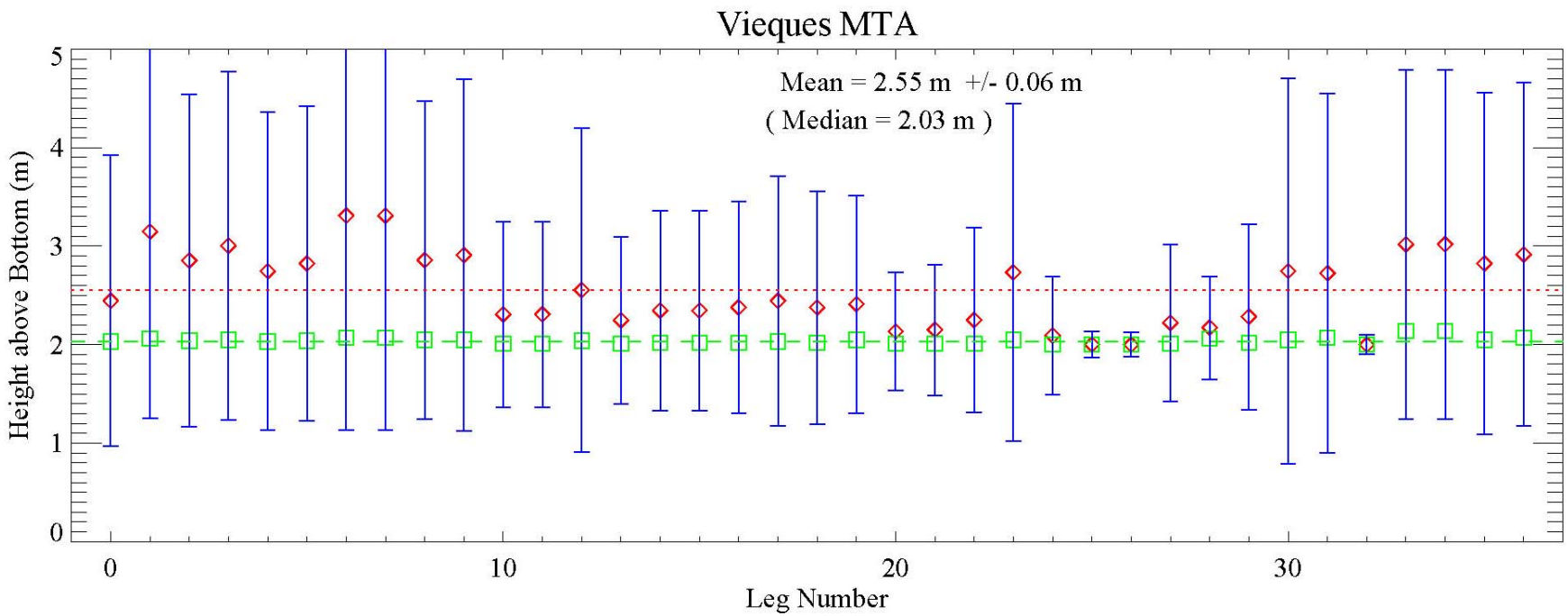

Figure 13 – Plot of the height statistics of the sensor array above the bottom for each leg of survey data. Each leg or separate time series of data is represented by it's mean (red diamond), median (green square) and standard deviation (blue bars) about the mean. The red dotted line signifies the mean of the means, while the green dashed lines signifies the median of the medians. In addition, the values of both these levels, along with the standard deviation of the means, are presented for completeness.

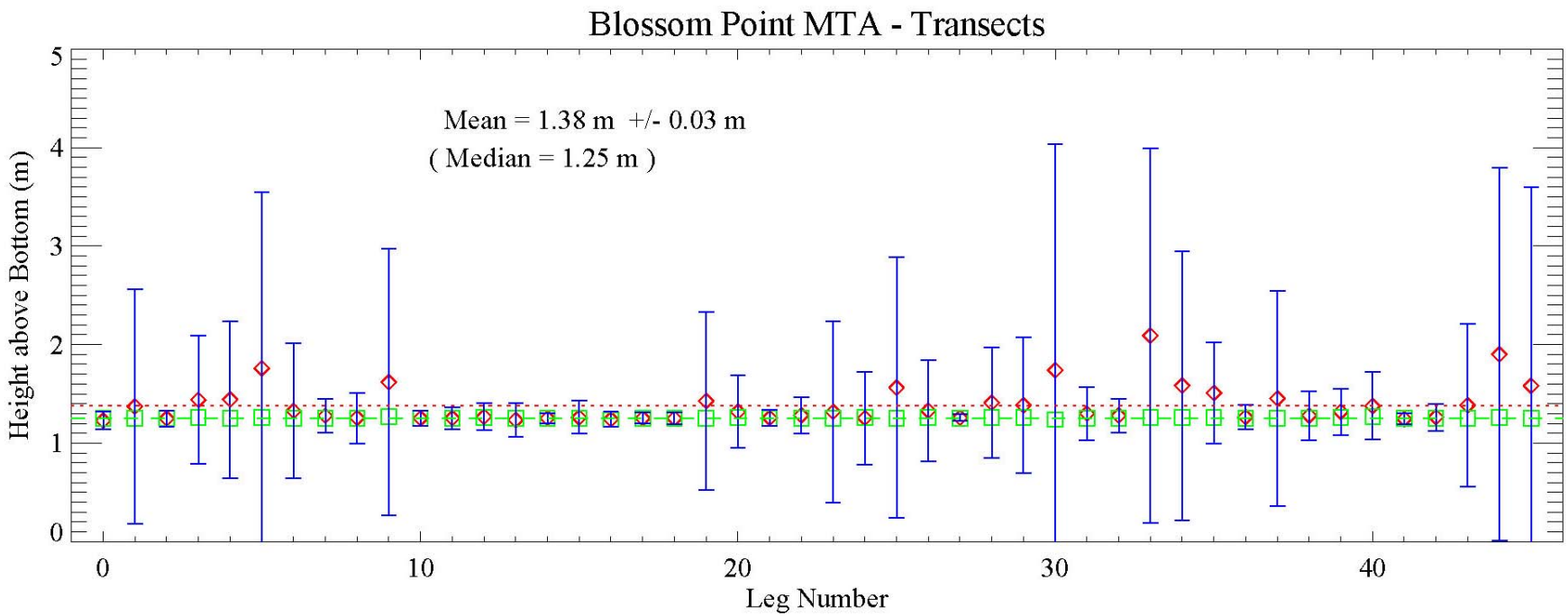

Figure 14 – Plot of the height statistics of the sensor array above the bottom for each leg of survey data. Each leg or separate time series of data is represented by it's mean (red diamond), median (green square) and standard deviation (blue bars) about the mean. The red dotted line signifies the mean of the means, while the green dashed lines signifies the median of the medians. In addition, the values of both these levels, along with the standard deviation of the means, are presented for completeness.

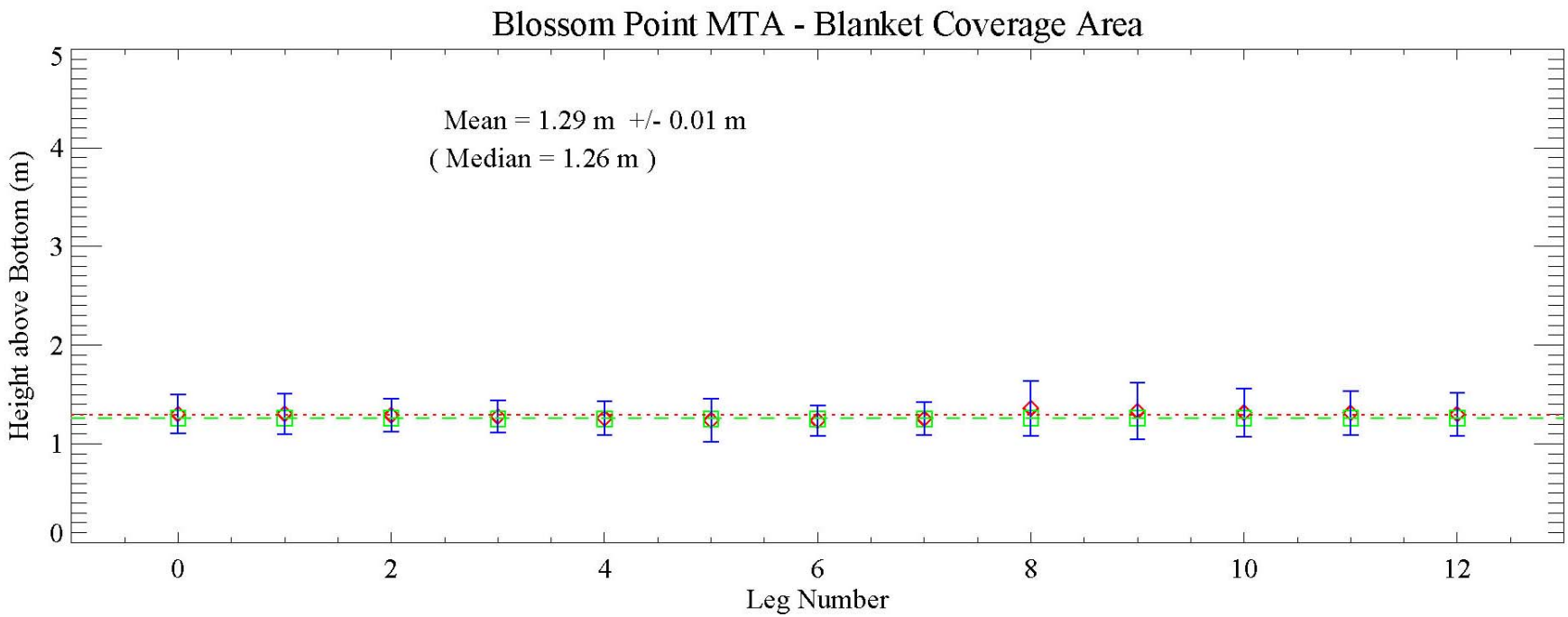

Figure 15 – Plot of the height statistics of the sensor array above the bottom for each leg of survey data. Each leg or separate time series of data is represented by it's mean (red diamond), median (green square) and standard deviation (blue bars) about the mean. The red dotted line signifies the mean of the means, while the green dashed lines signifies the median of the medians. In addition, the values of both these levels, along with the standard deviation of the means, are presented for completeness.

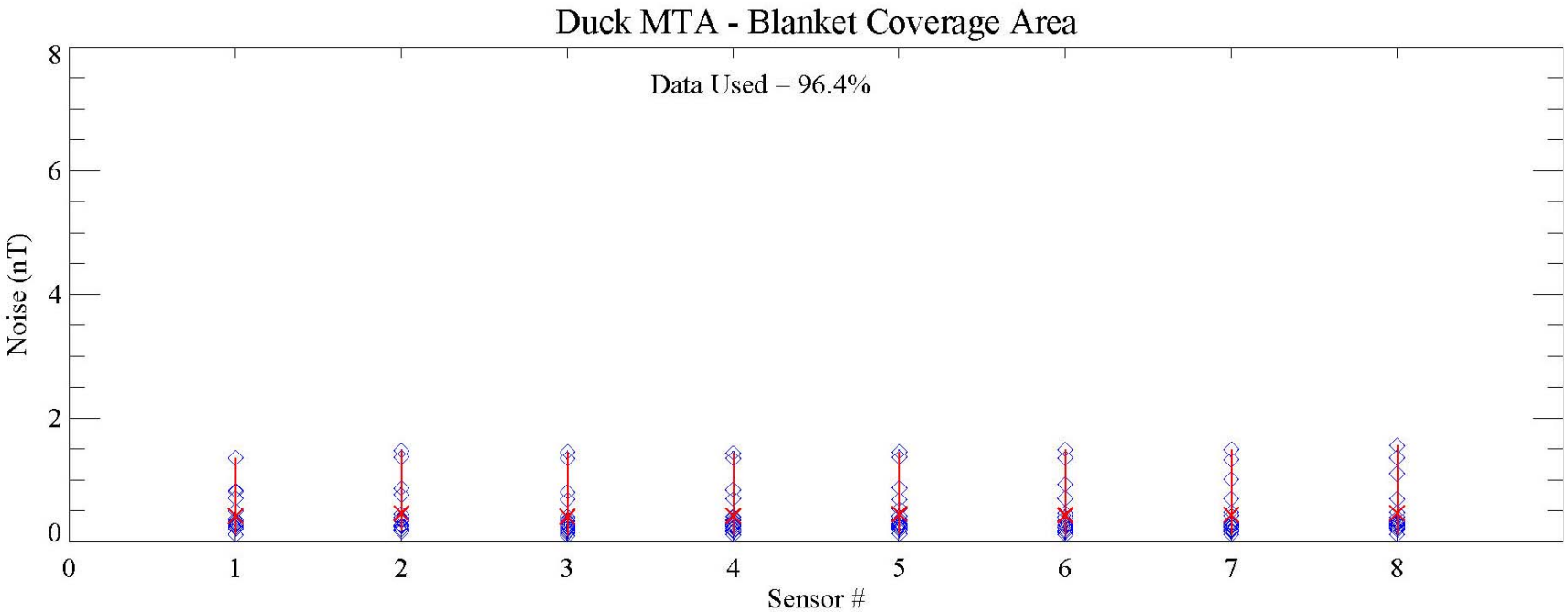

Figure 17 – Plot of noise estimates on a per sensor basis using time series MTA data. The blue diamonds represent estimates for each separate survey leg (i.e. time series), with the red vertical lines connecting the minimum and maximum values. The red crosses represent the mean noise levels for each sensor over all survey legs. The total amount of time series data used in the noise estimations is noted.

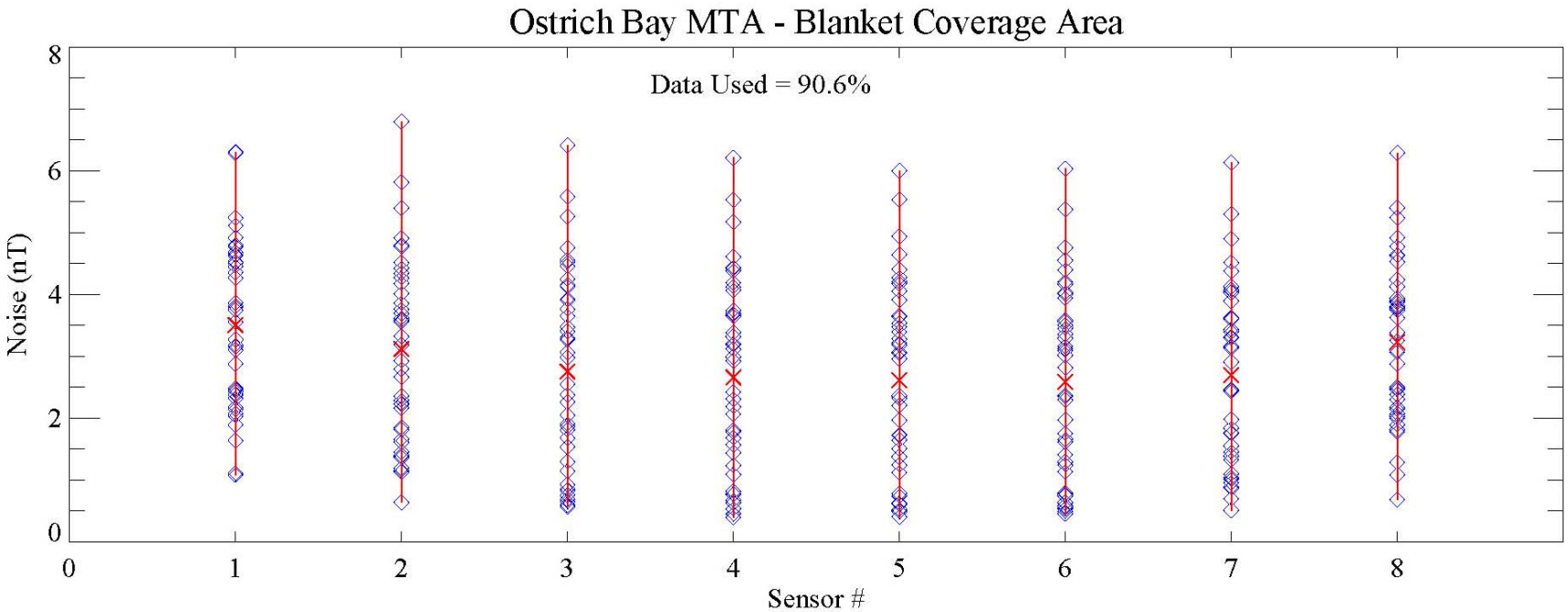

Figure 18 - Plot of noise estimates on a per sensor basis using time series MTA data. The blue diamonds represent estimates for each separate survey leg (i.e. time series), with the red vertical lines connecting the minimum and maximum values. The red crosses represent the mean noise levels for each sensor over all survey legs. The total amount of time series data used in the noise estimations is noted.

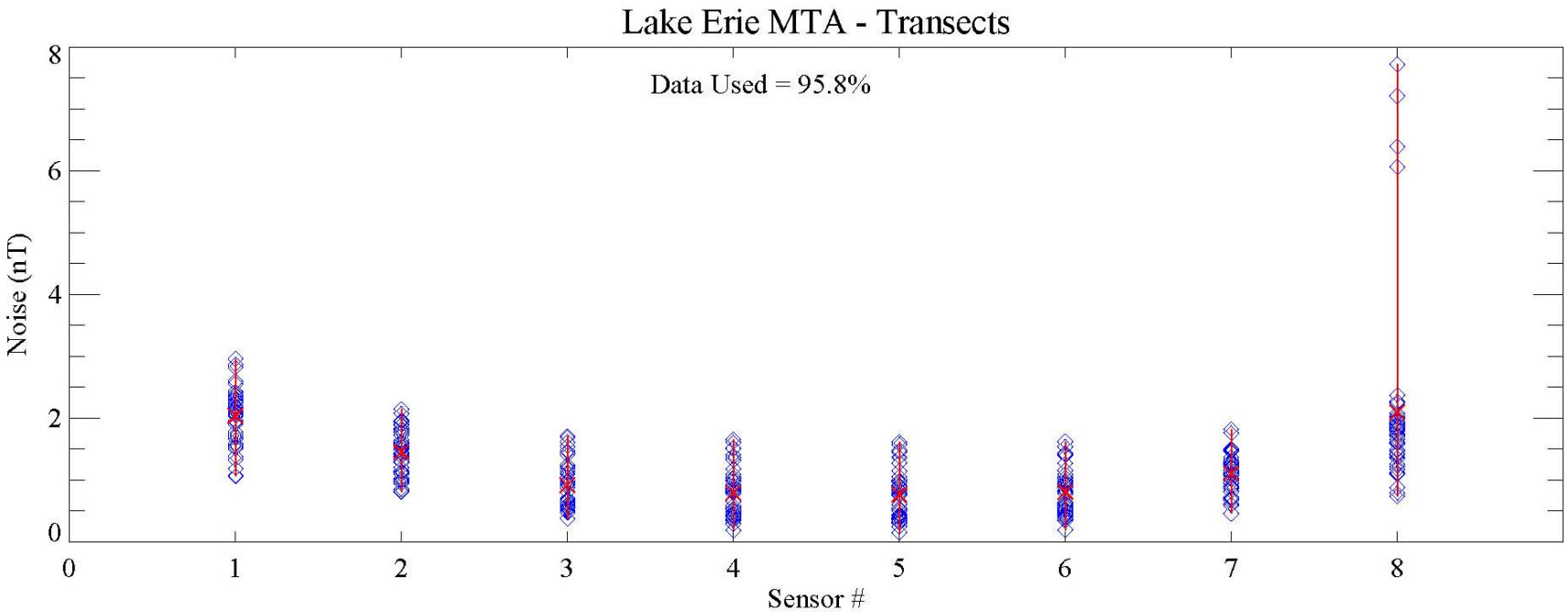

Figure 19 - Plot of noise estimates on a per sensor basis using time series MTA data. The blue diamonds represent estimates for each separate survey leg (i.e. time series), with the red vertical lines connecting the minimum and maximum values. The red crosses represent the mean noise levels for each sensor over all survey legs. The total amount of time series data used in the noise estimations is noted.

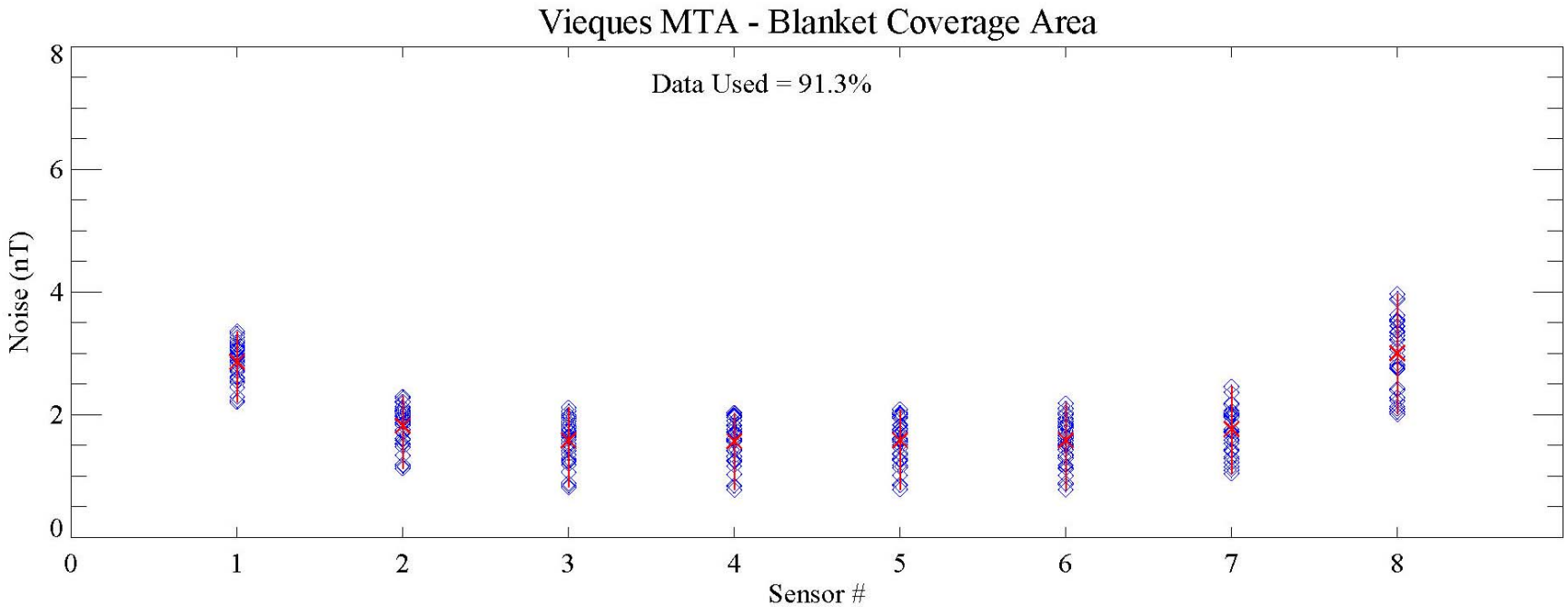

Figure 20 - Plot of noise estimates on a per sensor basis using time series MTA data. The blue diamonds represent estimates for each separate survey leg (i.e. time series), with the red vertical lines connecting the minimum and maximum values. The red crosses represent the mean noise levels for each sensor over all survey legs. The total amount of time series data used in the noise estimations is noted.

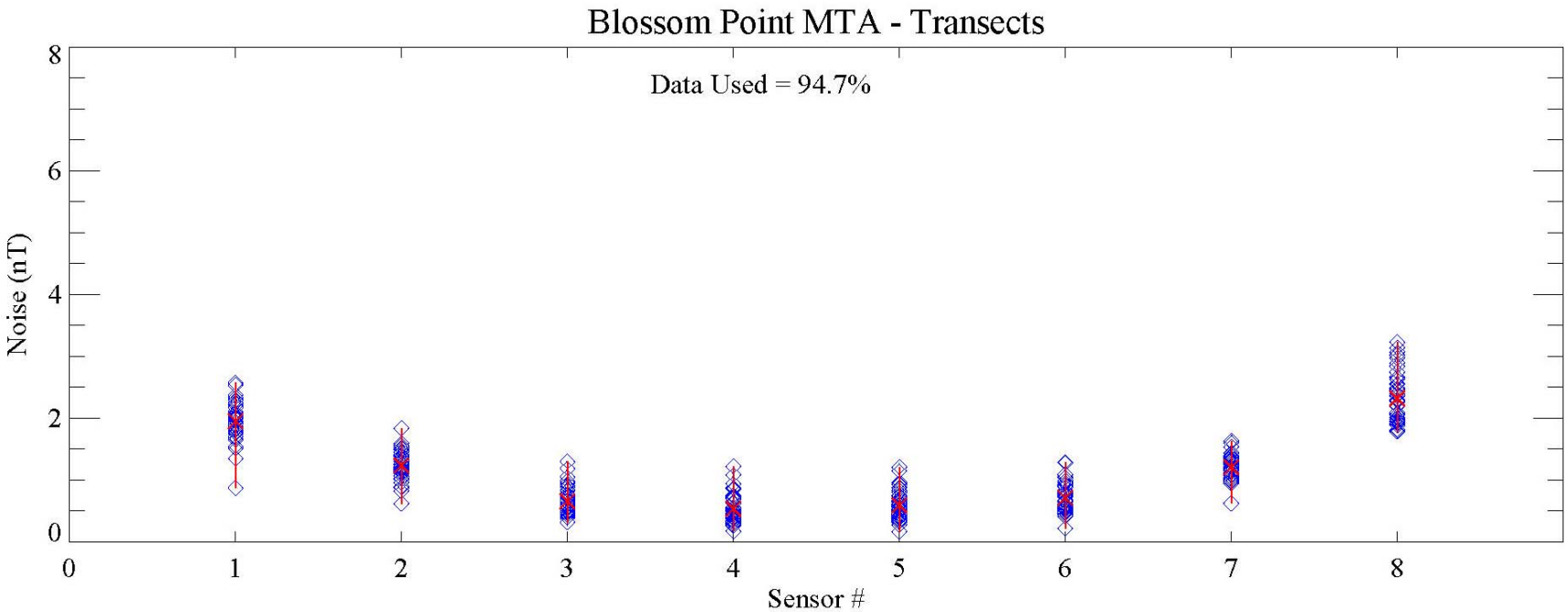

Figure 21 - Plot of noise estimates on a per sensor basis using time series MTA data. The blue diamonds represent estimates for each separate survey leg (i.e. time series), with the red vertical lines connecting the minimum and maximum values. The red crosses represent the mean noise levels for each sensor over all survey legs. The total amount of time series data used in the noise estimations is noted.

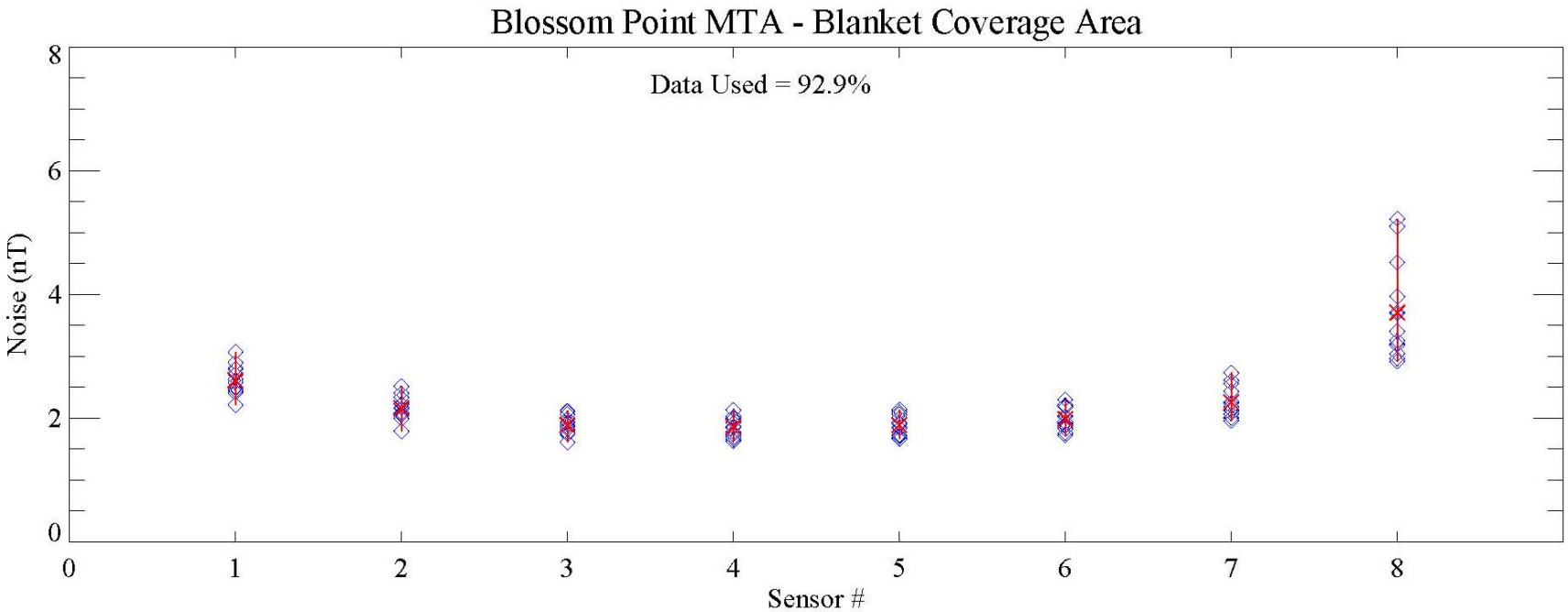

Figure 22 - Plot of noise estimates on a per sensor basis using time series MTA data. The blue diamonds represent estimates for each separate survey leg (i.e. time series), with the red vertical lines connecting the minimum and maximum values. The red crosses represent the mean noise levels for each sensor over all survey legs. The total amount of time series data used in the noise estimations is noted.

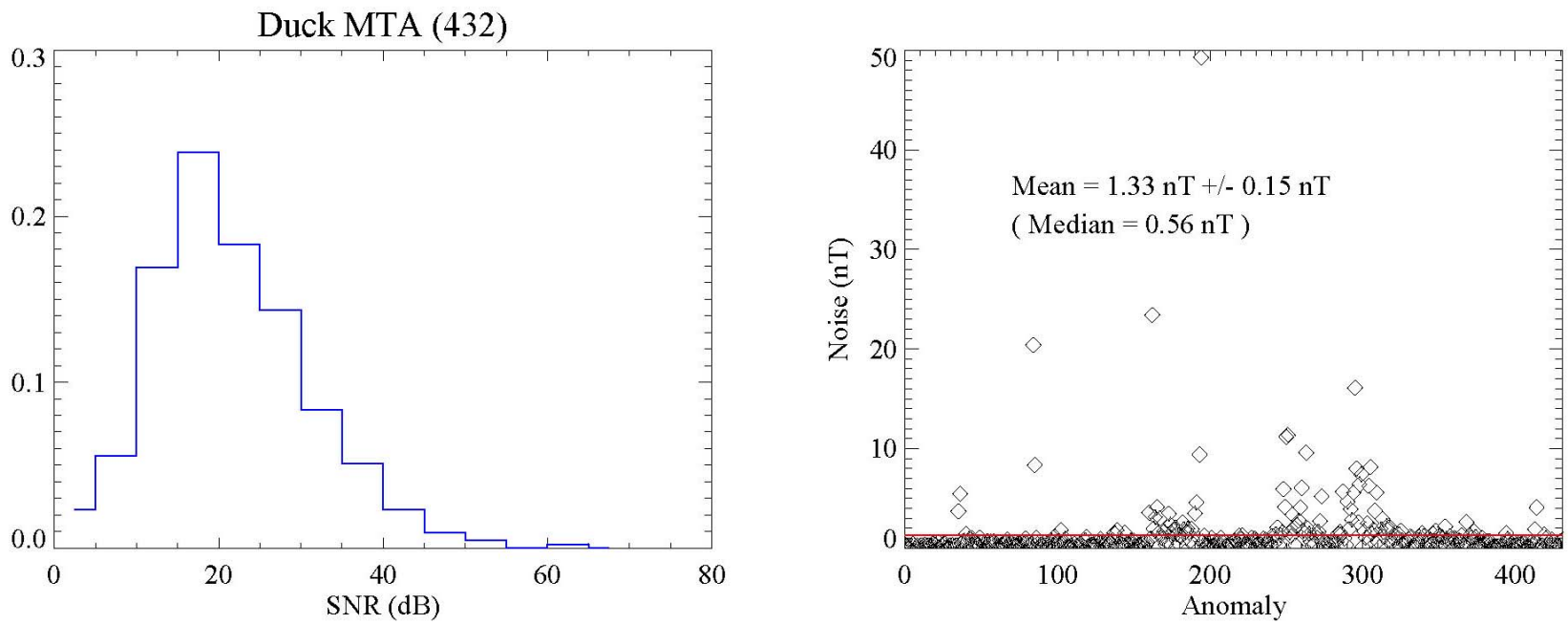

Figure 24 – The left panel shows a histogram of the SNR, expressed in decibels, for all the anomalies analyzed in the magnetometer data collected with the MTA at Duck, NC. The right panel shows a plot of the noise levels derived from the spatially outlying data for each anomaly. The mean noise level (red line) is presented with an uncertainty given by the standard deviation of the mean. The median noise level is also presented as a comparison.

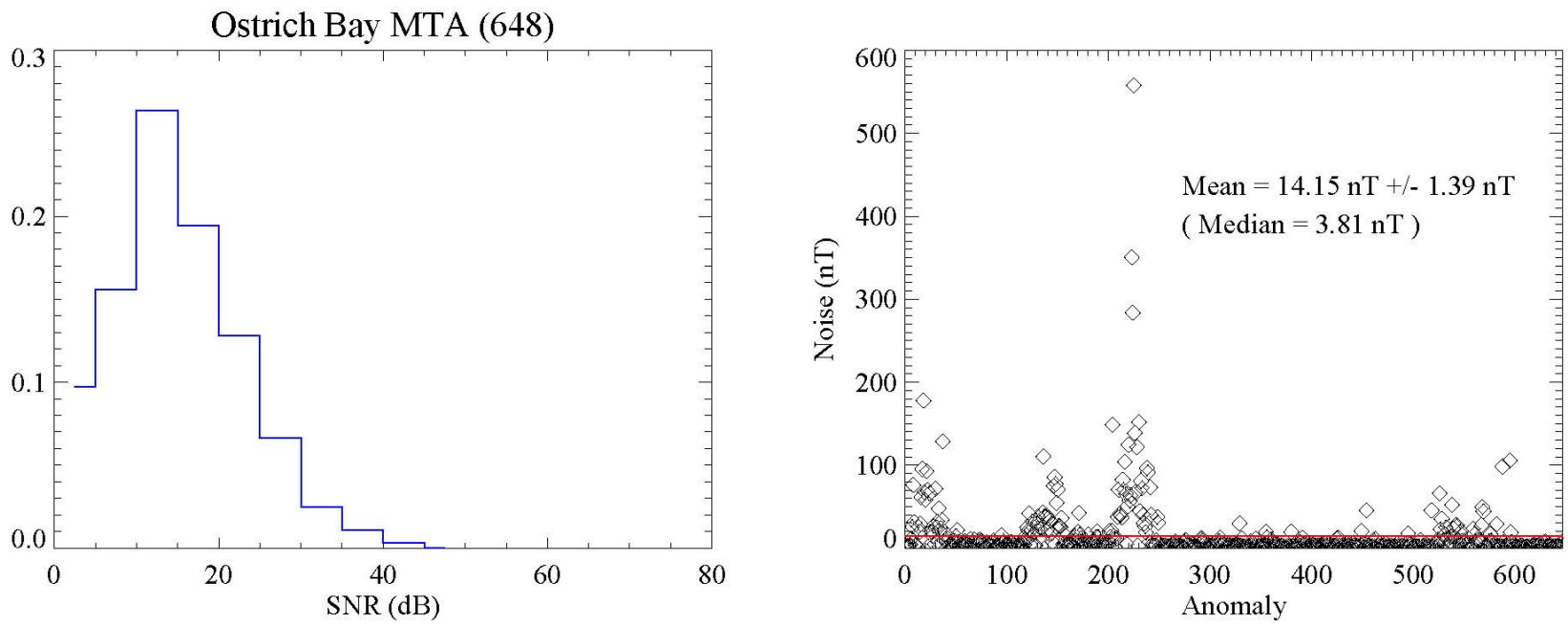

Figure 25 – The left panel shows a histogram of the SNR, expressed in decibels, for all the anomalies analyzed in the magnetometer data collected with the MTA at Ostrich Bay, WA. The right panel shows a plot of the noise levels derived from the spatially outlying data for each anomaly. The mean noise level (red line) is presented with an uncertainty given by the standard deviation of the mean. The median noise level is also presented as a comparison.

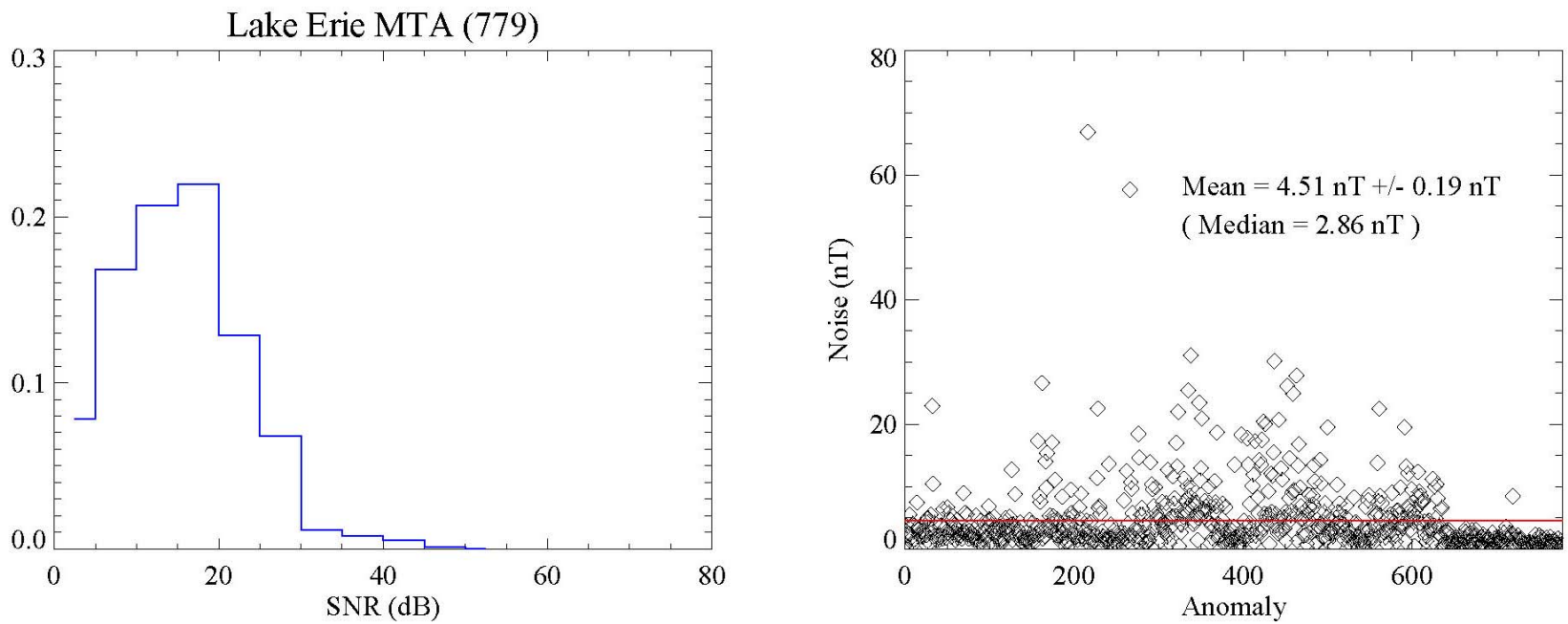

Figure 26 – The left panel shows a histogram of the SNR, expressed in decibels, for all the anomalies analyzed in the magnetometer data collected with the MTA at Lake Erie, OH. The right panel shows a plot of the noise levels derived from the spatially outlying data for each anomaly. The mean noise level (red line) is presented with an uncertainty given by the standard deviation of the mean. The median noise level is also presented as a comparison.

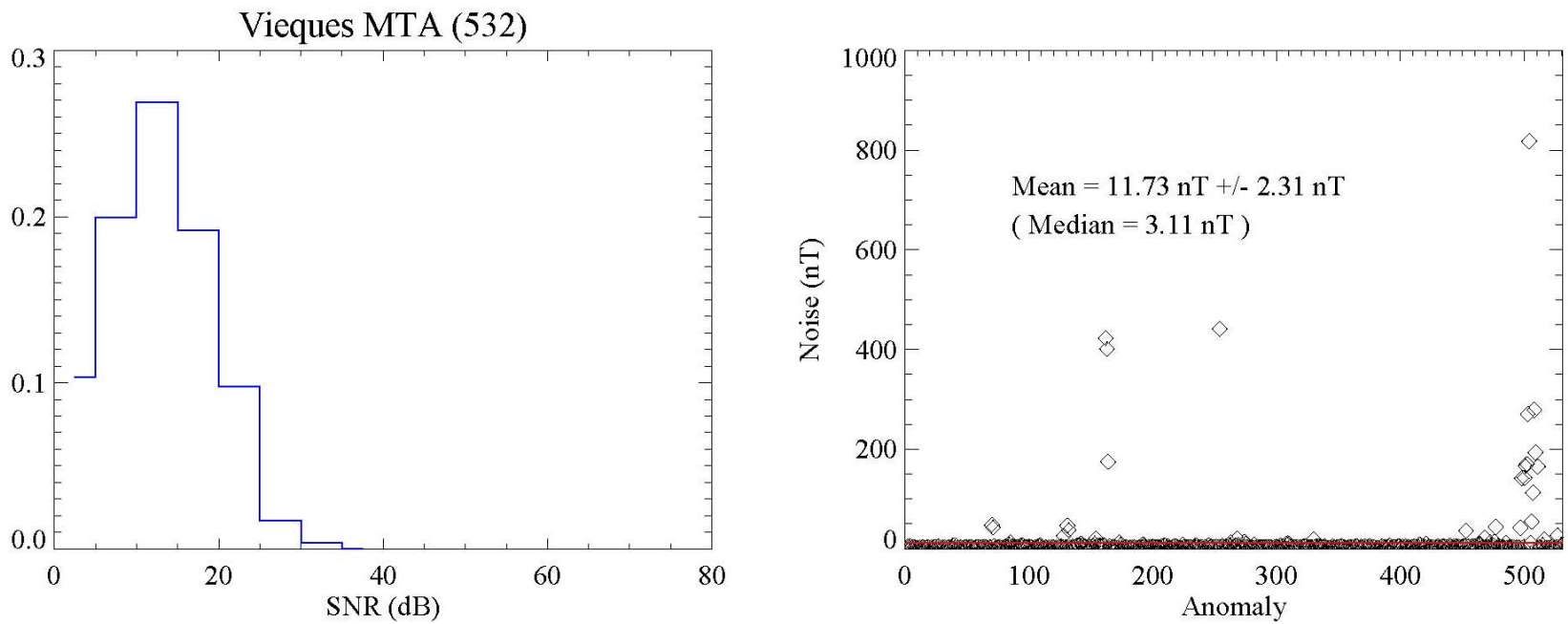

Figure 27 – The left panel shows a histogram of the SNR, expressed in decibels, for all the anomalies analyzed in the magnetometer data collected with the MTA at Vieques, PR. The right panel shows a plot of the noise levels derived from the spatially outlying data for each anomaly. The mean noise level (red line) is presented with an uncertainty given by the standard deviation of the mean. The median noise level is also presented as a comparison.

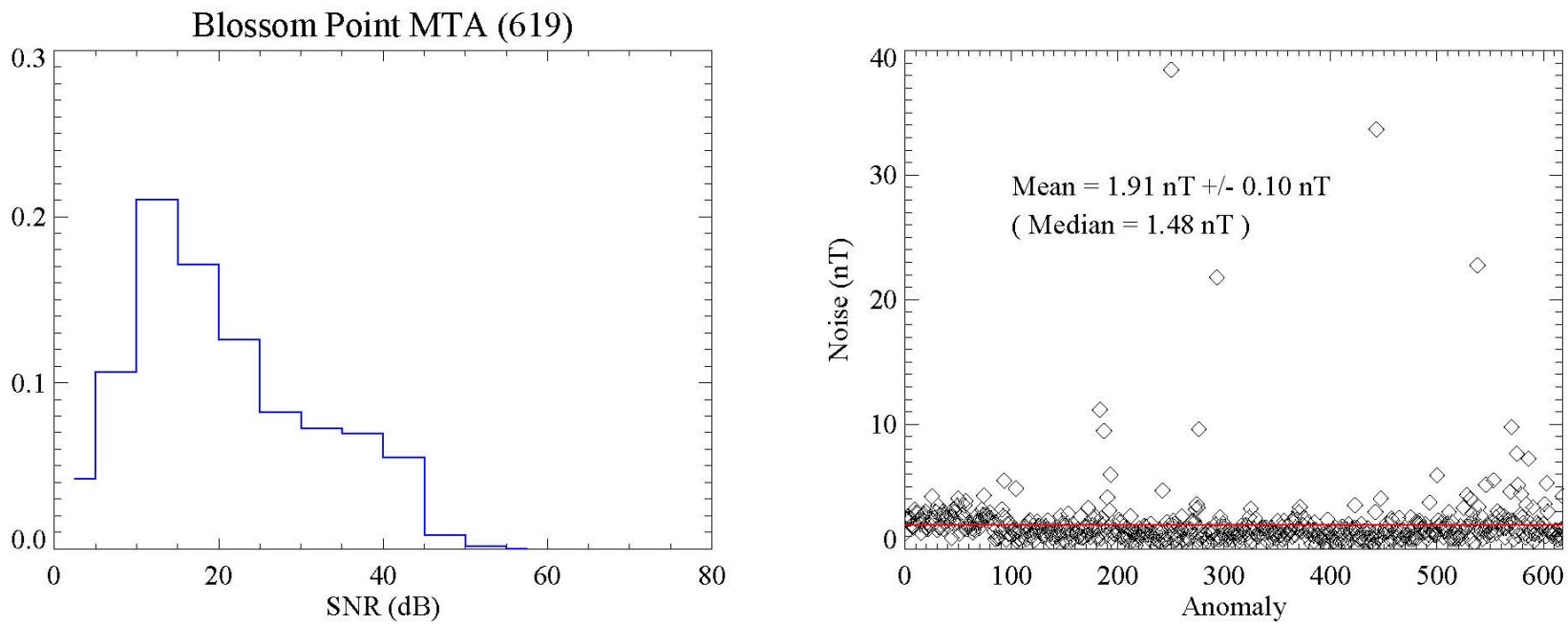

Figure 28 – The left panel shows a histogram of the SNR, expressed in decibels, for all the anomalies analyzed in the magnetometer data collected with the MTA at Blossom Point, MD. The right panel shows a plot of the noise levels derived from the spatially outlying data for each anomaly. The mean noise level (red line) is presented with an uncertainty given by the standard deviation of the mean. The median noise level is also presented as a comparison.

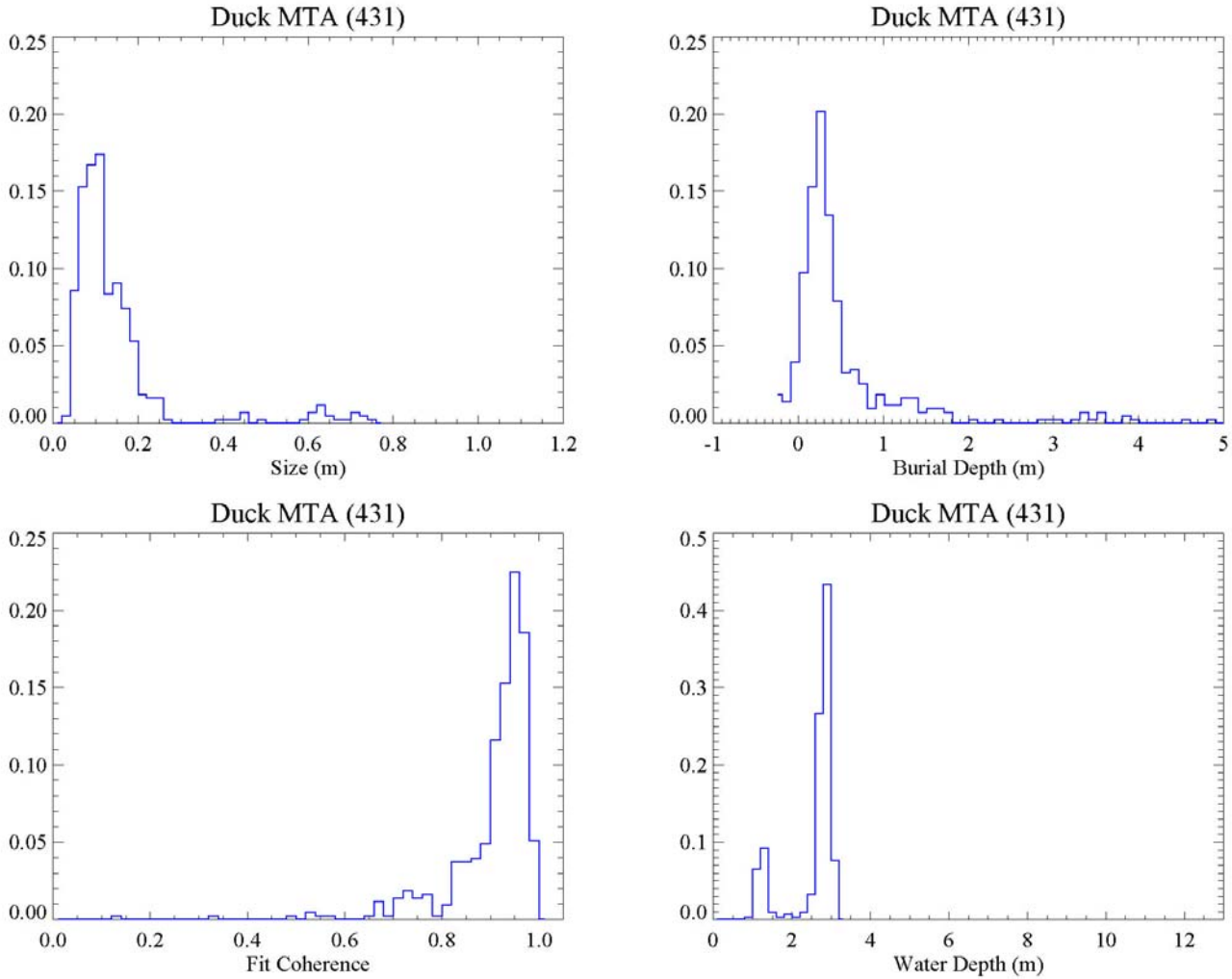

Figure 29 – The top two panels show histograms of the estimates, based on a dipole model, of size and depth of objects that would likely create the anomalies in the magnetometer data collected with the MTA at Duck, NC. The lower left panel shows a histogram of the fit coherence for the same anomalies, while the lower right panel shows a histogram of the water depth at the anomalies in question.

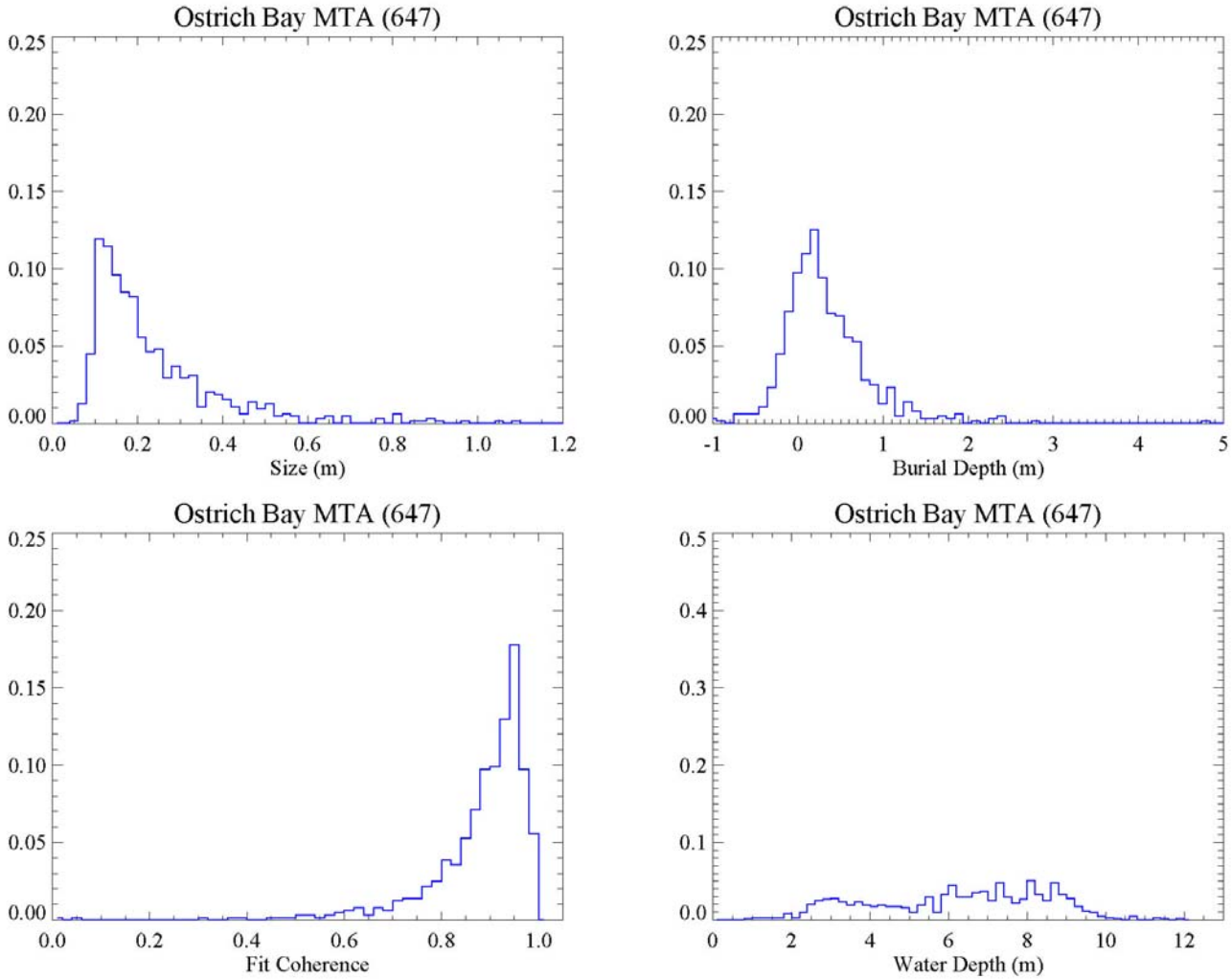

Figure 30 – The top two panels show histograms of the estimates, based on a dipole model, of size and depth of objects that would likely create the anomalies in the magnetometer data collected with the MTA at Ostrich Bay, WA. The lower left panel shows a histogram of the fit coherence for the same anomalies, while the lower right panel shows a histogram of the water depth at the anomalies in question.

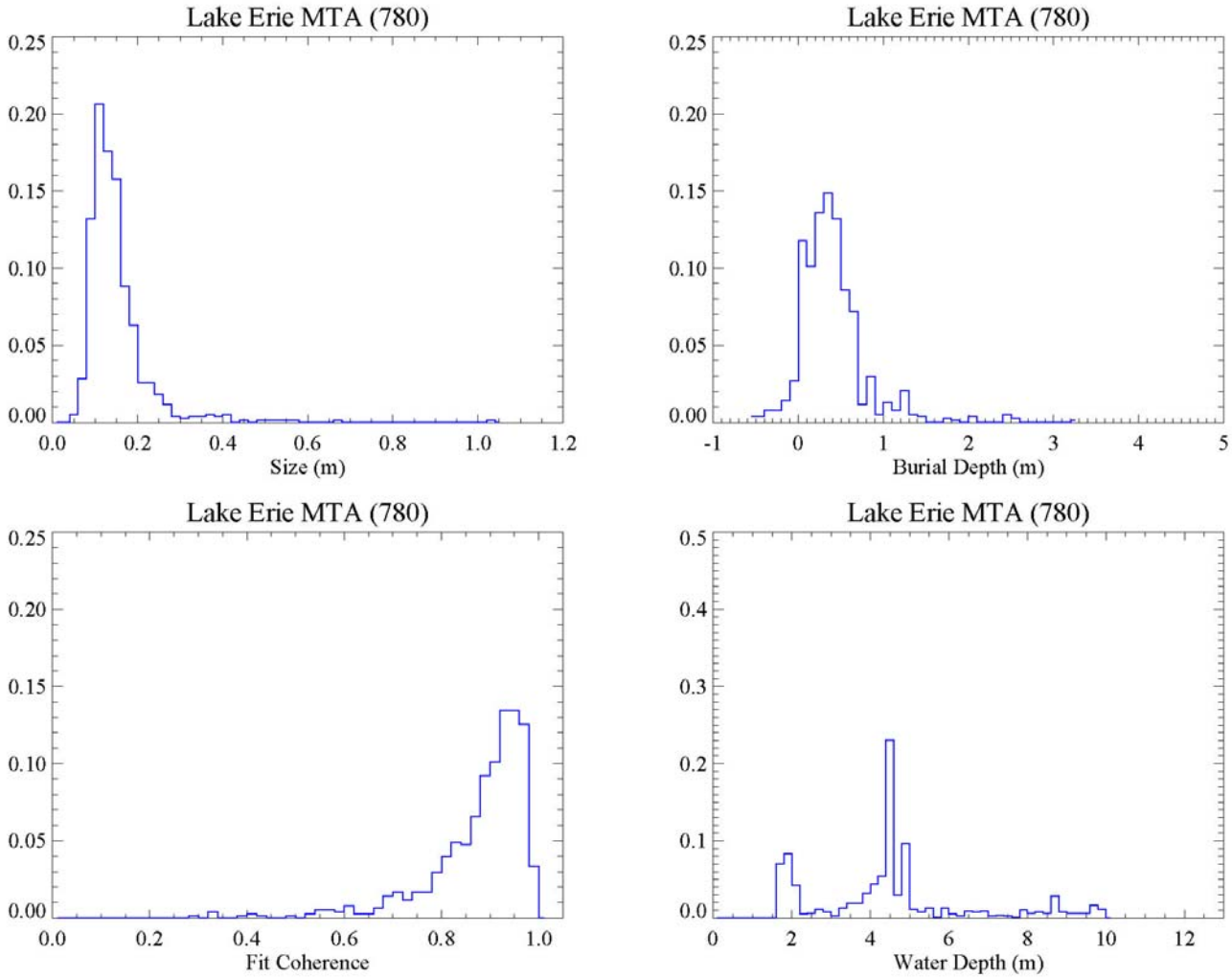

Figure 31 – The top two panels show histograms of the estimates, based on a dipole model, of size and depth of objects that would likely create the anomalies in the magnetometer data collected with the MTA at Lake Erie, OH. The lower left panel shows a histogram of the fit coherence for the same anomalies, while the lower right panel shows a histogram of the water depth at the anomalies in question.

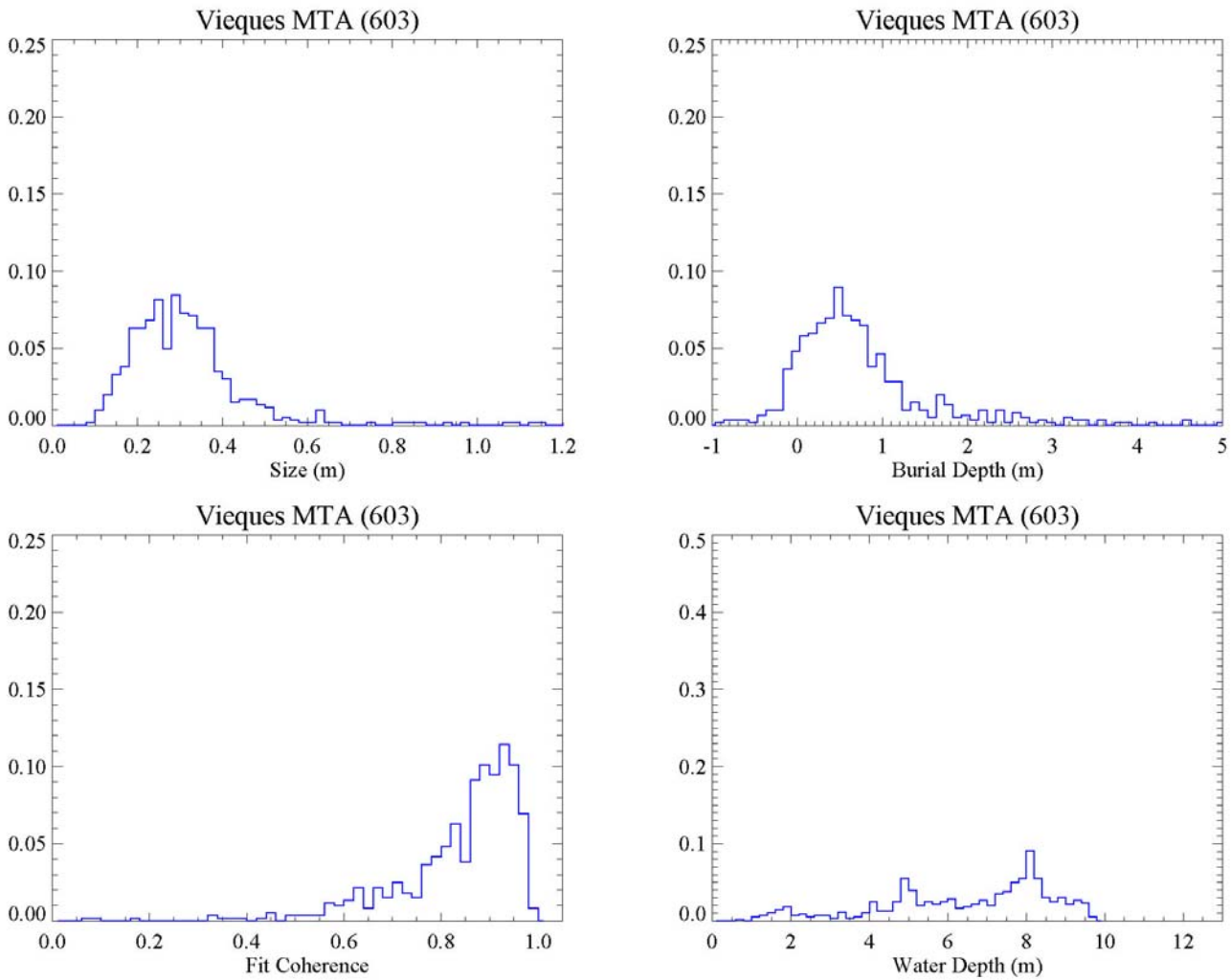

Figure 32 – The top two panels show histograms of the estimates, based on a dipole model, of size and depth of objects that would likely create the anomalies in the magnetometer data collected with the MTA and skiff at Vieques, PR. The lower left panel shows a histogram of the fit coherence for the same anomalies, while the lower right panel shows a histogram of the water depth at the anomalies in question.

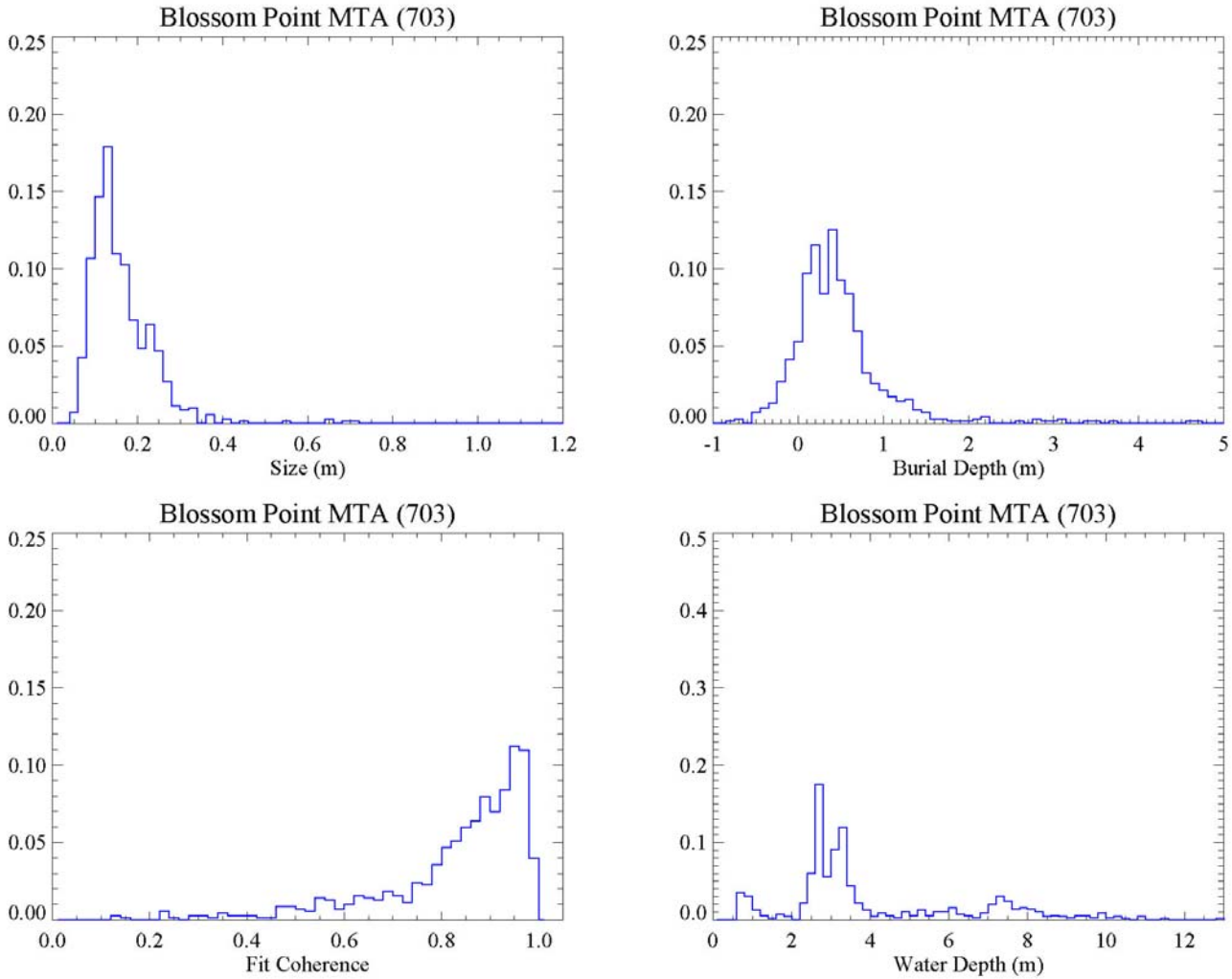

Figure 33 – The top two panels show histograms of the estimates, based on a dipole model, of size and depth of objects that would likely create the anomalies in the magnetometer data collected with the MTA and skiff at Blossom Point, MD. The lower left panel shows a histogram of the fit coherence for the same anomalies, while the lower right panel shows a histogram of the water depth at the anomalies in question.

References

1. "Marine Towed Array Technology Demonstration at the Former Naval Duck Target Facility," Final Report, November 21, 2005

2. "Demonstration of the Marine Towed Array on Ostrich Bay at the Former Naval Ammunition Depot – Puget Sound, June 12-30, 2006," ESTCP Project MM2003-24, Final Report, September 20, 2008

3. "The MTA UXO Survey and Target Recovery on Lake Erie at the Former Erie Army Depot – ESTCP Project MM2003-24," Final Report, January 25, 2007

4. "Demonstration of the Marine Towed Array on Bahia Salinas del Sur – Vieques, Puerto Rico, June 1-30, 2007," Final Report, November 3, 2008

5. "?," Final Report, September, 2009

6. http://www.geosoft.com/downloads/whatisit/uxoqaqc.asp

7. "UCEANALYSETARGET GX," available under the free UX-Process Software extension for Geosoft Oasis Montaj, version 6.4, May 28, 2007

8. DeProspo,D. and R. DiMarco, "Automatic Detection and Characterization of Magnetic Anomalies in Total Field Magnetometer Data," in Conference Proceedings of the UXO Forum 1996, Williamsburg Virginia, pp. 301-307, March 1996

9. Barrow B. and H. H. Nelson, "Collection and analysis of multi-sensor ordnance signatures," *J. Environ. Eng. Geophys.*, vol. 3, no. 2, pp. 71–79, 1998